UNIVERSITY OF CALIFORNIA
SANTA CRUZ

GEOPHYSICAL AND GEOCHEMICAL EXAMINATION OF THE ICE-OCEAN BOUNDARY TO DETERMINE PAST AND PRESENT GLACIAL CONDITIONS

A dissertation submitted in partial satisfaction
of the requirements for the degree of

DOCTOR OF PHILOSOPHY

in

EARTH SCIENCES

by

Sarah U. Neuhaus

September 2021

The Dissertation of Sarah U. Neuhaus is approved:

_____
Professor Slawek Tulaczyk, chair

_____
Professor Susan Schwartz

_____
Professor Terrence Blackburn

_____
Professor Andrew Fisher

_____
Peter Biehl
Vice Provost and Dean of Graduate Studies

Table of Contents

List of Figures

List of Tables

Abstract

Geophysical and geochemical examination of the ice-ocean boundary to determine past and present glacial conditions

Sarah U. Neuhaus

Ice sheets and glaciers that are in contact with the ocean lose ice more rapidly than land-terminating ice masses due to melting at the ice-ocean interface and iceberg calving. Hence, ice sheets and glaciers in contact with the ocean have the greatest potential to raise sea levels in the near future. With roughly a quarter of the global population living near the coast (Small and Nicholls, 2003), it is therefore critical to understand how these glaciers will respond to a warming climate. The way that we do this is by examining how they interact with the ocean presently, and how they have interacted with the ocean in the past. My dissertation consists of three studies in which I examine interactions between glacier ice and the ocean, covering time periods from two million years ago to the present. In addition to examining different time scales, I examine different mechanisms of ice-ocean interaction to gain a broader understanding of the processes occurring at the ice-ocean interface.

Chapter 1

In my first chapter, I examine the spatial and temporal distribution of icebergs inside a temperate fjord in Alaska. Although most of the ice on Earth is locked up in Greenland and Antarctica, the glaciers that have been contributing most to sea level rise in recent decades are the more temperate glaciers outside of Greenland and

Antarctica (Gardner et al., 2013). As the climate warms and glaciers in Greenland thin, the fjords which connect the Greenland Ice Sheet to the ocean might begin to resemble present day temperate fjords. Thus, understanding how icebergs interact with the circulation patterns inside temperate fjords can help us predict the behavior of the Greenland Ice Sheet in the near future.

Circulation inside fjords is often characterized as having two layers: a deeper one which flows towards the glacier front and contains relatively warm and salty waters, and a shallow one which flows away from the glacier and contains cooler, fresher waters (Klinck et al., 1981). The incoming warmer waters interact with the front of the glacier (the terminus) and become cooler and more buoyant either by inducing glacier melt or by receiving an influx of subglacial meltwater (Carroll et al., 2015). Icebergs are typically omitted from fjord circulation models, although they have the potential to alter this circulation pattern by increasing the spatial distribution of freshwater input and by cooling the incoming deeper water masses before they reaches glacier termini.

To explore this potential, I examined high-resolution satellite imagery, creating an algorithm to identify icebergs based on pixel brightness. The imagery spanned March to November, allowing me to examine seasonal differences in iceberg size distributions and spatial distributions. I found that the large icebergs were more likely to run aground in the shallow areas of the fjord, located primarily along the sides of the fjord and over submarine moraines. This has implications for where freshwater is added to the fjord because the large icebergs contain most of the ice

volume. Fitting power-law equations to the observed iceberg size distributions allowed me to determine that iceberg fracture was much more prevalent during the summer months.

I also compared iceberg keel depth to salinity and temperature profiles (CTD profiles) measured in the fjord and found that although the icebergs were interacting with the upper, outflowing water layer, they were not large enough to penetrate the deeper, warmer, incoming water. Additionally, the total surface area of the icebergs in contact with the water was far less than the surface area of the glacier terminus. Thus, in this fjord, icebergs have limited effect on the thermal budget of the fjord. Currently in Greenland, icebergs are much larger and have much longer residence times, and therefore are able to alter the circulation patterns and cool the incoming water before it reaches the terminus (Enderlin et al., 2016; Enderlin and Hamilton, 2014; Moon et al., 2018a; Sulak et al., 2017). But in a warmer climate, icebergs inside Greenland fjords may stop being able to provide this buffer, resulting in an increase in melt at the glacier terminus.

Chapter 2

My second chapter focuses on the position of the grounding line (the location where grounded ice transitions to a floating ice shelf) in West Antarctica following the Last Glacial Maximum (LGM). Knowing the location of the grounding line is crucial to understanding the stability of the West Antarctic Ice Sheet (WAIS) based on the theory of marine ice sheet instability (MISI). MISI states that marine ice

sheets – ice sheets whose beds are located below sea level, e.g. WAIS – with beds that slope towards the center of the ice sheet rather than the margins are inherently unstable because any thinning or perturbation of the grounding line position could lead to runaway retreat (Weertman, 1974). The position of the WAIS grounding line at the LGM is well constrained from geomorphological evidence (Bentley et al., 2014). The current position of the WAIS grounding line is also well known from geophysical methods (Brunt et al., 2010; Rignot et al., 2011). Although there has been some debate about timing and mechanism of the initiation of post-LGM grounding line retreat, the enduring paradigm has been that the grounding line retreated unidirectionally (Ackert, 2008; Anderson et al., 2014; Bentley et al., 2014; Conway et al., 1999; Hall et al., 2013). However, recent analysis of radiocarbon found in sediment samples collected from below the ice sheet indicate that the grounding line actually retreated further back than its current position and subsequently re-advanced (Kingslake et al., 2018). In this chapter, I re-examine measurements taken in the Ross Sea section of WAIS in order to better constrain the timing of post-LGM grounding line retreat and re-advance.

To constrain the timing of grounding line retreat, I analyzed radiocarbon and total organic carbon (TOC) present in subglacial sediments at six different field sites in the Ross Sea sector. Because of the overabundance of radiocarbon dead material in Antarctica, conventional methods of radiocarbon dating result in ages that are much too old (Andrews et al., 1999). To circumvent this, I created a radiocarbon model that also accounts for accumulation of radiocarbon. Comparing the results of

my model to the radiocarbon and TOC measurements allowed me to put bounds on the length of exposure to the ocean (i.e. amount of time the grounding line was behind my field sites).

To constrain the timing of grounding line re-advance in the Ross Sea sector, I modelled heat diffusion through ice and ionic diffusion through sediment porewater. By comparing my results to observed temperature and ionic profiles, I was able to put bounds on the timing of grounding line re-advance over the area.

I found that the grounding line retreat coincided with warm periods in the climate, and that the re-advance coincided with cooling periods. This is concerning for the stability of WAIS at present because the amount of climate warming that coincided with retreat of over 1000 km was less than 2 ºC, which is the amount of warming that is predicted by the end of the 21st Century (Collins et al., 2013; Cuffey et al., 2016; Cuffey, 2017).

Chapter 3

My third chapter concerns cryogenic brines found in sediment porespaces at the margin of the Antarctic Ice Sheet. Hypersaline brines have been found in deep boreholes in places that were formerly glaciated in the Northern Hemisphere (Bottomley et al., 1994; Frape and Fritz, 1982; Starinsky and Katz, 2003). In Antarctica, hypersaline brines are less prevalent, but have been found in two deep boreholes as well as on the surface and in the shallow subsurface of the McMurdo Dry Valleys (Foley et al., 2019; Frank et al., 2010; Lyons et al., 2019; Pompilio et al.,

2007). Additionally, precipitates have been found indicating the past presence of brines (Blackburn et al., 2020; Fitzpatrick et al., 1990). Not only do these brines serve as an important source of nutrients for microbes (Mikucki et al., 2009), they help provide information about ice sheet sensitivity to climate by giving rise to mineral precipitation which can be used to interpret past glacial conditions (Blackburn et al., 2020). While there is agreement that these brines result from seawater which has been concentrated through freezing, the actual environment in which these brines form has been debated (Starinsky and Katz, 2003).

Previous ideas about how these brines formed require seawater to be periodically isolated from the ocean in a basin (Grasby et al., 2013; Starinsky and Katz, 2003). While cut off from the ocean, the basin freezes over and hypersaline brines form. Because these brines are denser than the surrounding water, they sink to the bottom of the basin and infiltrate the subsurface. However, the two boreholes in Antarctica are currently located in the ocean at depths of 935 m (Falconer et al., 2007) and 384 m below sea level (Florindo et al., 2008). At these depths it is unlikely that these sites were cut off from the ocean except when overridden by the Antarctic Ice Sheet. Therefore, I propose a new mechanism for the formation of these brines which does not require the presence of an isolated marine basin.

I propose that hypersaline brines form in the pore spaces of sediments which have experienced repeated cycles of ice sheet advance and retreat. When the ice sheet retreats and the sediments are exposed to the ocean, seawater infiltrates the pore spaces. When the climate becomes favorable for ice sheet advance, the sediments are

covered by ice. This can affect the brine concentration in two ways. When the ice sheet is cold at the base and basal freeze-on occurs, the brines become more concentrated. When conditions are such that the ice sheet is warm at the base and melting occurs, the brines are diluted by basal meltwaters. Repeated cycles of exposure to seawater, freezing, and melting can lead to the formation of hypersaline brines.

To verify the plausibility of this idea, I ran a time-dependent advection-diffusion model of porewater chemistry and compared the results to geochemical measurements made on porewater samples from the two Antarctic boreholes. I ran the model for 10-20 glacial cycles, each 100,000 years long, and was able to successfully match the porewater chemistry data. This process not only allowed me to verify that a subglacial mechanism for brine formation is plausible, but it allowed me to learn something about past grounding line activity in this area. I was able to re-create the chemical composition of brines in one borehole within seven 100,000-year cycles (700,000 years), while the other borehole required nearly 20 glacial cycles (2 million years). Thus, despite these two sites being located within 50 km of each other, they have experienced very different glacial conditions. These differences may, however, be due to the large difference in water depths between the two borehole sites.

Acknowledgments

I would like to thank my friends, family, and colleagues who supported me throughout graduate school.

The text of this dissertation includes reprint of the following previously published material:

Chapter 1:
Neuhaus, S. U., Tulaczyk, S. M., and Branecky Begeman, C.: Spatiotemporal distributions of icebergs in a temperate fjord: Columbia Fjord, Alaska, The Cryosphere, 13, 1785–1799, https://doi.org/10.5194/tc-13-1785-2019, 2019.

An earlier version of Chapter 2 was published as a discussion paper under the citation:

Neuhaus, S. U., Tulaczyk, S. M., Stansell, N. D., Coenen, J. J., Scherer, R. P., Mikucki, J. A., and Powell, R. D.: Did Holocene climate changes drive West Antarctic grounding line retreat and re-advance?, The Cryosphere Discuss. [preprint], https://doi.org/10.5194/tc-2020-308, in review, 2020.

Chapter 1: Spatiotemporal Distributions of Icebergs in a Temperate Fjord: Columbia Fjord, Alaska

Abstract

Much of the world's ice enters the ocean via outlet glaciers terminating in fjords. Inside fjords, icebergs may affect glacier-ocean interactions by cooling incoming ocean waters, enhancing vertical mixing, or by providing back stress on the terminus. However, relatively few studies have been performed on iceberg dynamics inside fjords, particularly outside of Greenland. We examine icebergs calved from Columbia Glacier, Alaska, over eight months spanning late winter to mid-fall using 0.5-meter resolution satellite imagery, identifying icebergs based on pixel brightness. Iceberg sizes fit a power-law distribution with an overall power-law exponent, m, of -1.26 ± 0.05. Seasonal variations in the power-law exponent indicate that brittle fracture of icebergs is more prevalent in the summer months. Combining our results with those from previous studies of iceberg distributions, we find that iceberg calving rate, rather than water temperature, appears to be the major control on the exponent value. We also analyze icebergs' spatial distribution inside the fjord and find that large icebergs (10,000 m^2 – 100,000 m^2 cross-sectional area) have low spatial correlation with icebergs of smaller sizes due to their tendency to ground on shallow regions. We estimate the surface area of icebergs in contact with incoming seawater to be 3.0 ± 0.63 x 10^4 m^2. Given the much larger surface area of the terminus, 9.7 ±

3.7×10^5 m^2, ocean interactions with the terminus may have a larger impact on ocean heat content than interactions with icebergs.

1 Introduction

In recent decades, fjord-terminating glaciers have been rapidly losing mass (Larsen et al., 2007; Pritchard et al., 2009), contributing significantly to eustatic sea level rise (Gardner et al., 2013; McNabb and Hock, 2014). High volumes of ice discharge due to iceberg calving and submarine melt have been attributed to contact between the glacier terminus and relatively warm and salty fjord waters (Bartholomaus et al., 2013; Motyka et al., 2003). Current fjord circulation models do not take icebergs into account, though icebergs may modify warm, dense waters entering the fjord by enhancing vertical mixing and by extracting heat through iceberg melt (Carroll et al., 2015; Klinck et al., 1981; Mortensen et al., 2018; Motyka et al., 2003; Rignot et al., 2010). Various studies have examined the iceberg calving process (Bahr, 1995; Chapuis and Tetzlaff, 2014; Hughes, 2002; O'Neel et al., 2003; Warren et al., 2001), as well as the transport and evolution of icebergs in the open ocean (Bigg et al., 1997; Dowdeswell and Forsberg, 1992; Gladstone et al., 2001; Kubat et al., 2007), but comparably little is known about iceberg evolution inside the fjords where they originate.

Recent studies of icebergs have focused on icebergs calved from Greenland or Antarctic glaciers, however in this study we characterize the size and location of icebergs in a major Alaskan fjord using high-resolution satellite imagery. We

examine the differences in iceberg populations over a span of eight months in 2013 to gain insights into their seasonal variability. We also investigate how icebergs evolve along the fjord to better understand where iceberg meltwater is introduced in vertical and horizontal dimensions.

Our analyses focus on the fjord of Columbia Glacier, which connects with Prince William Sound, Alaska. Columbia Glacier is the single largest contributor to ice loss from Alaskan glaciers, accounting for ~6-17% of annual land ice loss from this region (Gardner et al., 2013; Pfeffer, 2015; Rasmussen et al., 2011). Columbia Glacier is also one of the best-studied glaciers in the world. The United States Geologic Survey (USGS) has been instrumenting Columbia Glacier since the 1970's, and the first time-lapse cameras used to study glacier movement and iceberg calving were implemented in 1978 (Meier and Post, 1978; Pfeffer, 2012). From 2012 to 2015, the Prince William Sound Regional Citizen's Advisory Council (PWSRCAC) commissioned a study of Columbia Glacier, which included several field campaigns and geophysical tools, with the aim of better predicting the future behavior of the glacier. PWSRCAC was particularly interested in understanding iceberg discharge, as icebergs that exit Columbia Fjord later intrude on the shipping lanes into and out of the Port of Valdez (Pfeffer, 2012, 2013a, 2013b, 2014a, 2014b, 2015).

Columbia Glacier has a total surface area of around 910 km^2 (McNabb et al., 2012a), and is located in central Alaska in the Chugach Mountains (Fig. 1.1). From 1794 – when the terminus of Columbia Glacier was first mapped by Captain George Vancouver – to 1980, the terminus of the glacier was in a stable location, terminating

at the northern end of Heather Island (Meier and Post, 1978; Post, 1975). From 1980 to 2013, the year when the satellite images used in this project were acquired, the glacier retreated approximately 20 km. This retreat revealed a fjord extending north-south, roughly 5 km in width and 20 km in length. At the entrance to the fjord is a submarine end moraine – which shall be referred to as "Heather Moraine" – built by the glacier when it was in its extended Neoglacial position (Meier and Post, 1978). An oceanographic survey of Columbia Fjord completed in 1983 determined that the water column over Heather Moraine was shallow – less than 20 m below Mean Lower Low Water (the average height of the lowest tide over the National Tidal Datum Epoch, as defined by the National Oceanographic and Atmospheric Administration [NOAA]) – and partially exposed (Pfeffer, 2013a; Walters et al., 1988). Pfeffer (2013a) examined more recent bathymetric surveys of Heather Moraine and found that the bathymetry did not change significantly between 1977 and 2005, indicating that very little erosion has occurred. The mean tidal fluctuation in nearby Valdez, as measured by NOAA, is ~3m, with maximum fluctuations up to 5-6m, indicating the maximum water depth above Heather Moraine to be ~25m. Behind Heather Moraine, fjord bathymetry descends to 200 m below sea level. (Walters et al., 1988). Iceberg calving rates increased following the initiation of glacial retreat, and reached a maximum of over 10 $km^3\ yr^{-1}$ in 1999-2000 (Pfeffer, 2013b) – 8.5 $km^3\ yr^{-1}$ averaged over 1996-2007 (Rasmussen et al., 2011). Calving rates at Columbia Glacier have since been decreasing (Pfeffer, 2013b). Between 2010 and 2013 the average ice flux into the fjord was measured at 2.23 $km^3\ yr^{-1}$

(Pfeffer, 2013b), most of which came from the main branch of the glacier. Between 2011 and 2014 the average mass flux from the main branch of Columbia Glacier was measured to be 1.18 ± 0.30 Gt yr^{-1} (~1.29 km^3 yr^{-1}) (Vijay and Braun, 2017).

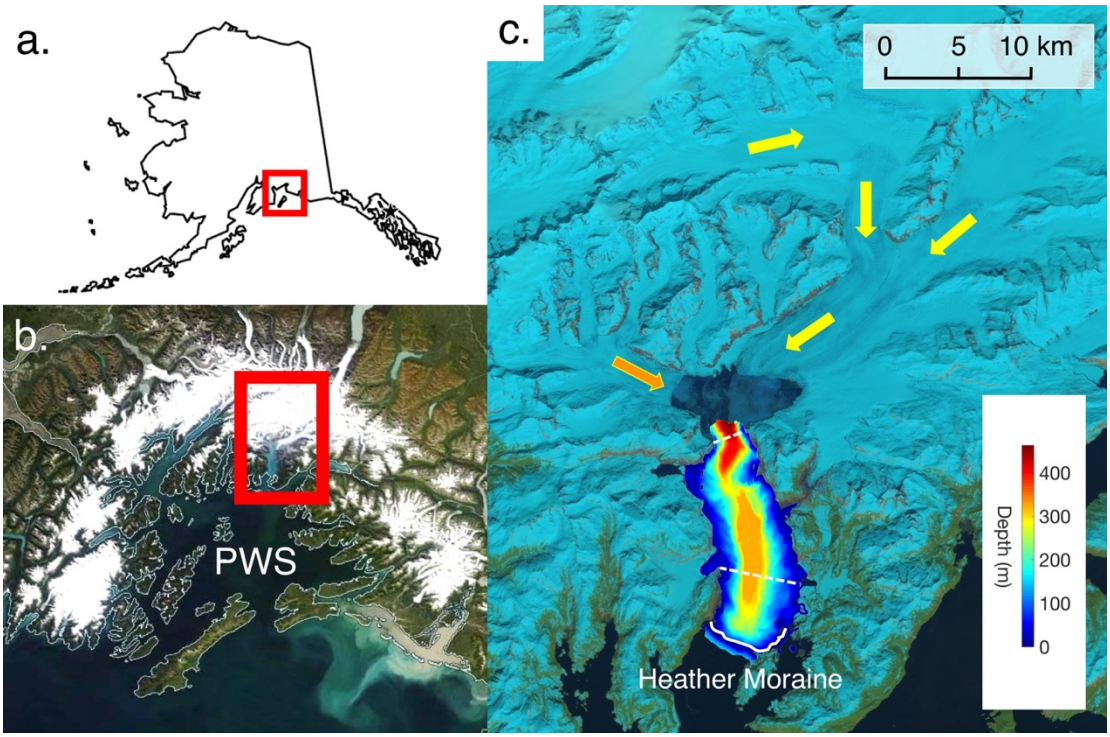

Figure 1.1: Columbia Glacier. **(a)** Outline of Alaska. **(b)** NASA MODIS image of Prince William Sound (PWS) from WorldView satellite. **(c)** Landsat image of Columbia Glacier and Fjord in 2013. Yellow arrows indicate flow of the main branch of the glacier. Orange arrow indicates flow of west branch of the glacier. Heather Island is visible along Heather Moraine. White line indicates location of Heather Moraine. Dashed lines delineate the boundaries between the Proximal Zone, the Mid-Fjord Zone, and the Distal Zone. The bathymetry, measured by NOAA Ship RAINIER in 2005, is overlain on the lower portion of Columbia Fjord.

2 Methods

2.1 Image Processing

To determine the spatial distribution of icebergs, we obtained 0.5 m-resolution, 8-bit, grayscale imagery of Columbia Fjord from the Polar Geospatial Center at the University of Minnesota. The images were taken by the WorldView satellites 1 and 2 during 2013, and georeferenced by the Polar Geospatial Center (image details shown in Table 1.1). Although the WorldView 2 satellite offered multispectral bands, we only used the higher-resolution panchromatic bands from both satellites (WorldView 1 spectrum spanned wavelengths 400 – 900 nm, and WorldView 2 spectrum spanned wavelengths 450 – 800 nm). The spread of nine dates provided seasonal coverage of the fjord, from late winter to the middle of the fall: March 13, May 6, June 10, July 11, July 12, and November 19. Note that we use the oceanographic definitions of seasons, such that winter is January-February-March, and so on in 3-month increments.

Table 1.1: Survey of images used in this study. Image processing was performed by the Polar Geospatial Center prior to our obtaining the images. Satellites used were WorldView 1 and 2 (WV1, WV2). Projection is NAD83. *Time reported in AKDT despite daylight savings ending on November 3.

Reference ID	Date, 2013	Alaska Daylight Time	Sensor	Coverage	Number of Images in Mosaic
March 13	March 13	13:14:44	WV1	Full	2
May 06a	May 06	13:32:05	WV2	Full	3
May 06b	May 06	13:33:02	WV2	Partial	2
June 10a	June 10	13:20:07	WV1	Full	3
June 10b	June 10	13:20:52	WV1	Full	3
July 11	July 11	12:51:12	WV1	Partial	3
July 12a	July 12	14:03:23	WV2	Full	3
July 12b	July 12	14:04:23	WV2	Full	3
November 19	November 19	13:07:18*	WV1	Full	2

To image large swaths, the WorldView satellites capture multiple overlapping images at once. We mosaiced these overlapping images taken simultaneously or within hundredths of a second to provide complete coverage of the fjord, with the exception of July 11 and May 06b. For several of the dates a second set of images were taken one minute later, for the purposes of stereo imagery. We distinguish between the two sets of images by labelling the first image mosaic 'a' and the second 'b'. Because the icebergs likely remain unchanged between these sets of images, the differences in iceberg identification between 'a' and 'b' images potentially result from changes in reflectivity of the open ocean due to the two distinct satellite viewing angles. Changing the angle at which we view the ocean changes the reflectivity of the ocean, which could therefore affect which pixels were identified as ice versus water. We used these pairs of images to constrain the error on our iceberg identification method.

We consider the fjord to be the area bounded by the shores of the fjord, the glacier termini, and Heather Moraine (covering a total area of ~87 km^2). Because of the shallow water depths above Heather Moraine, it is a natural barrier separating Columbia Fjord from Prince William Sound. In addition, the shallow depths cause large icebergs to run aground, allowing for easy identification of the submarine moraine in the satellite imagery.

To identify and locate icebergs in each image we created a thresholding algorithm using the MATLAB image processing toolbox that identified potential iceberg areas based on pixel intensity value. Icebergs had higher pixel brightness

values than the darker fjord waters, thus we set a threshold brightness value above which pixels were classified as icebergs and below which they were classified as water. Because frequency histograms of pixel brightness did not reveal a bimodal pattern, we therefore chose a threshold value of 41 out of 255, which corresponded with the highest pixel value for open ocean identified through visual inspection. The automatic iceberg recognition algorithm performance was impacted when the icebergs were surrounded by ice mélange, tiny chunks of ice derived from icebergs or the glacier terminus floating on top of the water. Since the mélange was brighter than the water, but darker than the icebergs, we were able to mitigate this by adjusting the threshold value in those areas until we reached a more realistic discrimination of icebergs based on visual inspection. We manually inspected the automatically-selected icebergs to quantify the reliability of automatic iceberg detection. We treat visual inspection as the 'gold standard' because the human observer can use textural and contextual information in addition to brightness alone. However, we opt for an automatic detection of icebergs for this study because mapping of all icebergs by visual inspection would be prohibitively time consuming. An example of iceberg identification by the algorithm is shown in Fig. 1.2b.

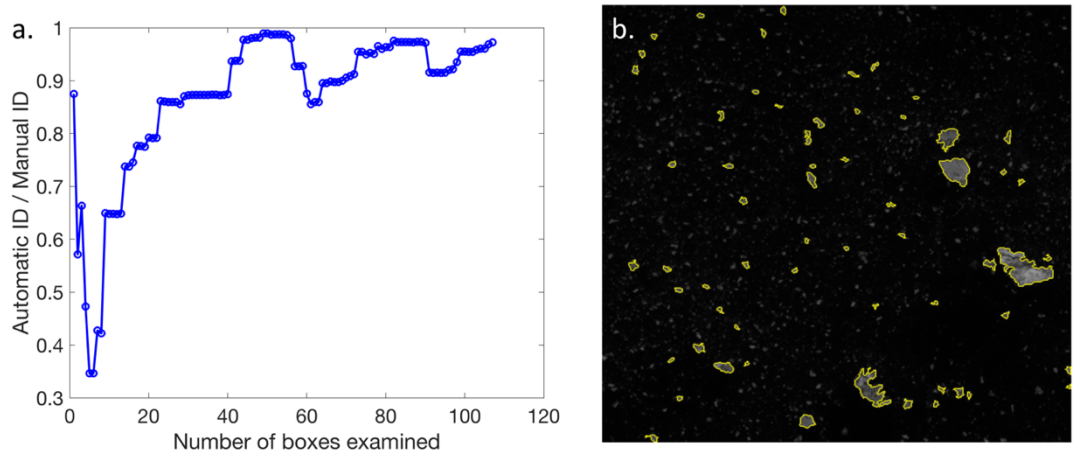

Figure 1.2: (a) The ratio of automatic iceberg detections to manual iceberg detections as a function of the cumulative number of test boxes counted (each box is 250 x 250 pixels). The total number of test boxes counted was 107. **(b)** Example of iceberg detection by algorithm. Gray 'blotches' not outlined in yellow are too small to be identified as icebergs, and are thus classified as mélange.

In addition to defining the pixel intensity threshold, we set upper and lower bounds on the iceberg area, with the lower bound corresponding to the smallest group of pixels we could visually identify as an iceberg (20 pixels, or 5 m^2) and the upper bound corresponding to the number of pixels in the largest iceberg we found visually (112,000 pixels). We set an upper bound on iceberg size to prevent large areas of ice mélange being identified as a single iceberg. The term 'iceberg' in this study refers to icebergs (>15m across as defined by the Canadian Ice Service, or >3000 ft^2 [278 m^2] in area as defined by the US National Ice Service), as well as growlers and bergy bits (glacially-derived ice in the ocean that is smaller than an iceberg as typically defined by the previously mentioned Ice Services).

To quantify the error on iceberg identification, we compared the results of the manual and automatic iceberg identification. We divided each mosaic into a test grid,

with each test cell being 250 by 250 pixels (~125m x 125m, or roughly half the area of the largest iceberg). We then randomly selected test cells on each of the mosaics and counted the number of icebergs by eye and using the thresholding code. After examining a total of 107 grid cells, we found that the algorithm identified 95 ± 4 % of the icebergs identified by an observer. Occasionally, when icebergs were close together, the algorithm would categorize them as a single iceberg, leading to the under-identification of the number of icebergs. To verify if we had counted enough cells, we divided the cumulative number of icebergs identified by the algorithm in cells 1 through N (where N is the number of test cells counted) by the cumulative number of icebergs identified manually (cells 1 through N) (Fig. 1.2a). This value plateaued for N≥44. We used the mean and the standard deviation of the line between N=44 and N=107 as our estimate of iceberg identification error. Error in automatic iceberg identification was greater in mélange-covered areas than open ocean. We found that the algorithm identified 67 ± 6 % of the icebergs in the areas of ice mélange. To assess the amount of mélange present in Columbia Fjord, we examined the pixels identified as ice, but not counted as icebergs. The area of the fjord covered by mélange ranged from 1.1 ± 0.12 to 9.9 ± 0.79 % (Table 1.4).

In addition to quantifying the error in the number of icebergs identified, we estimated the error on the area of the icebergs by comparing the total area of icebergs calculated by the algorithm. For June 10a and June 10b, the difference in total iceberg area amounted to less than 8% of the total calculated iceberg area for each image. For July 12a and July 12b, that difference amounted to less than 4%.

2.2 Overall Iceberg Distributions

To examine the spatial distribution of icebergs inside the fjord, we created a time-integrated map of iceberg density. We divided the fjord into 500 m x 500 m squares and counted the number of icebergs whose centroids were present within each square. Overlaying the results from March 13, June 10a, July 12a, and November 19, we created a map which depicted the locations of all the icebergs identified during our study (Fig. 1.3a). We created a similar map of cumulative area of icebergs whose centroids resided in each square (Fig. 1.3b).

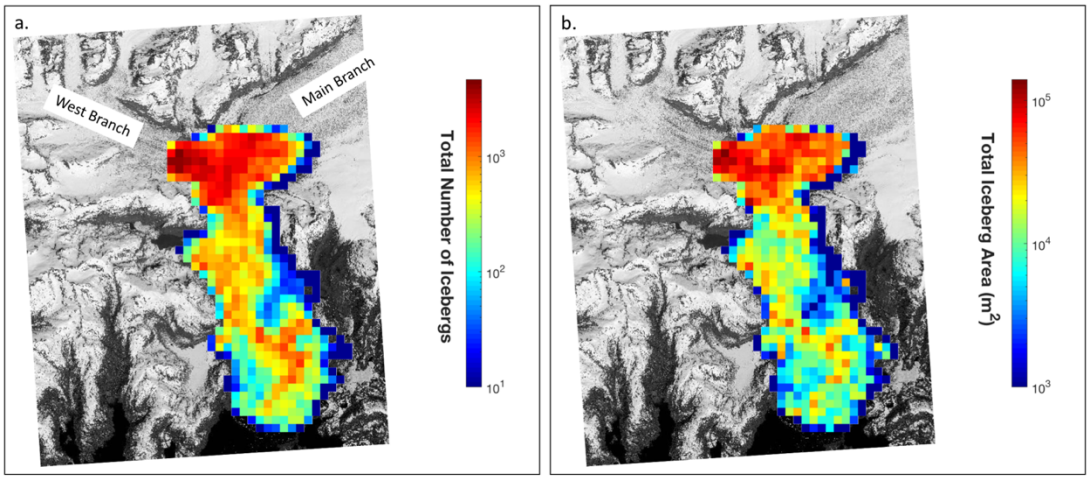

Figure 1.3: Cumulative iceberg population density and area map. Each grid cell represents a 500m x 500m square. The scenes from March 13, May 06a, June 10a, July 12a, and November 19 were overlain to obtain the total number and area of icebergs inside each grid cell. Data is overlain on a satellite image of the fjord taken by WorldView 1 on June 10, 2013. **(a)** number of icebergs in each grid cell **(b)** area of icebergs inside each grid cell.

2.3 Along Fjord Iceberg Distributions

To examine the variation in spatial distribution of icebergs between scenes, we divided the fjord longitudinally into evenly spaced sections roughly one kilometer

in length starting from the terminus to Heather Moraine. The icebergs were binned into those sections based on the location of their centroids. In some of our analyses, we needed a larger sample size of icebergs, so we also divided the fjord into three geographic sections (Fig. 1.1), which are based on fjord geometry. The "Proximal Zone" spans from the terminus of the glacier to the first major constriction, the "Mid-Fjord Zone" spans from the constriction to the inlet on the east side of the fjord, roughly two-thirds of the way downfjord, and the "Distal Zone" spans from the inlet to Heather Moraine.

Following the methodology established in prior similar studies, we fit a power-law equation of the form $Pr(A > a) = bA^m$ to iceberg areas in each of the three zones to determine the iceberg size-distribution (Kirkham et al., 2017; Sulak et al., 2017; Tournadre et al., 2016). $Pr(A > a)$ represents the number of icebergs whose waterline cross-sectional area, A, is greater than a while b and m are the constants which are constrained by data fitting. We chose values of a to be multiples of 1000 from 0 to 100,000 m^2, increasing the resolution of a between 0 and 1000 m^2 to include: 10, 25, 50, 75, 100, 250, 500, and 750 m^2. To determine the goodness of fit of the power-law we performed a Kolmogorov-Smirnov test. To obtain a fit with 95% confidence we had to remove the largest icebergs, which deviate from the power-law size distribution that is followed by smaller icebergs. There is often difficulty fitting the tail of the distribution due to the number of samples being too low, and removing the largest icebergs to fit the distribution has been done in other

similar recent studies (e.g. Sulak et al., 2017). An example of our power-law fit for a single image is shown in Fig. 1.4.

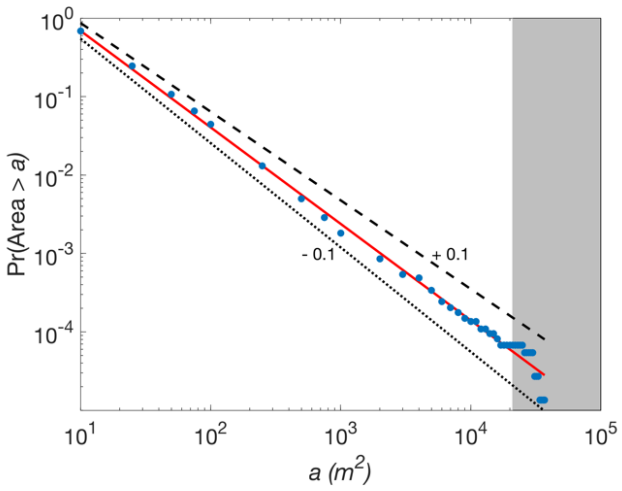

Figure 1.4: Power-law fit for the iceberg areas in the Proximal Zone on June 10b. The red line represents the best fit, and the black lines show the mismatch resulting from shifting the power exponent by ± 0.1 (the dotted line indicates a subtraction of 0.1, and the dashed line indicates an addition of 0.1). The largest icebergs that have been omitted to achieve a statistically significant fit are plotted in the gray box.

To test whether icebergs of various sizes co-vary spatially within Columbia Fjord, we separated the iceberg population into five class sizes based on their waterline cross-sectional area, which we define as the area of the icebergs visible from satellite imagery. The class size bins were spaced logarithmically (0-10 m^2, 10-100 m^2, 100-1,000 m^2, 1,000-10,000 m^2, and 10,000-100,000 m^2) with Class 1 representing the smallest icebergs and Class 5 representing the largest. For each one-kilometer bin along the fjord we compared the evolution of the different classes down the fjord by plotting the different class sizes against each other and calculating the Pearson correlation coefficient using the equation:

$$P_{C_a C_b} = \frac{cov(C_a, C_b)}{\sigma_{C_a} \sigma_{C_b}} \quad \text{Eq. (1)}$$

where cov is the covariance, σ is the standard deviation, and C_a and C_b represent the two class sizes being compared. Error bounds are given as 95% confidence intervals. We calculated the Pearson correlation coefficient using the icebergs from all scenes combined. In addition to calculating the correlation of the different size classes, we plotted the exact locations of the large icebergs (Classes 3-5) inside the fjord for each date to better understand where the large icebergs were located inside the fjord (Fig. 1.8).

2.4 Iceberg Characteristics

We used the waterline cross-sectional area of the icebergs (A) to calculate iceberg volume. We estimated iceberg volume using two previously proposed scaling laws. For the first approach we used the equation for iceberg volume (V) derived by Sulak et al. (2017):

$$V = 6.0A^{1.30} \quad \text{Eq. (2)}$$

For the second approach we assumed the icebergs to be rectangular prisms and used the proportions used by Bigg et al. (1997) where the ratio of iceberg length to width is equal to 1.5:1, the keel to the width ratio equal to 1:1, and the keel to freeboard ratio equal to 5:1. The equation relating area to volume using these dimensions is:

$$V = 0.98A^{1.5} \quad \text{Eq. (3)}$$

We also used the dimensions outlined in Bigg et al. (1997) to estimate keel depth (k) and underwater surface area (SA) of the icebergs:

$$k = 0.67A^{0.5} \quad \text{Eq. (4)}$$

$$SA = \frac{11}{3}A \quad \text{Eq. (5)}$$

We calculated the relative increase in the fjord albedo due to the presence of ice for each scene by assigning an albedo of 0.60 for each pixel identified as ice (Zeng et al., 1984) and 0.060 for the remaining pixels representing ocean surface. In this way, icebergs as well as mélange were accounted for in the ice fraction. The selected albedo of fjord water is the monthly averaged albedo for ocean water surface for the months of April, May, June, August, and September for the latitude of Columbia Fjord (Payne, 1972). We calculated albedo using this method to avoid problems with atmospheric influence on albedo calculations made from satellite imagery as well as to ignore the influence of solar angle on the ocean albedo whilst illustrating the impact of ice in the fjord on fjord albedo.

3 Results

3.1 Overall Iceberg Distributions

During 2013, the majority of icebergs were found within the first 5 km of the terminus, corresponding to the area of the fjord prior to where the fjord coastline pinches in and forms a constriction (Fig. 1.3a). Beyond the constriction, the number of icebergs drops steeply (Fig. 1.3a). Iceberg area followed a similar pattern, with the majority of iceberg area in the first 5 km from the terminus, followed by a rapid decline in total iceberg area on the other side of the constriction (Fig. 1.3b and Fig. 1.5). All scenes show a peak in the total iceberg area not directly adjacent to the

terminus, but 2 to 5 kilometers away. Most icebergs were small; over 95% of all the icebergs identified in this study had a waterline cross-sectional area of 100 m^2 or less (Classes 1 and 2). The mélange coverage in the spring and fall months was similar ($2.8 \pm 1.8 \times 10^6$ m^2), whereas the mélange coverage in the summer months was $9.1 \pm 0.8 \times 10^6$ m^2.

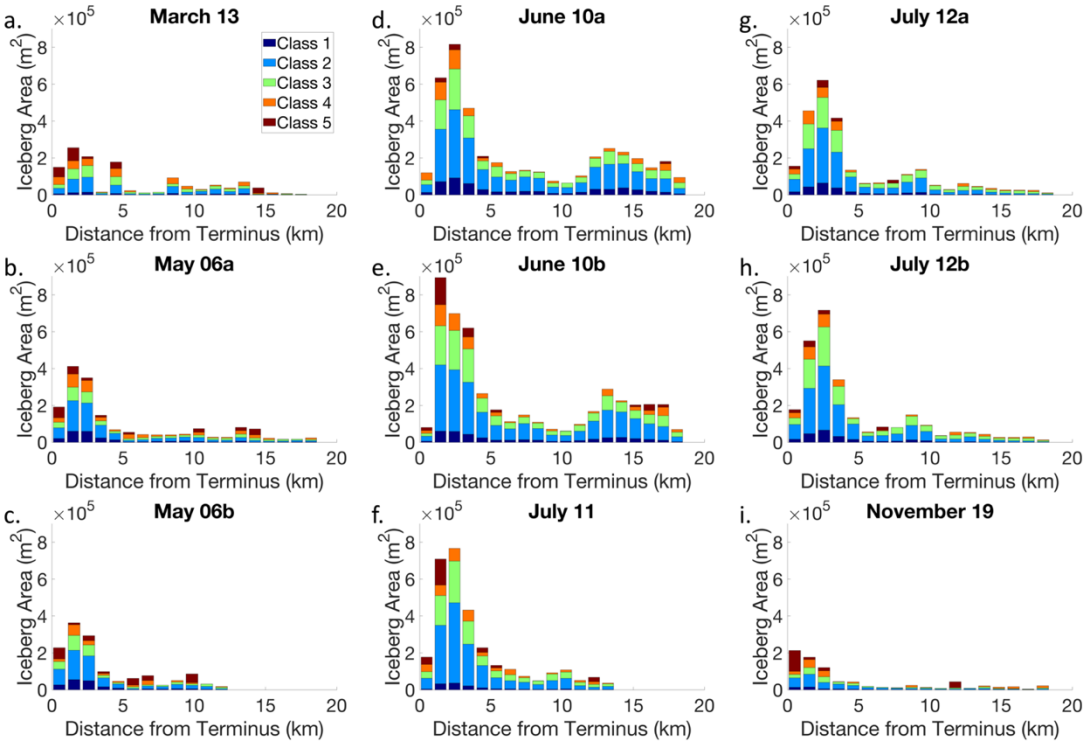

Figure 1.5: Total area of icebergs per 1-km bin along the fjord. The dates shown here are **(a)** March 13, **(b)** May 06a, **(c)** May 06b, **(d)** June 10a, **(e)** June 10b, **(f)** July 11, **(g)** July 12a, **(h)** July 12b, and **(i)** November 19. The peak of ice coverage inside the fjord is found 2-3 km from the terminus. The icebergs are divided into classes by waterline cross-sectional area, with the smallest icebergs residing in Class 1 and the largest in Class 5. The divisions for the bins were: 0-10 m^2, 10-100 m^2, 100-1,000 m^2, 1,000-10,000 m^2, and 10,000-100,000 m^2.

3.2 Along Fjord Iceberg Distributions

The exponents from the power-law equations fit to the iceberg size distributions reveal patterns in both the spatial and seasonal size distributions of icebergs inside the fjord (Fig. 1.6). The power exponent represents the relative abundance of large versus small icebergs, with more negative power exponent values indicating a higher proportion of small icebergs. The power exponents for the spring and fall months were similar, whereas the power exponents were more negative for the summer scenes. The power exponent for the spring and fall months ranged from -1.22 ± 0.03 to -0.91 ± 0.02 with a mean of -1.08. In the summer scenes, the power exponent ranged from -1.54 ± 0.03 to -1.12 ± 0.07 with a mean of -1.35. Every scene showed a decrease in the power-law exponent from the Proximal Zone to the Mid-Fjord Zone (indicating a decrease in the proportion of large icebergs with distance from the glacier terminus) and a subsequent increase in the power-law exponent from the Mid-Fjord Zone to the Distal Zone (indicating an increase in the proportion of large icebergs near Heather Moraine). The average decrease in the power exponent from the Proximal-Fjord to the Mid-Fjord Zone was 0.16, and the average increase from the Mid-Fjord Zone to the Distal Zone was 0.24.

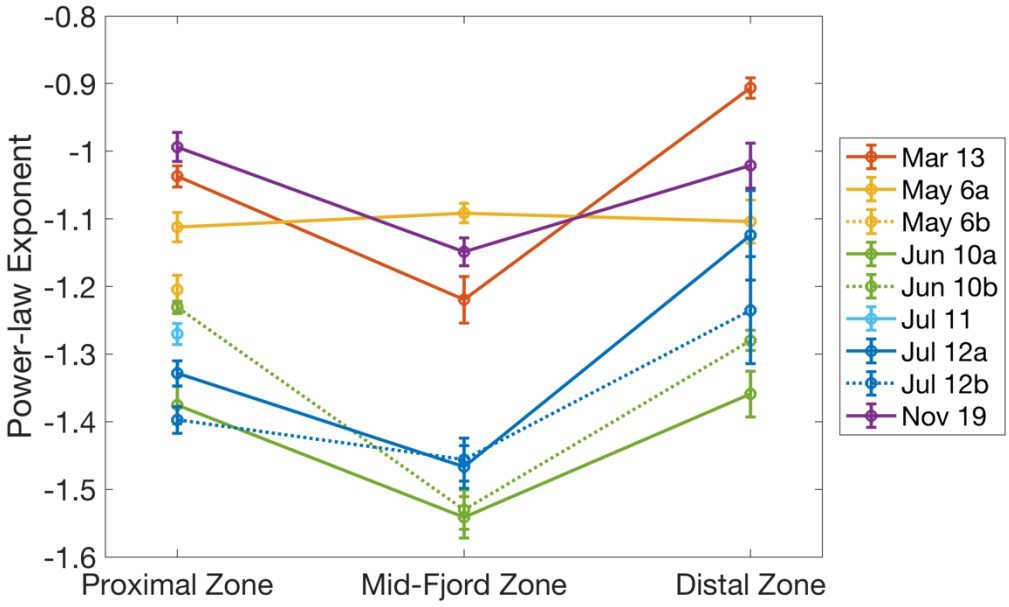

Figure 1.6: Power-law exponent calculated for each scene. Power-law exponents indicate both a spatial and seasonal changes in iceberg distribution. The more positive exponent in the Proximal and Distal Zones indicate a higher proportion of large icebergs present near the terminus and Heather Moraine. Additionally, the more positive exponent for the spring and fall scenes indicates a higher proportion of large icebergs present in those respective seasons. The anomalous increase in the power exponent in the mid-fjord zone for May 6a is due to contamination from cloud cover.

We calculated the spatial correlation of the different iceberg size classes along the fjord to reveal similarities and differences in iceberg evolution down the fjord. The correlation coefficient reflects the spatial covariance of different iceberg size classes. We performed these calculations for each scene individually, and for all identified icebergs combined. Our results show that the largest iceberg class, with a waterline cross-sectional area between 10,000 and 100,000 m^2, is the least spatially correlated with the other classes (correlation coefficient ranging between $0.344^{+0.131}_{-0.146}$ and $0.490^{+0.111}_{-0.129}$; Table 1.2). The fact that the largest icebergs behave differently

along the fjord than the other icebergs further justifies removing the largest icebergs from the dataset when fitting the power-law equation for size-frequency distribution. In contrast, the other class sizes are highly spatially correlated with each other (correlation coefficients ranging between $0.814^{+0.047}_{-0.061}$ and $0.980^{+0.005}_{-0.007}$; Table 1.2). After calculating the spatial correlation of the iceberg classes for each scene independently, we determined that the correlation does not appear to be seasonally variable.

Table 1.2: Correlation between different iceberg class sizes along the fjord for all scenes combined. The red shading corresponds to the size of the error estimates, with the darker shades of red representing larger error. Upper and lower limits on the 95% confidence interval are reported in the lower half of the table.

Size Classes	1	2	3	4	5
1		0.900	0.861	0.814	0.344
2	+ 0.026 - 0.035		0.980	0.845	0.398
3	+ 0.036 - 0.047	+ 0.005 - 0.007		0.867	0.396
4	+ 0.047 - 0.061	+ 0.040 - 0.052	+ 0.034 - 0.045		0.490
5	+ 0.131 - 0.146	+ 0.124 - 0.141	+ 0.125 - 0.141	+ 0.111 - 0.129	

3.3 Iceberg Volume and Effects on the Fjord

The two approaches we used to calculate iceberg volume yielded slightly different results (see Table 1.3). Generally, the volume calculations using Eq. (3) were larger than the volume calculations using Eq. (2). Both approaches showed that

the icebergs with waterline surface areas greater than 1000 m^2 accounted for the majority of the total ice volume present in each scene. Using Eq. (3), the percentage of ice volume that the large icebergs contained ranged from 53% to 88%, and using Eq. (2), the percentage of ice volume that the large icebergs contained ranged from 35% to 74%. The differences in iceberg volume found by the two methods are due to the differences in iceberg geometry assumed by these equations. Importantly, the variations in total volume and the proportion of iceberg volume in large icebergs are similar for both approaches, despite the different assumptions in iceberg geometry.

Table 1.3: Volume of icebergs in Columbia Fjord for each scene, calculated using Eq. (2) and Eq. (3). * Imagery of fjord is incomplete on these dates.

Date	Equation (3)			Equation (2)		
	Total Volume of Icebergs	**Volume of Icebergs: Area > 1000m^2**	**Percent Volume of Icebergs with Area > 1000m^2**	**Total Volume of Icebergs**	**Volume of Icebergs: Area > 1000m^2**	**Percent Volume of Icebergs with Area > 1000m^2**
Units	km^3	km^3		km^3	km^3	
March 13	0.077	0.065	84	0.060	0.042	70
May 06a	0.083	0.067	81	0.070	0.045	65
May 06b*	0.070	0.058	83	0.056	0.036	64
June 10a	0.10	0.055	53	0.12	0.042	35
June 10b	0.16	0.11	67	0.16	0.071	46
July 11*	0.12	0.089	72	0.11	0.054	50
July 12a	0.072	0.042	58	0.077	0.029	38
July 12b	0.074	0.041	56	0.079	0.029	36
November 19	0.057	0.050	88	0.042	0.031	74

The estimated increase in albedo due to the presence of icebergs for Columbia Fjord ranged from 1.2% to 9.8% (Table 1.4). The albedo increase was highest in the summer months, corresponding to the increased presence of ice inside the fjord.

Table 1.4: Increase in albedo of the entire fjord surface due to the presence of ice and mélange, calculated for each scene. Both icebergs and mélange are taken into account for albedo calculations. * Imagery of fjord is incomplete on these dates.

Date	Relative Albedo Increase (%)	Percent Mélange Coverage (%)
March 13	2.5 ± 0.95	2.7 ± 0.25
May 06a	4.8 ± 1.8	6.0 ± 0.50
May 06b*	4.0 ± 1.5	2.8 ± 0.24
June 10a	9.8 ± 3.7	11 ± 0.99
June 10b	9.6 ± 3.6	11 ± 0.96
July 11*	6.2 ± 2.3	4.0 ± 0.44
July 12a	7.7 ± 2.9	9.9 ± 0.79
July 12b	7.4 ± 2.8	9.1 ± 0.73
November 19	1.2 ± 0.46	1.1 ± 0.12

To evaluate the potential for icebergs to affect fjord waters, we estimated the iceberg residence time inside the fjord. The bulk iceberg residence time for each image is the total volume of icebergs inside the fjord divided by the average annual calving rate for both arms of Columbia Glacier (Pfeffer, 2013b). The average residence time over all images was 14 ± 6 days using Eq. (2) to calculate iceberg volume, and 15 ± 6 days when using Eq. (3).

4 Discussion

4.1 Overall Iceberg Distributions

Our data reveal spatial patterns in iceberg distribution in Columbia Fjord in 2013. In general, iceberg coverage decreases with distance from the terminus. The

observed peak in iceberg ice coverage 2 to 5 km from the terminus (Fig. 1.5) is somewhat surprising given that icebergs originate at the terminus, and it would be logical to expect the highest concentration of icebergs to be immediately adjacent to the terminus. Potential explanations for this are that the kinetic energy associated with the calving process or that the inflow of subglacial meltwater at the grounding line pushes icebergs away from the terminus. Furthermore, only the summer months showed peak iceberg concentration away from the terminus (normalizing total iceberg area to bin area), pointing to a causal role for subglacial meltwater discharge, which is higher in the summer. Alternatively, these patterns of ice concentration in the fjord could be the result of influx of icebergs from the west arm of Columbia Glacier. Figures 1.3a and 1.3b show an increase in both the number and area of icebergs in the location where the west arm of Columbia Glacier contacts the fjord. Additionally, ocean circulation patterns within the fjord could be driving these patterns of ice congregation. Near the terminus the fjord is wide, but roughly 4 to 6 km downfjord it narrows to ~2 km before expanding out to a consistent width of ~4.5 km until Heather Moraine. This change in geometry may drive ocean circulation that concentrate icebergs 2-5 km from the terminus.

In addition to these spatial patterns there were seasonal differences in iceberg coverage in Columbia Fjord in 2013, with more icebergs present during the summer months than the spring or fall (Fig. 1.5). This is consistent with an increase in calving rates caused by warmer air and water temperatures. Warmer fjord waters may increase the rate of submarine melt, which then increases the iceberg calving rates

(Luckman et al., 2015; O'Leary and Christoffersen, 2013). In addition, surface meltwater caused by warmer air temperatures can aid the formation of icebergs by infiltrating and enlarging crevasses at the terminus (Van Der Veen, 1998; Weertman, 1973). These processes may all work together to produce increased ice discharge during warm summer months as opposed to the late winter and fall. In calculating the calving rate of Columbia Glacier in 2013, Vijay and Braun (2017) show an increase in the calving rate from March until June/July, followed by a decrease in the calving rate for the remainder of the year. This increased ice discharge would explain increased iceberg coverage during the summer.

4.2 Along Fjord Iceberg Distributions

We fit power-law distributions to the data to gain insight – both seasonally and spatially – into the size-distributions of icebergs inside the fjord. Fitting a power-law distribution to the data allows us to more quantitatively understand the spatiotemporal differences in iceberg size distribution because power-law exponents reflect the relative abundance of small icebergs versus large icebergs. Our iceberg distributions were better described by a power-law distribution than by a lognormal distribution, which is consistent with the conclusion from Kirkham et al. (2017) that icebergs near the calving front tend toward a power-law distribution, and icebergs further out in the open ocean fit a lognormal distribution. The decrease in power-law exponents from the Proximal Zone to the Mid-Fjord Zone indicates a decrease in the relative proportion of large icebergs from the Mid-Fjord Zone to the Proximal Zone.

This is unsurprising given that we would expect icebergs to melt or fracture rather than grow as they travel from the terminus (Fig. 1.6). The proportion of large icebergs increases in the Distal Zone (shown by the increase in power-law exponents between the Mid-Fjord and Distal Zones), which is interpreted to be due to grounding of icebergs on Heather Moraine, which is at most 25 m below the sea surface (Pfeffer, 2013a; Walters et al., 1988). The larger icebergs become grounded until they have melted or broken up sufficiently to pass over, are pushed over by strong winds, or are able to pass during high tides (Pfeffer, 2015).

Power-law exponents also indicate that there is a greater proportion of smaller icebergs present throughout the fjord in the summer months, including within the Proximal Zone near the terminus. This could indicate that the glacier calves smaller icebergs in the summer. During the summer when air temperatures are higher, meltwater is ubiquitous along the surface of the glacier and can help break calving ice into smaller pieces through hydrofracturing (Van Der Veen, 1998). Alternatively, the icebergs could be more prone to melt and fragmentation during the summer, which would lead to the increase of small icebergs in the Proximal Zone. The power-law exponents found in the summer months were very close to -1.5, which has been shown both experimentally and theoretically to be indicative of dominant brittle fragmentation (Åström, 2006; Spahn et al., 2014). Previous studies examining iceberg size distributions resulting from fragmentation have also calculated power-law exponents close to -1.5 (Bouhier et al., 2018; Crawford et al., 2018; Tournadre et al., 2016). The warmer summer conditions in Columbia Fjord could be responsible

for the increased iceberg fragmentation. For all the environmental parameters examined in their study, Bouhier et al. (2018) found that sea surface temperature was the most highly correlated with iceberg fragmentation rates.

We compared the power-law exponents from Columbia Glacier to those calculated for other glaciers to determine the factors that influence iceberg size distribution. Sulak et al. (2017) reported a power-law exponent of -2.00 ±0.06 for Sermilik Fjord, a power-law exponent of -1.87 ±0.05 for Rink Isbrae Fjord, and a power-law exponent of -1.62 ± 0.04 for Kangerlussuup Sermia Fjord. Kirkham et al. (2017) reported a power-law exponent of -2.4 for the icebergs near the calving front of Jakobshavn Isbrae, Ilulissat Icefjord. These studies found their power exponents using the icebergs in the entire fjord. Therefore, we also calculated the power exponent for the entire Columbia Fjord, and averaged our results from each image to produce a value of -1.26 ± 0.05 for the entire study. Our results combined with results from these previous studies show no discernible relationship between power-law exponents and seawater temperatures; however, there is a relationship between power-law exponents and average annual calving flux (Fig. 1.7) (Howat et al., 2011; Sulak et al., 2017; Vijay and Braun, 2017). A higher calving flux corresponded to a more negative power-law exponent; glaciers with higher discharge rates had higher proportions of small icebergs. This supports the hypothesis of Sulak et al. (2017) that the power-law exponent could be an indicator of glacier productivity, i.e. calving rate.

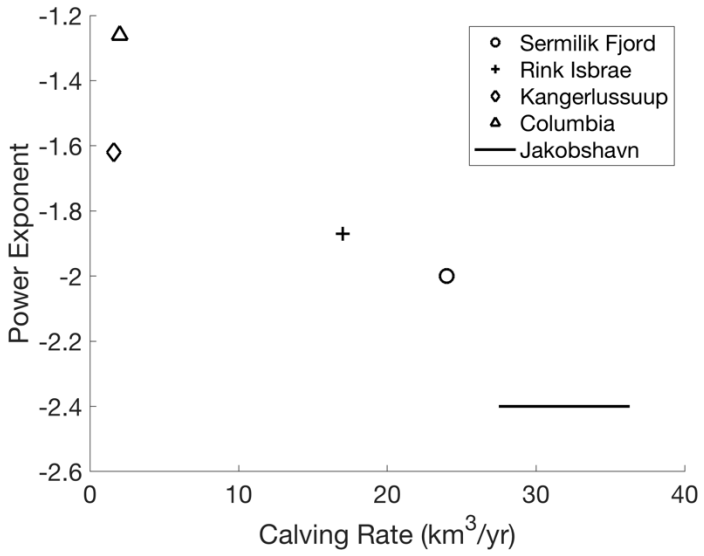

Figure 1.7: A comparison of published power exponents and glacier calving rates. (The power-law exponent for Columbia Fjord was calculated in this study.) An increase in the calving rate corresponds with an increase in the proportion of small icebergs present inside the fjord (more negative power exponent).

In calculating the spatial correlation of icebergs inside the fjord, we found that the majority of icebergs followed similar spatial patterns, but that the largest iceberg class was not strongly spatially correlated to any of the other size classes. The largest icebergs contain the majority of the ice inside the fjord, yet they behave differently than the remainder of the iceberg population. Our interpretation of this lack of correlation is that the largest icebergs are running aground on the shallower areas of the fjord, which decouples their spatiotemporal evolution from the smaller icebergs that tend to float more freely and evolve together as they move downfjord. Bathymetric surveys (McNabb et al., 2012a) show that in addition to being shallow along the sides and at Heather Moraine, the fjord contains areas near the glacier terminus with depths around 75 m which are able to ground icebergs with waterline

cross-sectional areas larger than roughly 8,500 m^2 [Eq. (4)]. We found that the largest icebergs were located in those shallower areas (Fig. 1.8).

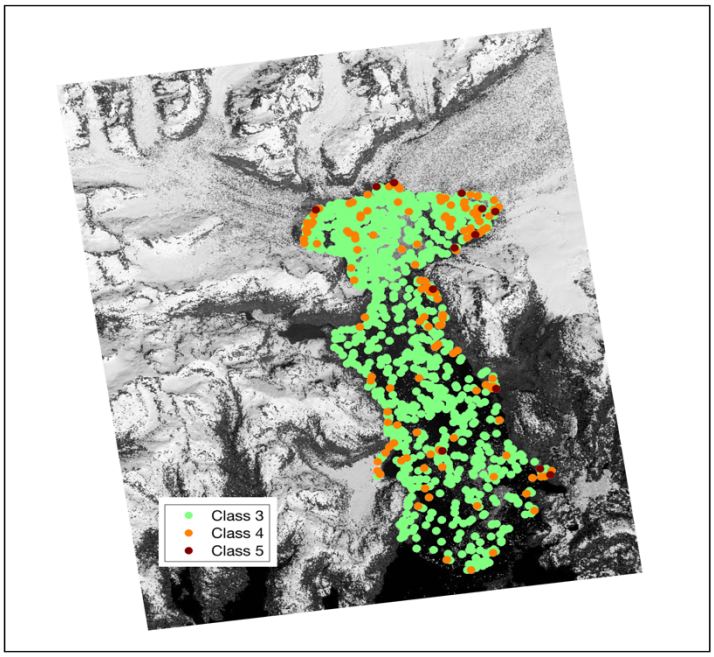

Figure 1.8: Location of large icebergs by centroid (May 06a). Icebergs in Class 3, Class 4, and Class 5 have waterline cross-sectional areas of 100 – 1,000 m^2, 1,000 – 10,000 m^2, and 10,000 – 100,000 m^2 respectively. The background satellite image was taken by WorldView 1 on June 10, 2013.

4.3 Iceberg Effects on the Fjord

Our findings of iceberg distribution throughout the fjord have direct implications for the locations of freshwater input. In contrast to riverine fluxes, freshwater fluxes from icebergs can be spatially distributed throughout the fjord; in contrast to precipitation, these fluxes may be spatially concentrated by factors such as wind stress, ocean currents and bathymetry (Bigg et al., 1997). These factors are reflected in the cumulative distribution of icebergs shown in Fig. 1.3. The sinuosity of

the iceberg density in the Distal Zone is likely related to wind stress or ocean current patterns as there are no related bathymetric features. As melt rate is related to the velocity differential between iceberg velocity and ocean current velocity, either high wind stress or ocean currents could produce velocity differentials that increase melt rates (Bigg et al., 1997). Thus, the sinuous iceberg density feature may be associated with elevated freshwater fluxes relative to other regions of the fjord.

In contrast, the presence of large icebergs along the coasts and at Heather Moraine (Fig. 1.8) is best explained by their grounding on bathymetric features. While a majority of the icebergs examined in this study were located within the first five kilometers of the fjord (Fig. 1.3b), the largest icebergs also tended to be grounded in the shallow areas of the fjord, namely along the coasts and at Heather Moraine (Fig. 1.8). Where large icebergs run aground, they release freshwater by melting until they shrink and unground by melting or fracture. Thus, unless fracture processes are dominant, large icebergs may release significant volumes of freshwater over small areas of the fjord. Large icebergs – icebergs with a waterline cross-sectional area greater than 1000 m^2 (Classes 4 and 5) – accounted for less than one percent of the number of icebergs present in the fjord, yet they made up 53-88% of the total iceberg volume in the fjord [Eq. (3)], which is a reflection of the power-law distribution. Freshwater fluxes from these icebergs can have implications for ocean mixing, fjord circulation, and the local ecology (Helly et al., 2011).

To assess the icebergs' impact on fjord water mass characteristics, we compared temperature and salinity profiles – collected July 30-31, 2013 (Arimitsu et

al., 2017) – to iceberg keel depth (Fig. 1.9). These profiles show a vertical structure characterized by a diurnally heated surface layer (ca. 1-13 ºC), a mixed layer (ca. 4 ºC and 26-30 PSU), and a deeper layer (ca. 5 ºC and 30 PSU). The salinity of the surface layer is highly variable (ca. 20-26 PSU). The mixed layer is cooler and fresher than the deeper layer and extends to a depth of ca. 30m in the Mid-Fjord and Distal Zones and ca. 60m in the Proximal Zone. Iceberg keel depths are generally coincident with the depth of the mixed layer; 99% of all iceberg keel depths are found within the mixed layer. While it may be a coincidence that the iceberg keel depth is related to the mixed layer depth, there are a few possible causal relationships to consider. The inverse relationship between salinity and number of iceberg keels present could be the result of freshwater from iceberg melting. This freshwater provides a buoyant flux that may significantly enhance vertical mixing from the depth of the iceberg toward the surface (Helly et al., 2011). Additionally, icebergs could mechanically mix the water column by shear produced during iceberg overturning and by current drag against the iceberg surfaces. This could be a significant process at Heather Moraine, where grounded icebergs alter the flow of water in and out of the fjord. Further evidence for iceberg influence on fjord waters at Heather Moraine is that the salinity profiles taken just outside Heather Moraine are ca. 5 PSU higher than directly inside the fjord (Arimitsu et al., 2017).

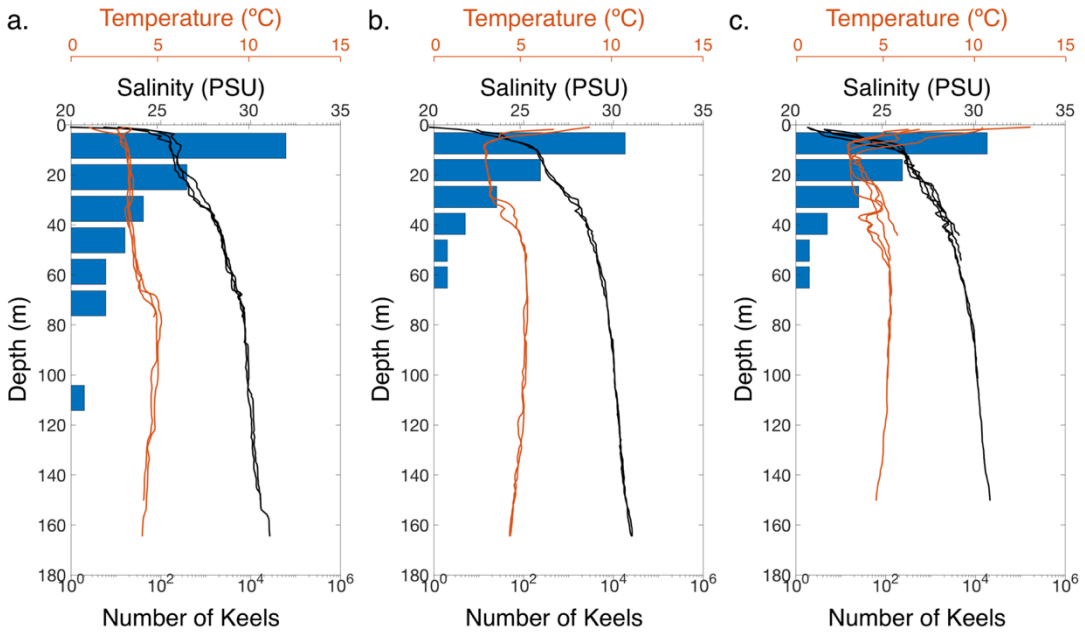

Figure 1.9: Iceberg keel depths compared to salinity and temperature profiles in Columbia Fjord. Salinity and temperature profiles were collected by the US Geological Survey on July 30 and 31, 2013. Keel depths presented here are from the July 12a icebergs. **(a)** Proximal Zone **(b)** Mid-Fjord Zone **(c)** Distal Zone. Note the log axis for number of keel depths.

To further assess the icebergs' effect on fjord characteristics, we consider iceberg melt. However, because our images are taken too far apart to track individual icebergs, we cannot directly measure iceberg deterioration. In addition, we cannot calculate iceberg melt rates for all dates using previously published equations due to lack of information of iceberg velocity and fjord water velocity. We therefore estimate an "effective iceberg melt rate" by dividing contemporaneous calving rate calculated in Vijay and Braun (2017) by the underwater surface area calculated using Eq. (5). The effective iceberg melt rate simply represents the rate of iceberg melting that would be required to balance the calving rate given the estimated underwater surface area of the icebergs. Because we lack information about iceberg surface

roughness, we neglect it with the consequence that our surface area calculations are an underestimate, and hence, our calculations of iceberg melt rates are an overestimate. Surprisingly, the effective iceberg melt rates were lowest in the summer months (0.30 ± 0.02 m day^{-1}) and highest in the spring (0.84 ± 0.11 m day^{-1}).

To examine what factors might be responsible for this unexpected result, we used the equation for turbulent iceberg basal melting (M_b) presented in Bigg et al. (1997):

$$M_b = 0.58\,\Delta V^{0.8}\,\frac{\Delta T}{L^{0.2}} \qquad \text{Eq. (6)}$$

Where ΔV is the difference between iceberg velocity and fjord water velocity, ΔT is the temperature difference between the surface ice temperature – assumed here to be the melting point of ice – and the temperature of fjord water, and L is the along-fjord length of the iceberg. We examined both the median and maximum iceberg length for each date to evaluate the influence of L, but the differences in the iceberg melt rates were negligible because L is raised to the power of 0.2. Normalizing ΔV, ΔT, and L by the variables in the July 12a scene (the date closest to the date on which the CTD measurements were taken in the fjord) allows us to examine the relative importance of temperature or velocity differential on iceberg melt rates. If we make the end-member assumption that ΔV remains constant throughout the year and use the observed July 30 seawater temperature of the mixed layer (3 ºC), (Fig. 1.9), it follows that water temperatures in the spring would have to be higher (8.0 ± 1.1 ºC) than in summer (2.8 ± 0.19 ºC), which is contrary to what is expected. Given this analysis, we attribute the spring increase in iceberg melt rate mainly to increased current shear

between icebergs and the surrounding waters (ΔV), which is consistent with previous studies which found higher iceberg melt rates in Greenland fjords in winter due to increased shear (Moon et al., 2018b). ΔV was 3.4 ± 0.56 m s^{-1} for the spring scenes, and 0.92 ± 0.08 m s^{-1} for the summer scenes. Possible reasons for this increased winter shear could include stronger winter currents and increased iceberg grounding events due to the greater proportion of large icebergs in the winter months. The difference in temperature between icebergs and the surrounding water may be a secondary factor in enhancing melt rates in the spring, however. The temperature that matters most for iceberg melt is the temperature of the water directly adjacent to the icebergs. Most of the icebergs in this study reside in the Proximal Zone, and in the summer this water is possibly cooler due to increased subglacial discharge and runoff in the summer, as well as increased albedo (Table 1.4), leading to lower iceberg melt rates.

Finally, icebergs can affect fjord water temperatures by altering its surface reflectivity. The presence of icebergs lowers the amount of solar radiation absorbed by the fjord by increasing the overall albedo of the fjord by 1.2 ± 0.46 to 9.8 ± 3.7 %. Although this increase in albedo is small, it is mostly concentrated near the terminus because the majority of icebergs are found within five kilometers of the terminus. This may be reflected in Fig. 1.9, which shows that only the surface waters in the Proximal Zone are not subject to warming from insolation, perhaps partly due to the high concentration of reflective icebergs there.

4.4 Comparison to Greenland Fjords

Most recent investigations of icebergs in fjords have focused on the peripheries of the Greenland ice sheet (Enderlin et al., 2016; Enderlin and Hamilton, 2014; Kirkham et al., 2017; Moon et al., 2018a; Sulak et al., 2017), which share some similarities to and some differences from Columbia Fjord. One difference between our study site and a number of the sites in Greenland is the presence of winter sea ice. Sea ice formation helps create a thick mélange by preventing icebergs and bergy bits from exiting the fjord. This mélange not only increases iceberg residence time in the fjord, but also provides a back stress on the terminus that slows the rate of iceberg calving and terminus velocity (Amundson et al., 2010; Walter et al., 2012). In Greenland, winter sea ice formation is widely prevalent (Amundson et al., 2010; Higgins, 1991; Walter et al., 2012), however, sea ice was not present in any of the scenes we examined in detail. Some pancake ice was visible in a satellite image taken on March 26 which was not used in this study, however it was not thick enough to lock in icebergs or provide significant backstress on the glacier terminus. Because maximum sea ice extent in the Arctic is typically reached in March, and oceanographic definition of winter is January-February-March, we consider the March 13 scene to be representative of winter conditions in Columbia Fjord. We found that the mélange coverage was greatest in the summer months when the iceberg coverage was also greatest, however the mélange coverage only amounted to 11 ± 0.99 % (Table 1.4). Hence, ice mélange in Columbia Fjord appears to be more a function of higher summer calving rates and ice fragmentation rather than resulting

from winter-time capture of ice fragments in sea ice. The lack of ice mélange in Columbia Fjord may contribute to the relatively short residence time (a fortnight) of icebergs in this fjord compared to iceberg residence times of over 100 days in some Greenlandic fjords (Sulak et al., 2017; Sutherland et al., 2014).

Icebergs in Greenlandic fjords are often much larger than the ones observed in Columbia Fjord. The largest icebergs in our study have a waterline cross sectional area on the order of magnitude 10^4 m^2, whereas other studies have measured iceberg areas to be around 10^7 m^2 (Kirkham et al., 2017; Sulak et al., 2017). A primary reason for the smaller icebergs in Columbia Fjord is the small height of the calving front. Vijay and Braun (2017) measured the maximum thickness of the terminus to be ca. 300 m between July 2011 and July 2014. One consequence of the small icebergs is the reduced presence of icebergs that penetrate the deeper, incoming water layer.

The iceberg surface area in contact with the incoming waters (averaging $2.8 \pm 0.58 \times 10^4$ m^2 over all images) is a small fraction of the surface area of the terminus ($9.7 \pm 3.7 \times 10^5$ m^2) calculated using the ice thickness data published by McNabb et al. (2012b). This is a conservative estimate of terminus area because we do not account for the sinuosity or roughness of the terminus, which we also neglected when calculating iceberg surface area. Because we estimate the surface area of the terminus to be approximately two orders of magnitude greater than the surface area of icebergs in contact with the incoming water, we do not believe that the icebergs are contributing as much freshwater to the fjord waters as the terminus itself. However,

this should not diminish the importance of icebergs' impact on fjord circulation. We see from the temperature and salinity profiles (Fig. 1.9) that icebergs alter the water masses in the fjord system, introducing melt water and forcing mixing of the water column at Heather Moraine. But we do expect iceberg contributions to fjord dynamics to be more significant in fjords where the surface area of icebergs is much greater than the surface area of the glacier terminus.

To highlight the similarities and differences between Columbia Fjord and fjords which have been studied in Greenland, we compare temperature profiles from Columbia Fjord and Sermilik Fjord. The July temperature profiles from Columbia Fjord look similar to summer temperature profiles collected in Sermilik Fjord (Arimitsu et al., 2017; Moon et al., 2018a). Below 200 m depth in both fjords, the water temperature is ca. 4 ºC, but the temperature of the waters above that depth are a few degrees warmer in Columbia Fjord. This is significant because, unlike in Sermilik Fjord where icebergs are large enough to reach 200 m depth, the icebergs in Columbia Fjord are not large enough to reach the lower warmer layer. Another difference in the temperature profiles between these two fjords is the temperature of the surface waters. The surface temperatures in Columbia Fjord reach as high as 13 ºC, whereas the summer surface temperatures in Sermilik Fjord are close to freezing. Ice mélange and iceberg albedo likely play some role in this difference, but it is beyond the scope of this study to quantify these effects. These warmer temperatures in Columbia Fjord could be accelerating iceberg melt and fragmentation. While we do not have velocity measurements for the fjord waters nor the icebergs in Columbia

Fjord, our analysis of the effective melt rates we calculated suggest that either the velocity of the water or the velocity of the icebergs increases in the winter months compared to the summer months, resulting in greater shear between icebergs and fjord water.

5 Conclusion

In this study we have obtained constraints on the distributions of icebergs inside a large Alaskan temperate fjord with high calving fluxes. Most icebergs were found within five kilometers of the terminus, but peak iceberg frequency was reached a few kilometers away from the terminus, particularly in the summer. The iceberg distributions fit a power-law distribution as opposed to a lognormal distribution. The power-law exponents suggest that the icebergs melt or break up as they move away from the terminus, and that large icebergs run aground on Heather Moraine. More icebergs were present in the summer months, but those icebergs tended to be smaller. Because the power-law exponents for the summer images are closer to -1.5 than the exponents for the fall and spring images, we attribute the summer increase in small icebergs to intensified iceberg fragmentation by warmer fjord conditions. In addition, we find a correlation between power-law exponents and average annual calving rate, with larger calving rates resulting in increased proportions of small icebergs.

Most of the calved ice was contained within only a small fraction of large icebergs. The largest icebergs (which account for the majority of calved ice) are the least spatially correlated with the other iceberg class sizes, which we attribute to their

tendency to ground in shallow areas of the fjord – namely along the coast and on Heather Moraine. The largest icebergs have the greatest potential to cool the incoming ocean waters before they reach the terminus, however, in Columbia Fjord the surface area of the glacier terminus is thought to surpass the surface area of icebergs in contact with the incoming ocean water, rendering the iceberg cooling effect somewhat less important. The total surface area of the icebergs inside the fjord amounts to 2.9% of the terminus surface area. We expect that only the icebergs at Heather Moraine have the potential to affect the dynamics of the fjord since the shallow water column allows more contact between icebergs and the incoming water. The icebergs do have the potential to cool the outgoing upper layer of ocean waters by increasing the albedo in the summer months, and thereby decrease the solar heating.

Icebergs can affect fjord circulation through spatially distributed introduction of meltwater that is dependent on wind stress, fjord currents, and bathymetry. Ocean and wind forcings control where smaller icebergs release meltwater into the fjord, whereas fjord bathymetry controls where the largest icebergs release meltwater. Salinity and temperature profiles indicate that icebergs may influence the mixed layer depth. To examine further the influence of icebergs on fjord freshwater budget, we calculated an effective melt rate, and found that melt rates were surprisingly higher in the spring months. We speculate that this higher melt rate in the spring months is due to increased shear between icebergs and fjord water rather than increased water temperatures. Freshwater input from icebergs is typically omitted from fjord

circulation models. By helping determine the relative importance of the variables affecting the location and quantity of iceberg melt, this study informs models of glacier-ocean interactions.

Chapter 2: Did Holocene climate changes drive West Antarctic grounding line retreat and re-advance?

Abstract

Knowledge of past ice sheet configurations is useful for informing projections of future ice sheet dynamics and for calibrating ice sheet models. The topology of grounding line retreat in the Ross Sea Sector of Antarctica has been much debated, but it has generally been assumed that the modern ice sheet is as small as it has been for more than 100,000 years (Conway et al., 1999; Lee et al., 2017; Lowry et al., 2019; McKay et al., 2016; Scherer et al., 1998). Recent findings suggest that the West Antarctic Ice Sheet (WAIS) grounding line retreated beyond its current location earlier in the Holocene and subsequently re-advanced to reach its modern position (Bradley et al., 2015; Kingslake et al., 2018). Here, we further constrain the post-LGM grounding line retreat and re-advance in the Ross Sea Sector using a two-phase model of radiocarbon input and decay in subglacial sediments from six sub-ice sampling locations. In addition, we reinterpret high basal temperature gradients, measured previously at three sites in this region (Engelhardt, 2004), which we explain as resulting from recent ice shelf re-grounding accompanying grounding line re-advance. At one location – Whillans Subglacial Lake (SLW) – for which a sediment porewater chemistry profile is known, we estimate the grounding line re-advance by simulating ionic diffusion. Collectively, our analyses indicate that the grounding line

retreated over SLW 4300^{+1500}_{-2500} years ago, and over sites on Whillans Ice Stream (WIS), Kamb Ice Stream (KIS), and Bindschadler Ice Stream (BIS) 4700^{+1500}_{-2300}, 1800^{+2700}_{-700}, and ca. 1700^{+2800}_{-600} years ago respectively. The grounding line only recently re-advanced back over those sites 1100^{+200}_{-100}, 1500^{+500}_{-200}, 1000^{+200}_{-300}, and 800 ± 100 years ago for SLW, WIS, KIS, and BIS respectively. The timing of grounding line retreat coincided with a warm period in the mid- to late-Holocene. Conversely, grounding line re-advance is coincident with climate cooling in the last 1000-2000 years recorded in the WAIS Divide Core. Our estimates for the timing of grounding line retreat and re-advance are also consistent with relatively low carbon-to-nitrogen ratios measured in our subglacial sediment samples (suggesting a marine source of organic matter) and with the lack of grounding-zone wedges in front of modern grounding lines. Based on these results, we propose that the Siple Coast grounding line motions in the mid- to late-Holocene were driven by relatively modest changes in regional climate, rather than by ice sheet dynamics and glacioisostatic rebound, as hypothesized previously (Kingslake et al., 2018).

1 Introduction

Ice loss from the West Antarctic Ice Sheet (WAIS) is a significant uncertainty in projections of near-future sea-level rise (Bamber et al., 2019; Church et al., 2013). This uncertainty is partly due to limited observational constraints on the climate sensitivity of WAIS grounding lines, which mark the locations where ice thins and starts floating on seawater. The evolution of grounding line positions in West

Antarctica during and immediately following the Last Glacial Maximum (LGM) is well documented because the relevant geologic evidence is largely accessible to marine geophysical and geological investigations (Anderson et al., 2014). However, evidence of WAIS grounding lines during much of the Holocene is hidden underneath fringing ice shelves, or even beneath the ice sheet itself (e.g., Bradley et al., 2015; Kingslake et al., 2018; Smith et al., 2019; Venturelli et al., 2020). Early ideas about post-LGM grounding line retreat in WAIS were that the grounding lines retreated unidirectionally, and that the modern configuration is the smallest since the LGM (Ackert, 2008; Anderson et al., 2014; Bentley et al., 2014; Conway et al., 1999; Hall et al., 2013). However, recent studies have challenged this paradigm by suggesting that during the Holocene, at least some of WAIS grounding lines retreated behind their modern positions before re-advancing to their current location (Bradley et al., 2015; Kingslake et al., 2018; Matsuoka et al., 2015; Venturelli et al., 2020).

Understanding Holocene ice sheet behavior may aid current efforts to project near-future ice mass loss from WAIS, due to the similarity of Holocene climatic and glacioisostatic forcings to the modern and near-future conditions. Here we re-examine previously collected datasets and samples to estimate the timing of grounding line retreat from, and re-advance to, the modern configuration in the Ross Sea sector of WAIS. We show that the available evidence is consistent with a climatic forcing of these major grounding line movements, with the retreat occurring during warm periods of the Holocene (Cuffey et al., 2016), which are also characterized by a decrease in sea-ice cover in the Ross Sea (Hall et al., 2006). Re-

advance occurred in the last 2000 years, corresponding to cooling recorded in the WAIS Divide ice core and an increase in Ross Sea summertime sea ice (Cuffey et al., 2016; Hall et al., 2006). Ice sheet model results published in Kingslake et al. (2018) suggest that these changes in Holocene positions of WAIS grounding lines may have been associated with global sea-level variations of about 0.2-0.3 m at the time when temperature variations at the WAIS Divide ice core site amounted to just a few degrees (Cuffey et al., 2016; Cuffey, 2017). Previous research in Greenland has indicated that at least some of the Greenland Ice Sheet retreated behind its present margin during the mid-Holocene climatic optimum, which ice sheet simulations suggest contributed an equivalent of 0.1-0.3 m of global sea-level rise (Vasskog et al., 2015).

2 Methods

2.1 Modelling of Basal Temperature Gradients

Vertical temperature profiles through ice can reveal information about past climatic conditions and ice deformation. The work of Engelhardt (2004) highlighted the fact that a large fraction of vertical temperature profiles measured in the Siple Coast ice streams are difficult to explain with an assumption of climatic and ice dynamic steady state because observed temperature gradients in the lowermost 100 m are anomalously high. The high basal temperature gradients indicate that there is cold ice present at the base of the ice. There are three ways to get cold ice at the base of an ice sheet without changing the basal boundary conditions: cooling the surface

temperature, increasing the vertical advection of ice (accumulation), or increasing the horizontal advection (ice velocity). Engelhardt (2004) addresses these options and rules out increased accumulation or lowering of the surface temperature, ultimately settling on horizontal advection as the main explanation for the cold ice. However, even by proposing a "super-surge" event that drastically increases the horizontal advection, he was unable to reproduce the high basal temperature gradients without invoking basal melt (i.e. changing the basal boundary conditions).

Here, we conjecture that this unsteady thermal state is due entirely to changing basal boundary conditions from Holocene ice shelf re-grounding in the region (Kingslake et al., 2018; Venturelli et al., 2020). Thus, we modelled the evolution of basal temperature gradients to constrain the timing of ice shelf grounding consistent with observed high basal temperature gradients. Measurements and analysis of temperature profiles taken at our field sites have previously been published (Engelhardt, 2004; Engelhardt and Kamb, 1993; Kamb, 2001), but we re-analyzed them with the new assumption that this area was an ice shelf that grounded in the recent past. We focused on the sites that had very steep basal temperature gradients: Kamb Ice Stream (KIS), Bindschadler Ice Stream (BIS), and the Unicorn (UC) (Fig. 2.1) (Table 2.1). (N.B. In this paper we will distinguish between our field sites and the ice streams they are located on by using abbreviations to refer to the field sites, and full names to refer to the ice streams.) Building on modelling employed by Bindschadler et al. (1990) to date the formation of Crary Ice Rise as the Ross Ice Shelf grounded on a bathymetric high, we modelled temperature profiles of

an ice shelf before and after grounding. We then compared the resulting basal temperature gradients to observed basal temperature gradients (Engelhardt, 2004). Our MATLAB code solves a one-dimensional, forward Euler, vertical advection-diffusion equation with a one-year time step and 10 m vertical step chosen to satisfy the von Neumann stability condition. The accumulation rate is set to be equal to the sum of vertical advection and change in ice thickness. Thus, when ice thickness remains constant, vertical advection is equal to the accumulation.

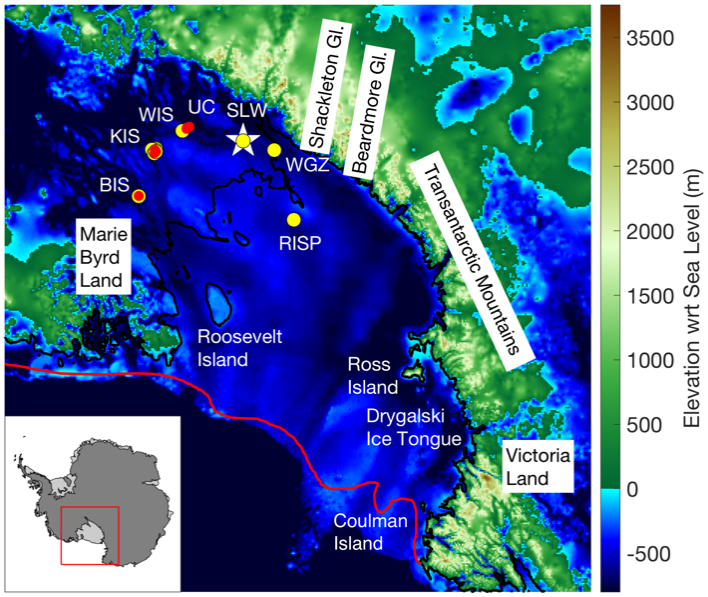

Figure 2.1: Location of sites and place names used in this study. Sites where measurements were taken and examined in this study are as follows: RISP (Ross Ice Shelf Project), WGZ (Whillans Grounding Zone), SLW (Whillans Subglacial Lake), UC (Unicorn), WIS (Whillans Ice Stream), KIS (Kamb Ice Stream), and BIS (Bindschadler Ice Stream). Background image uses bed elevation data (Fretwell et al., 2013). Yellow dots denote the location of sediment cores taken for radiocarbon and organic matter analyses. Red dots denote the location of deep ice-temperature profiles examined in this study. White star indicates the location where sediment porewater was collected and analyzed.

Table 2.1: Observed basal temperature gradients reported in (Engelhardt, 2004) and used in the temperature diffusion model.

Site	**Basal Temperature Gradient (K/km)**
BIS	-61.2
KIS	–54.6
KIS	–60.5
KIS	–63.4
KIS	–71.3
UC	–83.5
UC	–81.0
UC	–51.5

We ran the ice temperature model in two phases: floating ice shelf and grounded ice. First, we ran a diffusion advection model for the ice shelf phase with a constant surface temperature of -25 ºC based on surface temperature measurements along the Siple Coast (Engelhardt, 2004) and a bottom temperature equal to the freezing point of seawater at a salinity of 34 PSU and a pressure corresponding to ice thickness, calculated using Eq. (5) in Begeman et al. (2018). We assumed a constant surface accumulation rate of 0.15 m/yr based on observations at Siple Dome (Waddington et al., 2005). Additionally, we assumed the ice shelf to be in steady state, which requires a basal melt rate of 0.15 m/yr to compensate for accumulation, and ignored horizontal advection. We varied the starting ice shelf thickness from 500 m to 1000 m based on modern ice thickness near the Ross Ice Shelf grounding lines

(Fretwell et al., 2013; Still et al., 2019) and allowed the ice shelf temperature profile to come to steady state. Using this ice shelf steady-state temperature profile as the initial conditions for phase two of the simulations, we then modelled the ice temperature evolution after grounding. Keeping the surface boundary conditions constant, we changed the bottom temperature boundary condition to reflect the pressure melting point of ice. Although other similar models – including the Bindschadler et al. (1990) model – pick the basal boundary condition after grounding to be the geothermal flux, we chose the freezing point of freshwater because we assumed that basal freeze-on occurred at these locations after grounding, as evidenced by the widespread presence of basal ice layers found in boreholes drilled along the Siple Coast ice streams (Christoffersen et al., 2010; Kamb, 2001; Vogel et al., 2005) and at the grounding zone of the Whillans Ice Stream (unpublished data). Because basal melt rates of ice shelves near grounding lines are high – on the order of 10 cm/yr (Begeman et al., 2018) or even 20 m/yr in melt channels (Marsh et al., 2016) – we assume that any basal ice present prior to grounding line retreat melted away when our field sites became ungrounded, and that the basal ice found along the Siple Coast formed after re-grounding. In addition, we calculated the thickness of basal ice that forms during Phase 2 of the model. We allowed the model to run from 0 to 8000 years, and obtained the time-dependent temperature gradient for the bottom 100 m so we could compare our modelled results to observed basal temperature gradients (cf. Engelhardt, 2004). We chose 8000 years ago as the earliest the grounding line could have retreated over our field sites based on grounding line positions inferred from the

dating of sediments in the Transantarctic Mountains and the Ross Sea, which placed the grounding line several kilometers north of the Siple Coast ice streams 8000 years ago (Lee et al., 2017; McKay et al., 2016; Spector et al., 2017). Sensitivity tests and equations used for our ice temperature model are presented in the Supplemental Material.

2.2 Ionic Diffusion Modelling

To estimate the timing of retreat and re-advance of the grounding line at Whillans Subglacial Lake (SLW) (Fig. 2.1), where the observed basal temperature gradients are not anomalously steep (Fisher et al., 2015), we compared measured porewater ionic concentrations from a sediment core collected at SLW (Michaud et al., 2016a) to values modelled using an ionic diffusion model with a two-stage upper boundary condition. The first phase here assumes that the sedimentary column at SLW was exposed to seawater for some length of time during the Holocene (T_o). This was followed by ice-shelf re-grounding and exposure of the SLW sedimentary column to basal meltwater (T_i). Porewater chemistry data that we compare to the output of our forward model comes from sediment core MC-3B collected from SLW using a multicorer on January 30, 2013; methods used for sediment core and porewater collection are described in detail in Tulaczyk et al. (2014) and Michaud et al. (2016b).

We ran one-dimensional vertical diffusion simulations using the chemical parameters Cl^-, SO_4^{2-}, Na^+, Ca^{2+}, $\partial^{18}O$, and ∂D, through pore spaces of sediments

below SLW (e.g. Adkins and Schrag, 2003). The diffusion coefficients used for each chemical parameter examined in this study were calculated using the equation from Li and Gregory (1974) for diffusion of ions through sediments:

$$D_{sed} = D\frac{\alpha}{\theta^2} \quad (1)$$

Where D is the self-diffusion coefficient, α is the ratio of viscosity of the bulk solution to the average viscosity of the interstitial solution and θ is tortuosity. α is a constant with value close to one (Li and Gregory, 1974). In this study we assume it to be exactly one for simplicity. We used previously calculated self-diffusion coefficients determined for the chemical parameters at 0 ºC (Li and Gregory, 1974; Wang, 1951a, 1951b). To calculate tortuosity, we use an equation from Boudreau (1996):

$$\theta^2 = 1 - \ln(\varphi^2) \quad (2)$$

Where φ represents porosity, which is taken to be 0.4 here (Engelhardt et al., 1990; Tulaczyk et al., 2001). The final diffusion coefficients used for each chemical parameter are shown in Table (2.2).

Table 2.2: Diffusion coefficients and concentrations for chemical parameters examined in the porewater diffusion model. The seawater concentrations are the typical concentrations in standard 35 per-mil seawater, and the meltwater concentrations are from measurements taken in Whillans Subglacial Lake (Michaud et al., 2016a).

Chemical Parameter	**D_{sed} (m^2/yr)**	**Seawater Concentration *(g/kg) or **(‰)**	**Meltwater Concentration *(g/kg) or **(‰)**
Cl^-	0.0113	*19.353	*0.125
SO_4^{2-}	0.00557	*2.712	*0.053
Na^+	0.00699	*10.76	*0.121
Ca^{2+}	0.00416	*0.412	*0.017
$\partial^{18}O$ - (H_2O)	0.0162	**0	**-38
∂D - (H_2O)	0.0111	**0	**-300.9

We forced the diffusion model by switching the upper boundary conditions to reflect either marine or subglacial conditions (Table 2.2), which represent time periods when the grounding line had retreated beyond or advanced over SLW, respectively. For modelling purposes, we assumed the switch between sub-ice shelf and subglacial conditions and vice versa was instantaneous. However, we acknowledge that the transition is probably more nuanced and includes a stage of estuarine conditions where tidal pumping allows marine waters to enter the subglacial system upstream of the grounding line, as seen currently under the Whillans Ice Stream (Horgan et al., 2013a). The depth of the simulated diffusion profile was 100 m, vertical resolution was 0.5 m, and temporal resolution was 1 year. We started each simulation assuming that the initial porewater through the entire profile was in equilibrium with subglacial meltwater conditions, i.e. meltwater chemical properties

of Whillans Subglacial Lake (Table 2.2) throughout the domain thickness. This assumption is justified by the fact that the SLW site was beneath the ice sheet for at least 30,000 years (Clark et al., 2009) and must have been in a subglacial setting for almost all of the Quaternary period when WAIS was mostly larger than today (e.g., Scherer et al., 1998). We then instantaneously changed the upper boundary condition at time $t = 0$ to reflect seawater values (Table 2.2) to represent post-LGM grounding line retreat past SLW. In this first phase, characterized by simple initial and boundary conditions, the time- and depth-dependent changes in chemical concentration for each parameter can be expressed using the analytical solution (Turcotte and Schubert, 2014, Eq. 4.113):

$$\frac{C-C_o}{C_s-C_o} = erfc\left(\frac{y}{2*\sqrt{D_{sed}*t}}\right) \quad (3)$$

Where C is the ion or isotope concentration, subscripts o and s represent initial and surface respectively, y is the distance from the surface, and t is the total time. We then instantaneously changed the boundary conditions at time $t = T_o$ back to subglacial meltwater conditions to simulate ice shelf re-grounding. At $t = T_o$ we also switch to solving the problem using a finite-difference diffusion model, which is a modified version of the same MATLAB code used by us previously to calculate vertical heat advection-diffusion in the ice shelf. The initial condition for the second, numerical phase of the model is the profile obtained from our analytical solution (Eq. 3) at time $t = T_o$. The subglacial and oceanic tracer concentrations we assumed for

the six chemical parameters are given in Table (2.2). We ran the two-phase analytical-numerical diffusion model for each chemical parameter separately, varying the amount of time during which the upper boundary condition reflected marine conditions and subglacial conditions (T_o and T_i) from 1 to 8000 years.

To determine which profiles fit the measured concentrations in the core, we compared the gradient of the top 0.5 m of each model run to the measured concentration profiles (Michaud et al., 2016a). We performed a least squares regression on the measured concentrations and tracked which model profiles fit within 95% confidence bounds for the measured values.

We also considered the possibility that vertical advection was occurring as groundwater flow, but were able to discount it based on considerations of the Peclet number:

$$Pe = \frac{uH}{D_{sed}}, \tag{4}$$

where H is the length of the core and u is the velocity. In order for advection to be dominant (i.e. $Pe \geq 1$), u must be at least 0.011 m/yr. However, this is an order of magnitude greater than previous calculations of upward groundwater flux on the Whillans Ice Stream (Christoffersen et al., 2014).

2.3 Radiocarbon Measurements and Modelling

We revaluated the radiocarbon data from the Siple Coast of the WAIS presented in Kingslake et al. (2018) to estimate the timing of Holocene grounding line retreat and re-advance in this region. We focused on 11 subglacial till samples

collected between 1989 and 2013, and 23 sediment samples collected below the Ross Ice Shelf in 1978 and 2015. Site locations are shown in Fig. 2.1 and include: SLW, the Whillans Ice Stream (WIS), KIS, BIS, the Whillans Grounding Zone (WGZ), and the Ross Ice Shelf Project (RISP). Details of the core collection, storage, and radiocarbon analysis are described in Kingslake et al. (2018). Apparent carbon ages inferred from the fraction of modern radiocarbon (*Fm*) in the samples were presented in the extended data section of Kingslake et al. (2018). Kingslake et al. (2018) were careful to note that the apparent radiocarbon ages were not true ages due to the fact that the samples consisted of a mixture of young radiocarbon-bearing organic matter and re-worked radiocarbon-dead organic matter, which resulted in carbon ages that are much older than the actual age of the last exposure to radiocarbon inputs.

To better understand the sources of organic matter found in our sediment samples, we collected new data on carbon and nitrogen present in the samples: 17 samples collected from subglacial sites, 17 samples from sub-ice shelf sites, and 2 samples melted out from basal ice collected at a subglacial site. Total carbon (TC), total organic carbon (TOC), and total nitrogen (TN) measurements were performed at the University of California Santa Cruz Stable Isotope Laboratory. Samples (8-10 mg bulk sediment) for TOC and $\delta^{13}C$ determination were decarbonated via direct acidification with sulfurous acid. All samples were dried prior to weighing for measurement. TC and TN were measured simultaneously by Dumas combustion using a CE Instruments NC2500 elemental analyzer coupled to a ThermoFinnigan Delta Plus XP isotope ratio mass spectrometer. TOC and $\delta^{13}C$ were measured

independently on the same instrumentation. All measurements were calculated relative to an in-house gelatin standard, which was extensively calibrated against international standard reference materials. Typical reproducibility (1σ) of duplicate measurements is better than 0.1 wt%C, better than 0.01 wt%N, and better than 0.1 permil $\delta^{13}C$. Finally, total inorganic carbon (TIC) was calculated as the difference of TC and TOC. The TOC and C:N measurements for our field sites are shown in Fig. 2.2, and all results for TOC, TC, TIC, C:N, and $\delta^{13}C$ are presented in the Supplemental Material. We used the TOC measurements to constrain our radiocarbon model (see below) and used the $\delta^{13}C$ and C:N measurements to better understand the origin of the sediments. By examining where the measurements lie on a $\delta^{13}C$ vs. C:N plot (e.g., Fig. 2.3) we can glean information about the potential sources of the organic material in the sediments (Lamb et al., 2006).

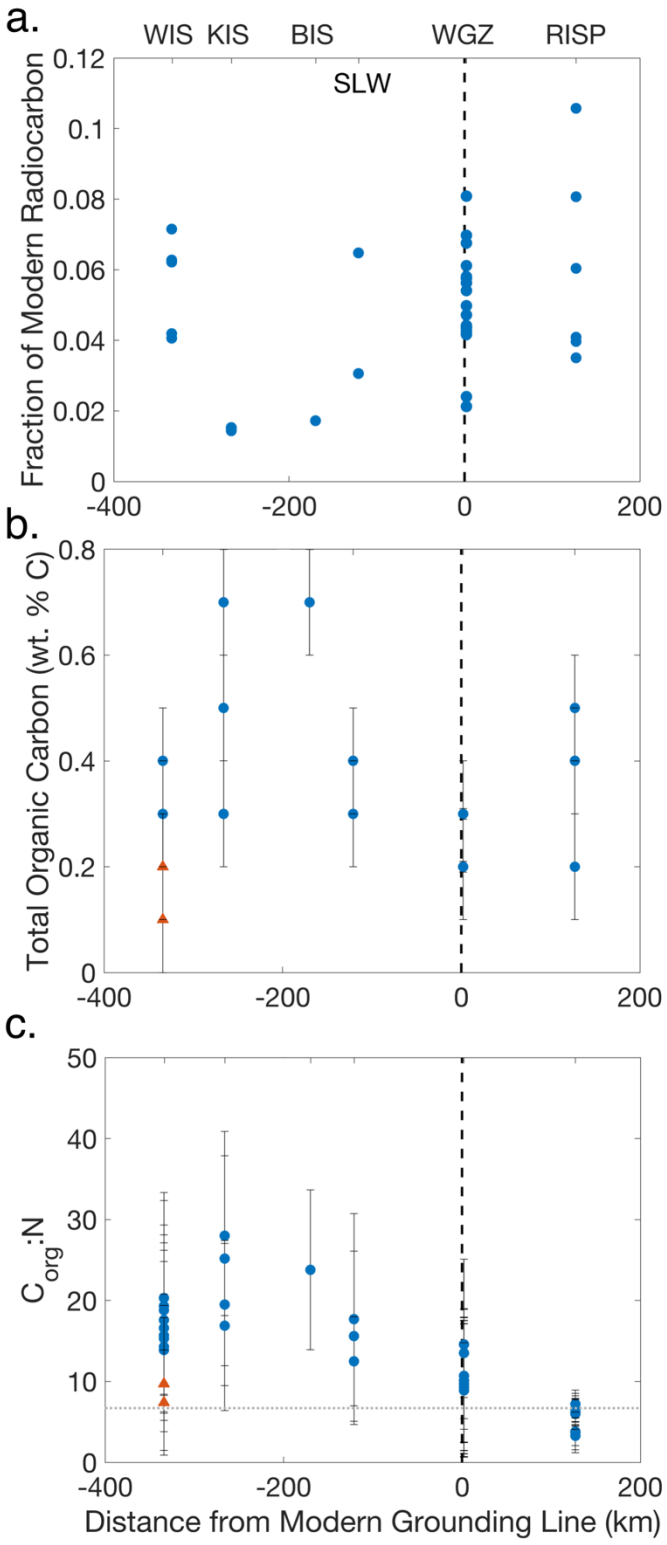
a.
WIS
KIS
BIS
WGZ
RISP
SLW
Fraction of Modern Radiocarbon
0.12
0.1
0.08
0.06
0.04
0.02
0
-400
-200
0
200
b.
Total Organic Carbon (wt. % C)
0.8
0.6
0.4
0.2
0
-400
-200
0
200
c.
C org :N
50
40
30
20
10
0
-400
-200
0
200
Distance from Modern Grounding Line (km)

Figure 2.2: Results of radiocarbon and organic matter analyses for sediment samples taken from beneath grounded ice (SLW, WIS, KIS, BIS), or beneath floating ice (RISP, WGZ), or entrained in basal ice (UC) plotted against sample position with respect to the modern grounding line. **(a)** Fraction of modern radiocarbon (*Fm*) measured in acid-insoluble organic matter from bulk sediments. Error bars are smaller than the symbols. **(b)** Total organic carbon (TOC). **(c)** C_{org}:N_{tot} (atom:atom). The dotted gray line represents the typical C:N of the ocean (Redfield, 1958). Orange triangles represent the values for sediments recovered from UC basal ice.

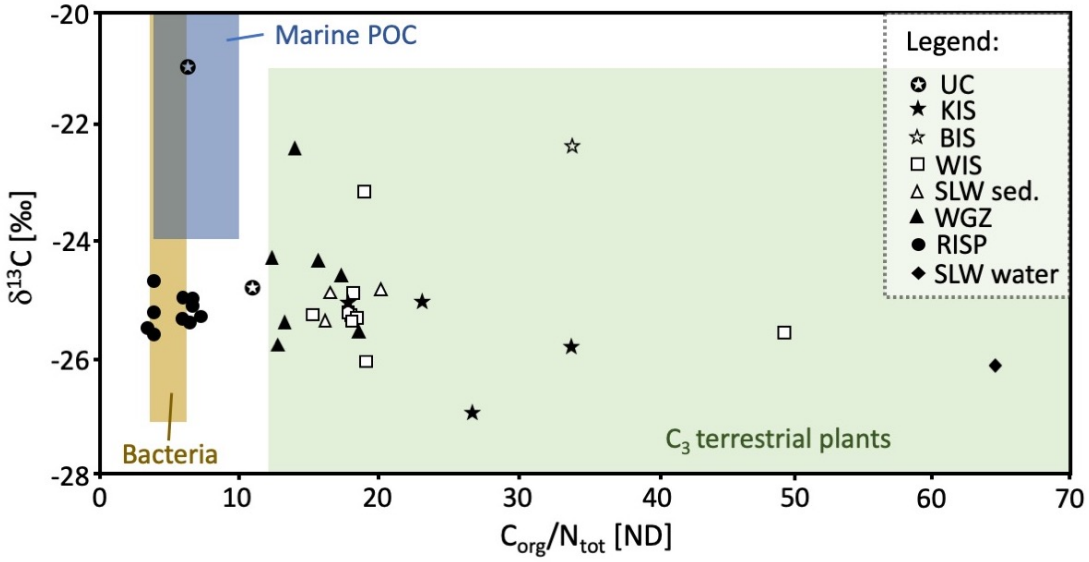

Figure 2.3: $\delta^{13}C$ plotted against C_{org}:N_{tot} (atom:atom). Shaded areas taken from Lamb et al. (2006). Although the RISP and WGZ samples are from a sub-ice shelf cavity, RISP is located mid-ice shelf whereas WGZ is located within the grounding zone. The UC samples are sediments melted out from basal ice, as opposed to collected below ice or an ocean cavity.

To estimate the timing of retreat and re-advance of the grounding line along the Whillans Ice Plain, we developed a two-phase model of ^{14}C and ^{12}C evolution at our field sites from 8000 years ago to the present (see Fig. 2.4 schematic). We again used 8000 years ago as the earliest possible time the grounding line could have retreated behind our field sites. The first model phase represented the time after grounding line retreat beyond the sediment sampling locations (Fig. 2.4). We

assumed that at the onset of post-LGM grounding line retreat in the Ross Sea Sector, sediments at our field sites contained no ^{14}C, but did contain organic matter with ^{12}C (Fig. 2.4). Given the short half-life of radiocarbon and the geologic evidence suggesting that the grounding line in the Ross Sea was at its LGM maximum position at roughly 30,000 years ago, we followed the conjecture of Kingslake et al. (2018) that ^{14}C found in the sediments was incorporated after the post-LGM grounding line retreat. This assumption that the ^{14}C originated from a marine environment was also employed by Venturelli et al. (2020) when they dated the grounding line retreat over WGZ. New, ^{14}C-bearing marine organic matter was thus introduced into radiocarbon-free sediments during this first model phase (Fig. 2.4). We assumed a constant rate of ^{14}C deposition, a, and a constant rate of ^{12}C deposition, A, for the entire first phase of the model, when sediments were assumed to be exposed to input of radiocarbon-bearing marine organic matter. The ratio of ^{14}C to ^{12}C at the time of deposition was taken to be equal to that measured in modern amphipods collected at the grounding zone of the Whillans Ice Stream (WGZ) in 2015 (Kingslake et al., 2018). Because these amphipods were part of the marine food chain beneath the Ross Ice Shelf, we assumed that their *Fm* is representative of the *Fm* of the ocean water in the grounding line environment. The *Fm* for the amphipods corresponds to a radiocarbon reservoir age of ca. 1000 years for the sub-ice shelf marine organic matter. We represented the evolution of ^{14}C concentration, n, during this phase by accounting for both the addition and decay of ^{14}C, with the equation:

$$n(t) = a\tau\left(1 - e^{\frac{-t}{\tau}}\right) \quad (5)$$

Where t is time and τ is the mean lifetime of ^{14}C (8033 years, based off the Libby half-life of ^{14}C [Stuiver and Polach, 1977]). We represented the time-dependent concentration of ^{12}C (N) during the first model phase using the equation:

$$N(t) = N_o + At \quad (6)$$

Where N_o is the amount of ^{12}C present initially in the system. We ran the first phase of the model from $t = 0$ to $t = T_o$, where T_o is the length of time a given field site is exposed to the ocean. The second model phase represents the time after the ice sheet again covered a given site, and the only process affecting ^{14}C concentration is radioactive decay (Fig. 2.4). We represented the ^{14}C concentration with the equation:

$$n(t) = n^* e^{\frac{-t}{\tau}} \quad (7)$$

Where n^* is the value of n when the system switches from sub-ice shelf to subglacial. After a site is glaciated, inputs of marine organic matter cease, and thus we took ^{12}C to be constant with time at the value it had at the moment of grounding (N^*):

$$N(t) = N^* \quad (8)$$

Detailed derivation of these equations is shown in the Supplemental Material.

We normalized the calculated TOC values to a 100 g sample of dry sediments. We added *n(t)* and *N(t)* and divided by 100 g of sediment. To calculate *Fm*, we divided *n(t)* by *N(t)*, and divided the quotient by the modern ratio of ^{14}C to ^{12}C (1.176×10^{-12}).

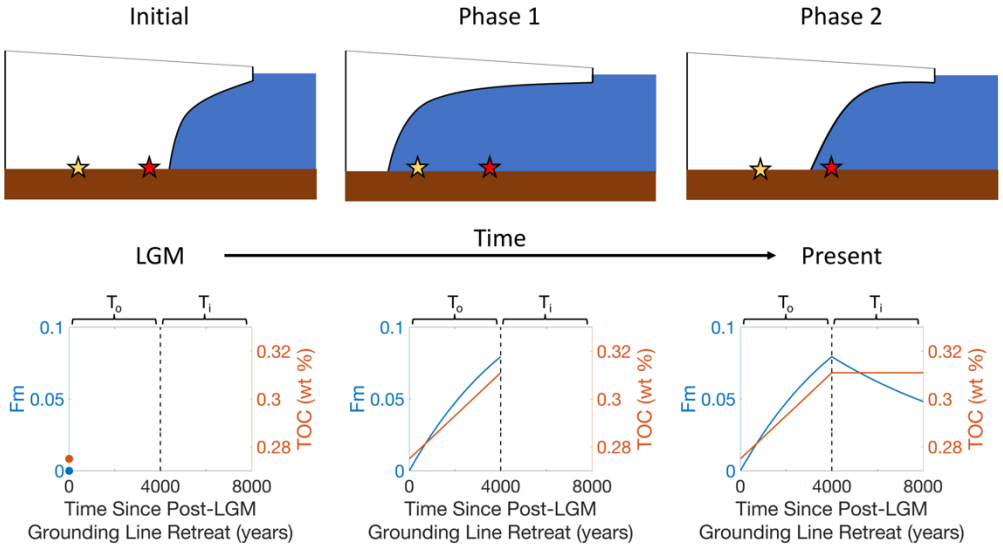

Figure 2.4: Schematic of the two-phase model of radiocarbon evolution since onset of LGM grounding line retreat over the field sites. The yellow star represents subglacial field sites, whereas the red star represents sub-ice shelf sites. The evolutions of *Fm* and TOC are shown for subglacial field sites. For this run, both T_o and T_i equal 5000 years; the horizontal axis represents time since post-LGM grounding line retreat past a subglacial site (yellow star). Ocean exposure (when the grounding line had retreated beyond a site) begins at $t = 0$ and is assumed here to last until $t = 5000$ years. Subsequent grounding line re-advance occurs at $t = 5000$ years and lasts until the end of the model run ($t = 10{,}000$ years). Accumulation rates for ^{14}C and ^{12}C were assumed to be 9.23×10^{-18} g/yr and 9.0×10^{-6} g/yr per 100 grams of dry sediments, respectively. Note that the right-hand side axis (TOC) does not start at zero.

Organic carbon input to the sediments likely comes predominantly from local fecal pellets and necromass of macro, micro, and meiofauna, with a potential additional syndepositional regional input by sub-ice shelf water column advection (Kingslake et al., 2018; Turner, 2015). During borehole drilling at WGZ, where the water column was only 10 m thick, higher than expected concentration of living biomass were observed in the form of planktic and nektonic organisms, including amphipods, fish, and jellies (whereas no multicellular life was noted at SLW). The

only potential evidence noted of benthic organisms at WGZ was rare organic sheaths, presumably from infaunal meiofauna at the sediment-water interface. The absence of a developed benthic community is likely due to high sediment rainout from melt of debris-laden basal ice, as observed by borehole cameras. Low concentrations of infauna were noted in the upper 10 cm at RISP (Harwood et al., 1989; Kellogg and Kellogg, 1981), ca. 100 km from WGZ, which is reflected in the relatively higher *Fm* measured in those samples. Although it is difficult to discern a sediment flux rate at WGZ from these observations, we were able to determine the accumulation of carbon in the sub-ice shelf ocean cavity by running the model for both RISP and WGZ, where we could ignore the re-advance of the grounding line (phase two of the model). Here, we expect them to be similar to the sub-ice shelf conditions experienced by our field sites following grounding line retreat, i.e., in the first phase of the model. We thus ran phase one of the model for RISP and WGZ for t equaling 8000 ± 1000 years. Because previous studies have placed the grounding line at Ross Island ca. 8000 years ago (Baroni and Hall, 2004; Licht et al., 1996; McKay et al., 2016), we set 8000 years ago as the most likely timing of grounding line retreat over RISP and WGZ. We also examine the preceding and following 1000 years to account for uncertainty in that timing. For each model run we varied the value of A in increments of 10^{-7} from 10^{-7} to $2x10^{-5}$ and varied the value of N_o in increments of 0.0025 from 0 to 0.6. To test which values of A and N_o fit observations, we compared the *Fm* and TOC resulting from our calculations of ^{14}C and ^{12}C to measured values at WGZ and RISP and noted which values of A and N_o produced *Fm* and TOC values that fell within the maximum

and minimum observed values. Values of A that fit the data ranged from 3 x 10^{-7} to 1.61 x 10^{-5} g/yr per 100 grams of dry sediment. The upper range of these values is comparable to the accumulation rate of organic carbon in modern Ross Sea sediments, of the order of 10^{-5} g/yr per 100 grams of dry sediments (recalculated from data in Demaster et al. [1992] and Frignani et al. [1998]).

With parameter ranges for a and A constrained using sample radiocarbon data from RISP, WGZ, and modern amphipods, we then ran the model for all subglacial cores for which radiocarbon has been measured. We varied A over the range determined from RISP and WGZ, varied N_o from 0.08 g to 0.5675 g (normalized to a 100 g sample of dry sediment), and varied the length of exposure to sub-ice shelf conditions as well as the time period of subsequent subglacial conditions from 0 to 8000 years each. As with the model runs for RISP and WGZ, we checked whether each model run was compatible with our measurements by comparing the calculated *Fm* to the measured *Fm*. Although the samples were collected at the same field sites in the same years, *Fm* and TOC could not be measured from the same sample; therefore, we tested whether modelled TOC fell within the maximum and minimum measurements of TOC for a given sampling location. Because we only had one measurement of TOC from BIS, we combined TOC measurements from BIS and KIS, and used maximum and minimum values of TOC as the bounds on TOC for both BIS and KIS. In our judgement, this approach is justified because values of *Fm* for both KIS and BIS are similar (Fig. 2.2a).

3 Results

3.1 Ice Temperature Analysis

We used thermal modelling in ice to constrain the time since grounding line re-advance (T_i) over the sites with steep observed basal temperature gradients (Fig. 2.5). We ran the model for $0 \leq T_i \leq 8000$ years, but because all basal temperature gradients ≥ 50 ºC/km – the definition of cold-based ice used in Engelhardt (2004) – occur when $T_i < 4000$ years, we only examine the model runs where $0 \leq T_i \leq 5000$ years. For each site, we compared the modelled basal temperature gradients to the observations and noted which model results fell within 10% of the observed basal temperature gradients. These comparisons suggest that the grounding line advanced over KIS between 2700 and 300 years ago, over BIS between 1400 and 700 years ago, and over UC between 3600 and 100 years ago. Combining the results for timing of grounding line re-advance (T_i) for all ice thicknesses allows for evaluation of the frequency at which the model predicted a certain value of T_i. Using the median as the optimal timing of grounding line re-advance (T_i) and the 32nd and 68th percentiles as the bounds on the error, the temperature model thus suggests that the grounding line likely re-advanced over KIS 1000^{+200}_{-300} years ago, over BIS 800 ± 100 years ago, and over UC 1500^{+500}_{-200} years ago (Fig. 2.5). UC has the largest spread of possible values of T_i, due to one observed basal temperature gradient differing noticeably from the other two. This may be a result of that location being separated from the others by a paleo-shear margin (named Fishhook) (Clarke et al., 2000). We account for vertical advection, but not horizontal advection in the temperature model. Because the

Bindschadler Ice Stream is not currently stagnant and the Kamb Ice Stream has only been stagnant for the past ca. 150 years (Retzlaff and Bentley, 1993), temperature modelling cannot be used to determine a precise time since grounding, but rather it provides a more general idea of how long ago grounding occurred. Importantly, the only model runs that produced basal temperature gradients comparable to those measured at KIS, BIS, and UC were those that assumed ice grounding within the last 4000 years. The temperature modelling through ice also allows us to estimate basal ice thickness growth after grounding. The maximum thickness of basal ice for the three locations examined was 15.8 m for KIS, 10.2 m for BIS, and 19.3 m for UC. These thicknesses only account for the accretion of pure ice, and do not include the contribution of any incorporated debris to the total thickness of debris-laden ice. Given the simplicity of our model, these values are reasonably close to the thickness of debris-laden basal ice (ca. 10-20 m) observed in boreholes in this region (e.g., Christoffersen et al., 2010; Vogel et al., 2005).

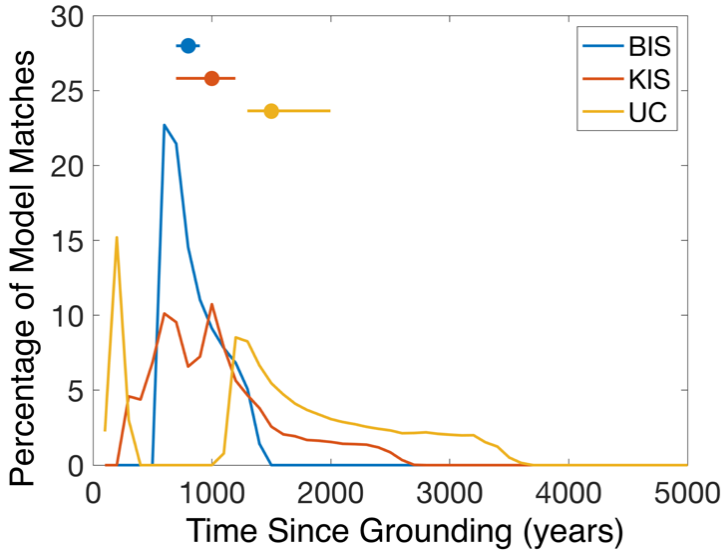

Figure 2.5: Results of temperature diffusion modelling. The y-axis represents the frequency at which the modelled basal temperature gradients fit within 10% of the observed basal temperature gradients (Engelhardt, 2004). The number of observed basal temperature gradients varied between the sites: one observation for BIS, four observations for KIS, and three observations for UC. The dots and lines in the upper portion of the figure correspond to the median and the 32nd to 68th percentiles of the distributions shown in the lower portion of the figure. The total number of model runs performed was 808,000, corresponding to a time window of 8000 years ago to present.

3.2 Ionic Diffusion Modelling

Ionic diffusion modelling of SLW allowed us to constrain T_i better than T_o. For each chemical parameter examined, the modelled diffusion profiles that fit the measured concentration profiles were in agreement with regards to exposure time to ocean (T_o) and subglacial (T_i) conditions (Fig. 2.6). We were able to fit diffusion profiles for every value of T_o tested, which impeded our ability to eliminate some lengths of T_o and therefore identify the length of time SLW was exposed to the ocean. Conversely, we were successful in constraining the time since grounding line re-

advance (T_i) as the majority of the diffusion profiles that fit the measured porewater concentrations fall within the past 2000 years.

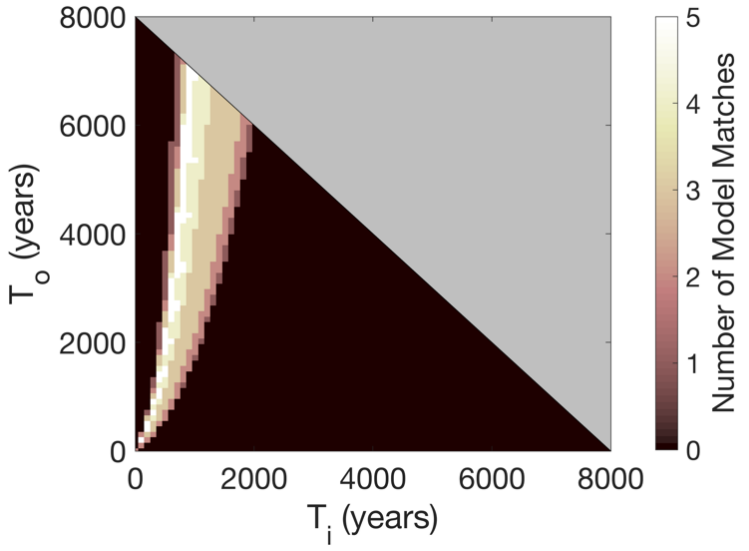

Figure 2.6: Stacked results from ionic diffusion modelling of all six chemical parameters. T_o represents the length of time over which the topmost sediment was exposed to ocean water after initial grounding line retreat and before grounding line re-advance. T_i represents the length of time over which the topmost sediment was exposed to subglacial conditions between the grounding line re-advance over SLW and now. The number of model runs included in this figure is 19,926.

3.3 Radiocarbon Modelling

The *Fm* values reported in Kingslake et al. (2018) and used in this study spanned from 0.0143 ± 0.0004 to 0.1058 ± 0.0013 (Fig. 2.2a). Ocean cavity samples recovered from RISP and WGZ showed greater spread in values of *Fm* than those recovered from sites below grounded ice. Samples with *Fm* values closest to the modern reference $^{14}C/^{12}C$ ratio (i.e. closest to *Fm* = 1) were recovered from the sub-ice shelf cavity of the Ross Ice Shelf (RISP and WGZ), and samples furthest from the modern reference $^{14}C/^{12}C$ ratio were recovered from below the Kamb and

Bindschadler Ice Streams. Even the samples taken from the ocean cavity (i.e. WGZ and RISP) contain only 10% or less of radiocarbon compared to the modern standard. The carbon-to-nitrogen ratio (C:N) of the organic matter from the RISP samples is also the closest to the typical 6.7:1 ratio measured in the ocean (Redfield, 1958) (Fig. 2.2c; Fig. 2.3), suggesting a significant input of marine organic matter consistent with the exposure of this site to the seawater below the Ross Ice Shelf during the Holocene. The subglacial sediment samples have higher C:N ratios, from 15.4 – 49.4 (Table S1) (Fig. 2.2c), which is consistent with their organic matter being a mixture of marine organic inputs and a pre-glacial, recalcitrant radiocarbon-dead component which originated from terrestrial C3 plants (Fig. 2.3). The grounding zone deposits sampled at WGZ cluster between the subglacial and RISP samples in terms of their C:N ratios (Fig. 2.3). Excluding the C:N values from UC, Fig. 2.2c indicates that the C:N ratios increase with distance from the modern grounding line. The two UC sediment samples are considered outliers because they came from debris-laden ice (Vogel, 2004, p. 61) rather than from subglacial till. Hence, they retained low, marine-like, C:N ratios because the process of basal freeze-on incorporated sub-ice shelf sediments right after ice shelf re-grounding.

The *Fm* values for samples collected from sites currently in the ocean cavity differ only slightly from those currently located below grounded ice. For instance, the mean *Fm* of the seven SLW and WIS samples is 0.050 ± 0.006 (standard error of the mean), while the corresponding mean and standard error for the six RISP samples is 0.060 ± 0.011. If the RISP samples were covered by ice today, it would take only

~1500 years for their average *Fm* to drop to the level of the SLW/WIS samples through radioactive decay alone. The difference in *Fm* among all subglacial (SLW, WIS, KIS, and BIS) and sub-ice shelf samples (WGZ, RISP) is statistically insignificant based on the linear mixed-effects model (p-value of 0.141, intraclass correlation coefficient of 0.565). The two groups only become statistically distinguishable from each other if we allow radioactive decay to occur in the samples below grounded ice for a period of at least an additional 1200 years. *Fm* values at KIS and BIS are similar to each other but differ from those at WIS and SLW (Fig. 2.2a), which are also similar to each other. The linear mixed-effects model indicates that KIS/BIS values are statistically distinguishable from the WIS/SLW *Fm* values (p-value of 2.11×10^{-5}). Overall, the sample-to-sample variations in *Fm* are relatively large compared to any variability due to differences in geographic settings of this sample population.

We used radiocarbon modelling to estimate the duration of ocean exposure following grounding line retreat (T_o) and the time since ice shelf re-grounding (T_i) (Fig. 2.7). Unfortunately, the radiocarbon modelling results are not very sensitive to T_i because the main process changing the simulated *Fm* of sediments after grounding is radiocarbon decay. That decay has a half-life of ca. 5000 years, or about half of the entire duration of the Holocene and much longer than values estimated for T_i through temperature or ionic diffusion modelling (0-2000 years for SLW, 100-3600 years for UC, 300-2700 years for KIS, and 500-1400 years for BIS). Thus, we use the results from temperature and ionic diffusion modelling to constrain T_i.

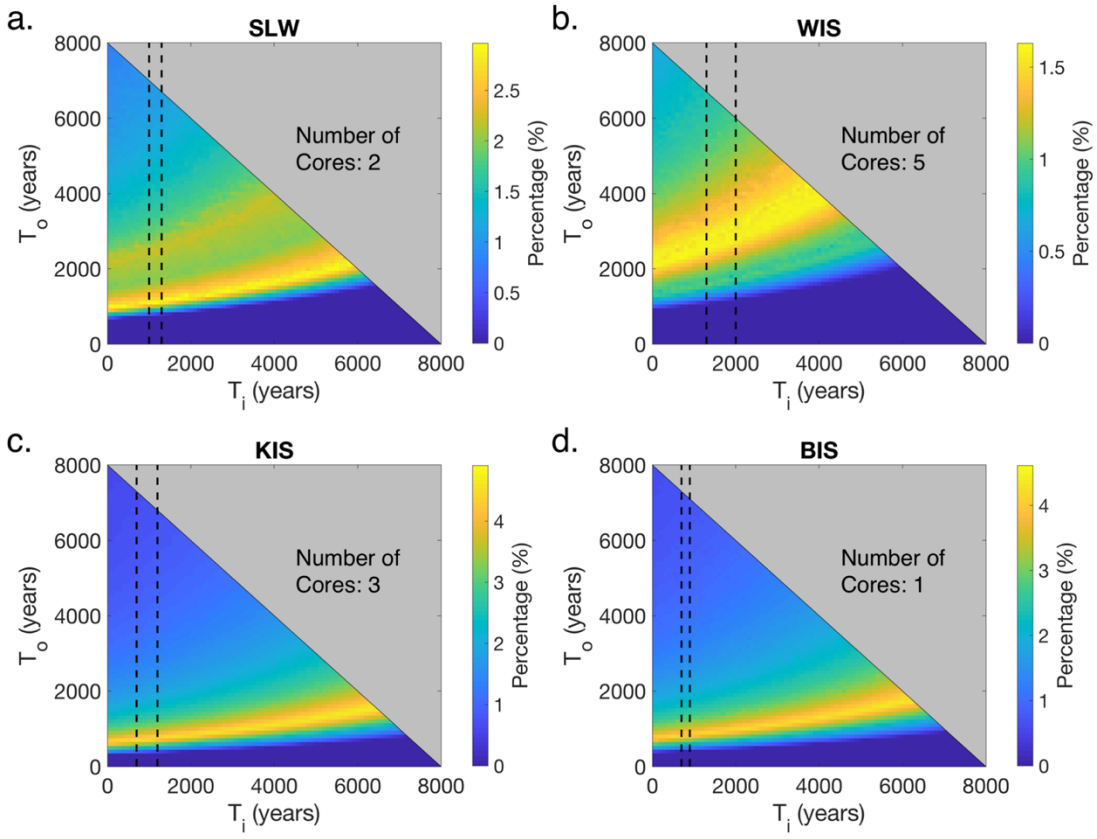

Figure 2.7: Results of radiocarbon modelling for all eleven subglacial cores. The axes correspond to the length of time the grounding line position had either retreated behind the sites (T_o) or advanced over them (T_i). The colorbar indicates the percentage of model runs which produced *Fm* and TOC that fell within the observed ranges for each core. A total of 103,495,644 model runs were performed for each core. Results from cores at the same field site are stacked on top of each other. Thus, the total number of model runs for each site is 206,991,288 for SLW, 517,478,220 for WIS, 310,486,932 for KIS, and 103,495,644 for BIS. **(a)** SLW **(b)** WIS **(c)** KIS **(d)** BIS. **a-d** indicate that the model provides better constraint to T_o than T_i. For example, **(c)** shows that at KIS, the model prefers ocean exposure durations (T_o) of 600-1800 years but does not constrain the duration of grounding line re-advance (T_i). The dashed lines indicate the 32nd and 68th percentiles from the results of the duration of T_i as determined by ionic and temperature diffusion modelling.

Additionally, we used the 32nd to 68th percentiles of the results from the temperature and ionic diffusion model results to further constrain the results of T_o found through radiocarbon modelling by only considering radiocarbon model

matches where T_i falls within the range determined for each respective area. We then calculated the time of grounding line retreat by adding together T_o and T_i for each radiocarbon model run that produced a model match (Fig. 2.8). For WIS, where we could not perform ionic or temperature modelling to constrain T_i, we used results from the temperature modelling at UC, which is located only a few kilometers away, but across the current shear margin of Whillans Ice Stream. We combine the T_i-constrained radiocarbon model results from every core at each site to estimate the peak of radiocarbon model matches for the timing of grounding line retreat at that site. The peak of radiocarbon model matches for timing of grounding line retreat over KIS and BIS were similar: 1800^{+2700}_{-700} years ago for KIS and 1700^{+2800}_{-600} years ago for BIS (Fig. 2.8; Fig. 2.9). The radiocarbon model matches for timing of grounding line retreat over SLW and WIS were slightly more distributed, with peaks occurring at 4300^{+1500}_{-2500} and 4700^{+1500}_{-2300} years ago, respectively (Fig. 2.8; Fig. 2.9).

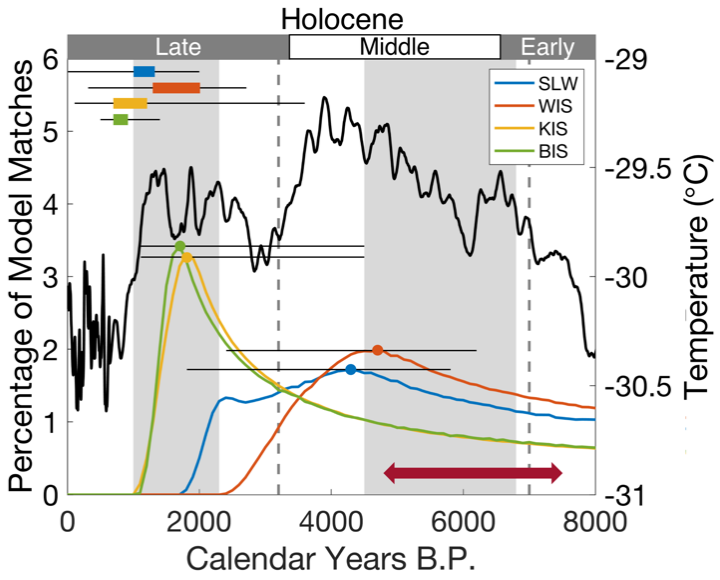

Figure 2.8: The estimated timing of grounding line retreat and re-advance compared to selected climate data for the study region. The colored lines (which correspond to the left y-axis) represent the probability distribution of the timing of grounding line retreat ($T_o + T_i$) for each subglacial field site. The lines are calculated by summing T_o and T_i from the model matches in between the dashed lines of the radiocarbon model results shown in Fig. 2.7. The dots on the peaks of the distributions indicate the optimal timing of grounding line retreat, and the thin black lines indicate the estimate on error. The box and whisker plots in the upper left corner indicate the timing of grounding line re-advance over our field sites (T_i) estimated from temperature and ionic diffusion modelling. The thick black line (which corresponds to the right y-axis) represents the Holocene history of surface temperature at WAIS Divide (Cuffey et al., 2016; Cuffey, 2017). The gray vertical shaded regions indicate the warm periods of less extensive sea ice in the Western Ross Sea proposed by Hall et al. (2006), and the gray dashed lines bracket the period of Ross Sea warming identified by Cunningham et al. (1999). The maroon arrow indicates the estimated range of grounding line retreat over WGZ based on the ramped-pyrolysis method (Venturelli et al., 2020).

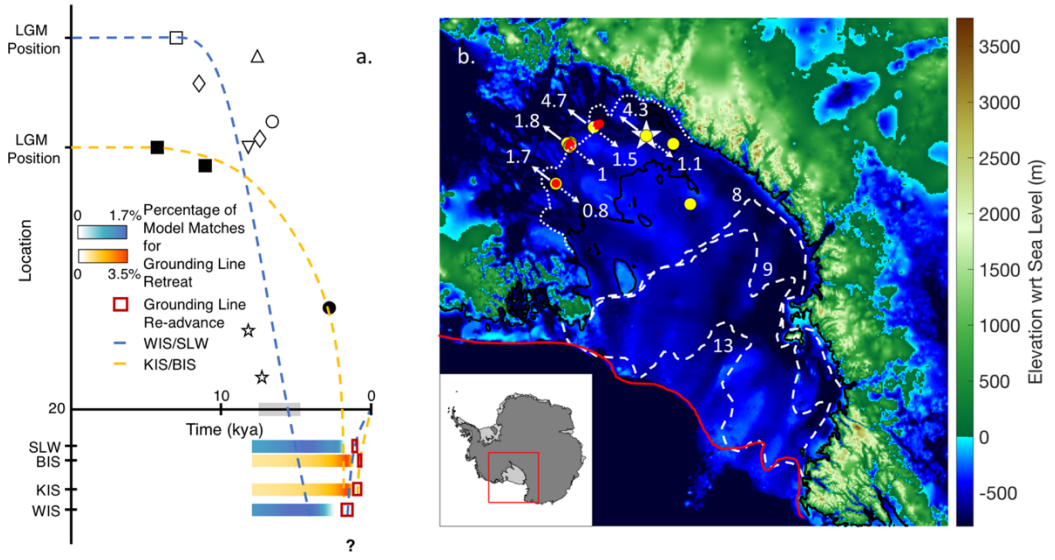

Figure 2.9: The evolution of grounding line positions in the Ross Embayment for the past 20,000 years. **(a)** Schematic for grounding line position along the flow lines of the Whillans Ice Stream (blue dashed line) as well as the Bindschadler Ice Stream and Kamb Ice Stream (yellow dashed line). Shaded bars represent the probability density plots for timing of grounding line retreat seen in Fig. 2.8. Symbols represent age constraints on grounding line position from the following studies: Baroni and Hall (2004) (right side up empty triangle), Bart et al. (2018) (solid square), Conway et al. (1999) (solid circle), Cunningham et al. (1999) (empty square), Jones et al. (2015) (empty circle), Licht et al. (1996) (empty diamond), McKay et al. (2016) (upside down empty triangle), Spector et al. (2017) (empty star). Open symbols represent ages along/near the flowline of the Whillans Ice Stream, and solid symbols represent ages along the flowline of the Bindschadler Ice Stream. Gray bar along the grounding line represents grounding line retreat at WGZ calculated in Venturelli et al. (2020). **(b)** Map-view of Holocene grounding line positions in the Ross Embayment. Background image is bed elevation (Fretwell et al., 2013). Yellow dots denote the location of sediment cores taken for radiocarbon and TOC analysis. Red dots denote the location of deep temperature profiles examined in this study. Cyan diamond indicates the location where sediment porewater was collected and analyzed. Red line indicates LGM grounding line position (Bentley et al., 2014). Dashed white lines indicate grounding line retreat from Lee et al. (2017). The corresponding numbers indicate timing in kya (thousands of years). Dotted white line shows most retreated grounding line position modelled in Kingslake et al. (2018). Solid white arrows indicate timing of grounding line retreat in kya, and dotted white arrows indicate timing of grounding line re-advance over those sites.

Radiocarbon modelling of the two cores from SLW produced slightly different results (Fig. 2.7a). These differences may be attributed to the difference in coring methods employed and by the apparent heterogeneity in sediment *Fm*. The

first core (SLW-PEC-1-34-35cm) was collected using a percussion corer, whereas the second (SLW-1 MC1B 0-8 bulk) was collected using a multicorer. The multicorer was designed to preserve and collect the surface sediments, whereas the percussion corer (which was acting as a gravity corer due to data communication issues) probably entered the sediment with backpressure in the barrel, thus blowing away soft surface sediments. Due to inefficient vertical mixing of sediments and the lack of evidence for erosion or deposition at this site (Hodson et al., 2016), we expect that these surface sediments were deposited when SLW was in a marine environment. Thus, the differences in *Fm* may result from the surface sediments being present in one core, but not the other.

4 Discussion

4.1 Post-LGM Grounding Line Position

To cast our results in a regional context, we created a schematic diagram of grounding line positions in the Ross Embayment for the past 20,000 years (Fig. 2.9a). The grounding line along the flow line of the Bindschadler Ice Stream began retreating before 14,700 years ago and remained on the outer continental shelf until at least 11,500 years ago (Bart et al., 2018). The grounding line was then located at Roosevelt Island 3,200 years ago (Conway et al., 1999) before retreating beyond KIS and BIS 1800^{+2700}_{-700} and 1700^{+2800}_{-600} years ago respectively; it then re-advanced over KIS 1000^{+200}_{-300} years ago and over BIS 800 ± 100 years ago. The grounding line along the Transantarctic Mountain side of the Ross Embayment began retreating from

its LGM position south of Coulman Island ca. 13,000 years ago (Anderson et al., 2014). This retreat was on average fairly rapid, as evidenced by the fact that the grounding line reached WIS 4700^{+1500}_{-2300} years ago. Our estimates for grounding line retreat along the flowline of the Whillans Ice Stream are in agreement with the estimates of grounding line retreat over WGZ (Venturelli et al., 2020). Venturelli et al. (2020) estimate that the grounding line retreated over WGZ 7500 – 4800 years B.P, which is only slightly earlier than our estimates of grounding line retreat over SLW (4300^{+1500}_{-2500} years ago) and WIS (4700^{+1500}_{-2300} years ago). This timing is consistent with the fact that SLW and WIS are roughly 100 and 300 km upstream of WGZ. The schematic for grounding line position along the Whillans Ice Stream flow line does not agree with all age constraints found in the Transantarctic Mountain Region (Fig. 2.9a). This could be because glaciers in the Transantarctic Mountains (for which the exposure ages were measured; Spector et al. [2017]) have a delayed response to grounding line retreat in the Ross Embayment, or because the grounding line retreated faster in the central Ross Embayment than along the sides. Grounding line re-advance also occurred relatively swiftly. Timing of this re-advance (1500^{+500}_{-200} years ago for WIS and 1100^{+200}_{-100} years ago for SLW) is coincident with the grounding of Crary Ice Rise 1100 years ago (Bindschadler et al., 1990). Although Crary Ice Rise is significantly seaward of SLW, it is situated on a pronounced bathymetric high. Therefore, it is plausible that by grounding first, it provided backstress (Still et al., 2019), allowing ice thickening and slow-down to aid the process of grounding line re-advance for the Whillans Ice Stream (Fried et al., 2014).

4.2 Ancillary Evidence Supporting Recent Grounding Line Re-advance

Our analysis of ice temperature and porewater chemistry suggest that the modern configuration of grounding line positions in the study region has been attained relatively recently. This inference is consistent with the conspicuous absence of grounding zone wedges (GZWs) revealed by detailed seismic surveys at the mouth of the Kamb and Whillans Ice Streams (Horgan et al., 2013b, 2017). These asymmetric sedimentary ridges can form quite rapidly during grounding zone stillstands (Simkins et al., 2018). For instance, the height of the massive Whales Deep GZW in the eastern Ross Sea grew by about 0.1 m per year in the last ca. 1000 years of its formation after growing nearly an order of magnitude slower over the prior ca. 2000 years (Bart and Tulaczyk, 2020). Assuming this range of GZW growth rates of 0.01-0.1 m/yr, in one millennium of GZW stillstand, GZWs can achieve heights of 10-100m. GZWs of such height would be detectable with the active-source seismic methods employed by Horgan et al. (2013, 2017). Hence, the lack of seismic evidence for GZWs at the grounding zones of Kamb and Whillans Ice Streams corroborates the inference that the modern grounding line positions of these ice streams have not been attained until very recently.

The idea that the lower part of the Whillans Ice Stream grounded only recently is also consistent with attributes of the microbial ecosystem discovered in Whillans Subglacial Lake (Christner et al., 2014). Ammonium is the predominant dissolved inorganic nitrogen compound in the lake water column, which also hosts a

high abundance of nitrifying microorganisms that obtain energy for chemosynthetic growth through oxidation of ammonia and nitrite (Christner et al., 2014). The source of ammonium for this community is diffusional flux from underlying sediment, facilitated by the activity of heterotrophic organisms which release ammonium via organic matter decomposition. While the abundant functional groups in the sediments shift to types associated with sulfur oxidation (Purcell et al., 2014) and methane oxidation (Michaud et al., 2016a) with depth, a diversity of heterotrophs exist in both the water and throughout the sediments sampled (Achberger et al., 2016). Similar phylotypes were also detected in sediments from KIS (Lanoil et al., 2009). Glacial meltwater contains no significant quantities of ammonia, and glacial erosion and grinding of minerals is not a significant source of nitrogen compounds (Tranter, 2014). Thus, a nitrifying microbial ecosystem in a subglacial lake, particularly one that is known to experience flushing of dissolved solutes (including nitrogen) from its lake waters every several years (Tulaczyk et al., 2014; Vick-Majors et al., 2020), requires a significant source of bioavailable nitrogen. A recent advance of the ice sheet over sub-ice-shelf sediments like the ones sampled at RISP offers an attractive explanation for the subglacial source of nitrogen fueling the microbial ecosystem found in Whillans Subglacial Lake (e.g., Fig. 2.3). It is well established that decomposition in organic-poor marine sediments can yield extremely low C:N ratios due to retention of ammonia on clay particles accompanied by the escape of carbon dioxide formed during oxidation of organic carbon stored in sediments (e.g., Müller, 1977). Recent analyses of fluorophore components identified in fluorescent

fractions of dissolved organic matter in SLW sediments, while not conclusive, support this notion, indicating characteristics of humic mixtures for coastal environments and marine sediments as well as Antarctic mountain glaciers and lakes (Vick-Majors et al., 2020). The ammonium-dominated, nitrifying microbial ecosystem of Whillans Subglacial Lake may, thus, be living off the legacy of marine organic matter stored in subglacial sediments for a relatively short period of time since the grounding line re-advanced over this region.

The mechanism described above also provides an explanation for the seemingly puzzling fact that the sub-ice shelf (RISP) sediment samples, which are exposed to seawater even now, have low C:N ratios, characteristic of marine sediments from a variety of locations (Müller, 1977), but have a very low *Fm* (0.06 on average). The RISP signature may be caused by the fact that much of the carbon, including radiocarbon, associated with young, recently produced organic matter, was part of labile organic molecules and hence, was preferentially digested during decomposition and released as carbon dioxide. This process, coupled with the fact that ammonia and ammonium are produced commonly in marine sediments through decomposition of marine organic matter rained out from the photic zone, can lower the C:N ratio of the sediments while removing some fraction of radiocarbon and leaving behind radiocarbon associated with more recalcitrant organic compounds which are radiocarbon-dead. The position of most subglacial sediment samples on the $\delta^{13}C$ – C:N plot (Fig. 2.3) is consistent with the bulk of their organic matter originating from pre-glacial terrestrial C3 plants rich in recalcitrant components such

as cellulose, lignin, or sporopollenin. The marine input which is responsible for the presence of radiocarbon (Kingslake et al., 2018; Venturelli et al., 2020) only makes up a small proportion of the total organic matter, and thus does not cause the subglacial sediments to display a marine signature in Fig. 2.3.

This interpretation is further corroborated by the fact that the two sediment samples from UC, which were melted out of basal ice rather than being sampled from beneath ice (Vogel, 2004, p. 61), show C:N ratios almost as low as those observed in the modern sub-ice shelf sediments of RISP and lower than those observed at the modern grounding line sediments of WGZ which likely receive an influx of subglacial sediment (Fig. 2.2c; Fig. 2.3). Microbial activity, including microbial consumption of nitrogen, is either nil or very slow in sediments incorporated into basal ice as compared to subglacial sediments (Montross et al., 2014). Thus, we interpret that UC's basal ice formed through freeze-on after ice shelf re-grounding took place in the Late Holocene, and that the freeze-on process incorporated sediments containing fresh organic marine matter with a low C:N ratio into the ice. Incidentally, this interpretation of observed low C:N ratios in the two sediment samples melted out from the basal ice of UC inspired our approach to modelling high basal temperature gradients resulting from recent ice shelf re-grounding.

Additionally, some evidence supporting recent grounding line re-advance in the Ross Sea sector has been reported in previous studies. Currently the Siple Coast ice streams are thickening (Joughin and Tulaczyk, 2002), which is consistent with ice sheet advance. Furthermore, the Siple Coast ice streams have experienced stagnation

and reactivation in the past thousand years (Catania et al., 2012), which could potentially be part of the ice shelf grounding process. After examining folds within the Ross Ice Shelf, Hulbe and Fahnestock (2007) concluded that the Whillans Ice Stream must have stopped flowing around 850 years ago. However, we provide an alternative explanation for the folds in the ice layers by positing that they did not form as the ice stream slowed down, but rather as a result of ice shelf grounding. Evidence supporting recent floatation of the lower part of Kamb Ice Stream found by Catania et al, (2005, 2006) is consistent with the grounding line re-advancing to its modern position within the last few hundred years. Finally, very recent grounding of a thin ice shelf produces steep basal temperature gradients, which should result in a rapid basal freezing that may be responsible for the observed frozen-on basal layers found in KIS boreholes (Christoffersen et al., 2010; Vogel et al., 2005) and at WGZ (unpublished data).

4.3 Patterns of Grounding Line Retreat in Ross Sea Embayment

There have been disagreements about post-LGM grounding line retreat in the central Ross Sea (Ackert, 2008; Bart et al., 2018; Conway et al., 1999; Halberstadt et al., 2016; Kingslake et al., 2018; Lee et al., 2017; Lowry et al., 2019; McKay et al., 2016; Prothro et al., 2020; Spector et al., 2017), due to few reliable age constraints from areas covered by the Ross Ice Shelf and the ice sheet itself (Anderson et al., 2014). Previous conjectures about grounding line retreat in the Ross Embayment have varied. Some followed the “swinging gate” model (Conway et al., 1999)

whereby the grounding line along the Marie Byrd Land side of the Ross Embayment stayed put ("hinged") near the King Edward VII Peninsula while swinging back along the Transantarctic Mountains in the other side of the Ross Embayment. Others have proposed the "saloon door" model, which envisions that the grounding line began retreating first in the central Ross Embayment and the sides caught up later. Our results are broadly consistent with either of these conceptual models. Exposure age dating along the Scott Coast of the Transantarctic Mountains indicates that the grounding line reached Beardmore and Shackleton glaciers ca. 8000 years ago (Spector et al., 2017). We find that the grounding line retreated over SLW 4300^{+1500}_{-2500} years ago, which would suggest that the grounding line retreated faster along the Transantarctic Mountains, as described in the "swinging gate" model. Conversely, the fact that the grounding line retreated over SLW and WIS earlier than KIS and BIS rather than at the same time could suggest that the grounding line retreated followed a pattern more in line with the "saloon door" model. Although our age constraints from the Siple Coast ice streams provide added information about grounding line positions, they do not provide constraints on the geometry of the grounding line during early stages of retreat.

These two models have been the enduring paradigms of post-LGM grounding line retreat in the Ross Embayment, however, we suggest that they are too simplistic a representation of grounding line activity because they treat the ice sheet which retreated across the Ross Embayment as a single entity. Currently the Ross Ice Shelf is ungrounded and therefore does behave as a single entity. But there is no reason to

expect a uniform retreat from a marine ice sheet that is sitting on a bed with variable bathymetry (Fretwell et al., 2013; Tinto et al., 2019). Using the logic of the marine ice sheet instability (Weertman, 1974), we would expect the grounding line to retreat faster in the troughs and to linger on the bathymetric highs. Recent examinations of geomorphic features in front of the current Ross Ice Shelf edge indicate that the post-LGM grounding line retreat initiated in troughs and left behind transient ice rises (Halberstadt et al., 2016; Prothro et al., 2020). We would like to extend that idea and speculate that the rapid grounding line retreat seen along the Transantarctic Mountains between 8,600 years ago and 8,000 years ago (Spector et al., 2017) was facilitated by a relatively deep trough visible in the bathymetry below the Ross Ice Shelf (Fig. 2.1) (Fretwell et al., 2013; Tinto et al., 2019). We believe that the mechanism of grounding line retreat is much more sensitive to bathymetry than is represented in the two canonical models of post-LGM grounding line retreat.

4.4 Holocene Climate-Driven Grounding Line Fluctuations

There are varied ideas in the scientific literature as to the mechanisms causing the Holocene grounding line advance in the Ross Embayment. Kingslake et al. (2018) proposed that the grounding line re-advance was dominantly due to glacioisostatic rebound following unloading from ice sheet thinning and retreat. Lowry et al. (2019) suggest that this retreat is earlier than, and incompatible with, estimates of ice surface lowering in the Transantarctic Mountains as determined by exposure age dating. Here, we propose that both the grounding line retreat and re-

advance is attributable to Holocene climate variability. The timing of grounding line retreat (re-advance) coincides with atmospheric warming (cooling) seen in the WAIS Divide ice core (Fig. 2.8) (Cuffey et al., 2016; Cuffey, 2017). Radiocarbon dating of elephant seal skins found on raised beaches along the Victoria Land Coast indicate two periods during the Holocene when ocean temperatures in this region were warm enough to suppress sea ice formation (Hall et al., 2006). The timing of the first warm period (6800 – 4500 years ago) corresponds reasonably well to the grounding line retreat over SLW and WIS, and the second (2300 – 1000 years ago) coincides with grounding line retreat over KIS and BIS. Following the most recent warm period, ocean temperatures cooled and sea ice cover expanded (Hall et al., 2006). The timing of this ocean cooling corresponds to the cooling period inferred from $\delta^{18}O$ measured in the WAIS Divide ice core (Cuffey et al., 2016; Cuffey, 2017) and is consistent with our estimates of grounding line re-advance over KIS, BIS, and SLW, suggesting that the grounding line re-advance was caused by ocean cooling. This is in agreement with results from WAIS simulations indicating Holocene grounding line positions to be most sensitive to ocean temperatures (Lowry et al., 2019). Our results from temperature diffusion modelling place the most likely timing of grounding line re-advance over WIS during the second warm period. However, given the error it is possible that the re-grounding at WIS may have started during the earlier cool period (3800- 2300 years ago). Further evidence for ocean temperatures driving grounding line motion is that our results are compatible with warming and cooling in the Ross Sea as indicated by analysis of diatoms in sediment cores (Cunningham et al., 1999).

Cunningham et al. (1999) found a period of Ross Sea warming from 7000 to 3200 years ago, which coincides with the timing of grounding line retreat over SLW and WIS, and KIS and BIS within error. Cunningham et al. (1999) additionally proposed a period of cooling from 3200 years ago to present, which coincides with grounding re-advance over all four of our field sites. The proposed high sensitivity of WAIS grounding line positions to relatively small Holocene climate variability may have implications for projections of grounding line behavior during the 21st Century as the temperature changes that coincided with the extensive Holocene grounding line retreat are on par with projections of temperature changes by the end of this century (Fig. 2.8) (Collins et al., 2013; Cuffey et al., 2016; Cuffey, 2017).

4.5 Revisiting the Unicorn Paradox

One puzzling observation noted by Engelhardt (2004) about observed basal temperature gradients from the Siple Coast was the difference in basal temperature gradients at UC and WIS. UC is completely surrounded by the Whillans Ice Stream, however, the basal temperature gradients measured at UC were much steeper than those measured a few kilometers away at WIS. Engelhardt (2004) reasoned that cold ice at the bottom of UC could not have formed locally, but rather must have flowed there from Kamb Ice Stream during a proposed "super-surge" event. Given that the grounding line retreated beyond this area within the Holocene (Kingslake et al., 2018), we conjecture that the steep basal temperature gradient is instead a transient signal resulting from recent re-grounding of an ice shelf. If this is correct,

Engelhardt's super-surge event was simply due to this part of the ice sheet experiencing transient ungrounding and re-grounding as the grounding line first retreated upstream, and then subsequently re-advanced over the sites where Engelhardt measured ice temperature profiles. Temperature modelling from this study dates the grounding of UC to between ca. 3600 and ca. 100 years ago. This time frame broadly fits within the range of values of T_i found for SLW. The difference in basal temperature gradients between UC and WIS can be explained by the velocity of the ice. UC is frozen to the bed and has very low surface velocities. Contrarily, WIS has surface velocities of several hundred meters per year. Thus, the ice at the base of WIS reflects migration from upstream and does not record the thermal effects of the recent ice shelf re-grounding in the same way that the slow-moving ice column of UC still does.

5 Conclusions

In this study, we use several lines of evidence and seek to help refine the current understanding of grounding line activity in the Ross Sea after the LGM. Modelling of subglacial radiocarbon concentrations allows us to estimate the length of ocean exposure (T_o) experienced by our field sites following grounding line retreat, and modelling of ice temperature and sediment porewater chemistry data enables us to assess the timing of grounding line re-advance (T_i). Kingslake et al. (2018), who first proposed that the grounding line in the Siple Coast region retreated past its modern positions after the LGM, favored the explanation that their retreat resulted

from a dynamic overshoot and their re-advance was driven by glacioisostatic rebound.

Here, we propose an alternative model whereby the grounding line retreated over our field sites as late as the mid- to late-Holocene and subsequently re-advanced during the late Holocene in response to climate cooling during the last 1000 – 2000 years (or 3800 – 2300 years ago in the case of WIS). Grounding line advance during the late Holocene occurred in spite of the fact that the WAIS Divide ice core shows a ~20% drop in ice accumulation rate over the past 2000 years, from a maximum reached around 4000 years B.P. (Buizert et al., 2015) – that is when our data suggest grounding line retreat. This counterintuitive relationship between ice input rates and grounding line motion places emphasis on ice-ocean interactions as the process capable of translating modest Holocene climate changes (corresponding to temperature variations of less than 2ºC at WAIS Divide) to grounding line migration of hundreds of kilometers (Lowry et al., 2019). By suggesting strong climate sensitivity with regard to both retreat and advance, our hypothesis may raise further concern for accelerated future grounding line retreat with increasingly warmer sub-ice shelf oceanic input. We note that it is now recognized that at least some sections of the Greenland ice sheet retreated during the mid-Holocene climate optimum, and re-advanced during the late Holocene cooling (Vasskog et al., 2015). Further investigations into the relationship of these Antarctic and Greenland ice sheet fluctuations to Holocene climate variability present an opportunity to reveal the

sensitivity of these ice sheets to the slightly warmer climate states that may be reached in the very near future.

Our results are conjectural, largely because they are based on samples and measurements collected for other research reasons. However, our study highlights the value of maintaining archival materials because we were able to glean a greater understanding of grounding line movement in the Ross Sea by applying new modelling approaches to previously published data collected in different locations from multiple drilling projects over a period of more than 40 years. Future focused studies may be able to test our hypothesis. Similar efforts should also be aimed at other Antarctic ice sheet margins where it may be generally assumed that the grounding line was insensitive to Holocene climate variability, simply because no positive evidence has yet been collected. Insights into the response of Antarctic grounding lines to Holocene climate changes will inform projections of Antarctic ice sheet evolution under near-future climates, regardless of whether such insights will indicate high climate sensitivity or a general lack of climate sensitivity.

Chapter 3: Mechanism for the Subglacial Formation of Cryogenic Brines

Abstract

Cryogenic brines have been found in deep boreholes in places that were formerly glaciated in the Northern Hemisphere as well as in Antarctica. These brines represent a potential expansive microbial habitat, may provide an important source of nutrients to the coastal ocean, and can provide information about past ice sheet climate sensitivity through mineral precipitation. Cryogenic brines form through cryoconcentration of seawater, although the actual environment and mechanism of formation has been debated (Starinsky and Katz, 2003). Previous conceptual models of brine formation require seawater to be periodically isolated from the ocean in a basin which freezes over. We propose instead that they may form in pore spaces of marine sediments which have experienced repeat cycles of ice sheet advance and retreat. Basal freezing concentrates the brines and induces downward flow driven by unstable density stratification. Simulating these repeated cycles of ice sheet advance and retreat with an advection-diffusion model of porewater chemistry, we successfully recreated the porewater chemistry of two deep Antarctic cores (AND-1B and AND-2A). We are able to match the major features of the AND-1B porewater chemistry after seven glacial cycles, and the AND-2A porewater chemistry after

nineteen cycles, suggesting that cryogenic brines can be formed through the repeated isolation and cryoconcentration of marine waters within sediment pore spaces.

1 Introduction

Cryogenic brines are ubiquitous in formerly glaciated regions in the Northern Hemisphere, having been found in deep boreholes across the Canadian Shield (Bottomley et al., 1994; Frape and Fritz, 1982) and Fennoscandia (Starinsky and Katz, 2003). Additionally, cryogenic brines have been found in the porewater of two deep boreholes drilled into the seafloor in McMurdo Sound, Antarctica (Frank et al., 2010; Pompilio et al., 2007) and underneath Taylor Glacier (Lyons et al., 2019). Although it appears as though these subsurface cryogenic brines are more rare in the Antarctic than the Arctic, this may simply be due to the difficulty of obtaining samples from below the ice sheet. In fact, subsurface brines may be widespread around the edges of the Antarctic continent where freezing occurs at the bed (Foley et al., 2019). However, these areas remain largely unsampled as drilling has been biased towards fast-flowing ice (Kamb, 2001; Tulaczyk et al., 2014). These brines are important because they may be responsible for a significant nutrient flux into the coastal ocean (Foley et al., 2019; Lyons et al., 2019; Null et al., 2019; Wadham et al., 2010, 2013) and represent a key microbial environment (Mikucki et al., 2009). Additionally, subglacial brines may precipitate minerals that record ice sheet sensitivity to climate changes (Blackburn et al., 2020). These cryogenic brines may also be of interest to planetary scientists as they are likely similar to the types of fluids hypothesized to exist on other planetary bodies (namely Mars, Europa, and

Enceladus) and are therefore the most likely environment for finding an extraterrestrial microbial habitat in our own Solar System. Chemical signatures in the brines found in both the Arctic and the Antarctic indicate that they are derived from the freezing (cryoconcentration) of seawater (Frank et al., 2010; Lyons et al., 2019; Starinsky and Katz, 2003). However, there has been debate about the mechanisms allowing for the cryoconcentration of these brines and about the geologic environments in which they form (Starinsky and Katz, 2003).

The prevailing conceptual models for the formation of these cryogenic brines require the isolation of marine waters from the ocean (Grasby et al., 2013; Starinsky and Katz, 2003). Starinsky and Katz (2003) proposed a model that invokes glacial isostatic adjustment resulting from cycles of glacial advance and retreat. Formation of an ice sheet depresses the lithosphere and creates a forebulge at the margin of the ice sheet. A trough forms on the inland side of the forebulge, which seawater then infiltrates. Sea-ice then forms on the surface of the seawater, creating a denser brine which seeps into the sediments below. Differing slightly, Grasby et al. (2013) propose that these brines form when thermokarst lakes filled with seawater are annually cut off from the ocean by sea ice formation. Both of these models require semi-isolated marine basins that freeze over. Brines form in these basins when sea ice grows. They then sink to the bottom of the basin and seep into the sediment porespaces. Although the idea of an isolated marine basin could be used to explain the formation of cryogenic brines found in the Northern Hemisphere, it is difficult to transplant that idea to the Ross Sea Sector of Antarctica due to a lack of evidence for

bathymetric highs large enough to have isolated marine waters from the ocean in the past (Tinto et al., 2019). Thus, we propose an alternative model, in which these brines form in the sediment pore spaces below an ice sheet, and do not require the presence of an isolated marine basin.

In this study we model the concentration of Cl^- and $\delta^{18}O$ in sediment porewaters that have experienced multiple cycles of glacial retreat and advance. We compare our results to brines found in cores AND-1B (recovered in 2006) and AND-2A (recovered in 2007). The AND-1B and AND-2A drill sites are located 935.76 m (Falconer et al., 2007) and 384 m (Florindo et al., 2008) below sea level, respectively, beneath the McMurdo Ice Shelf in Antarctica (Fig. 3.1), and were drilled as part of the ANDRILL (Antarctic Drilling) Project.

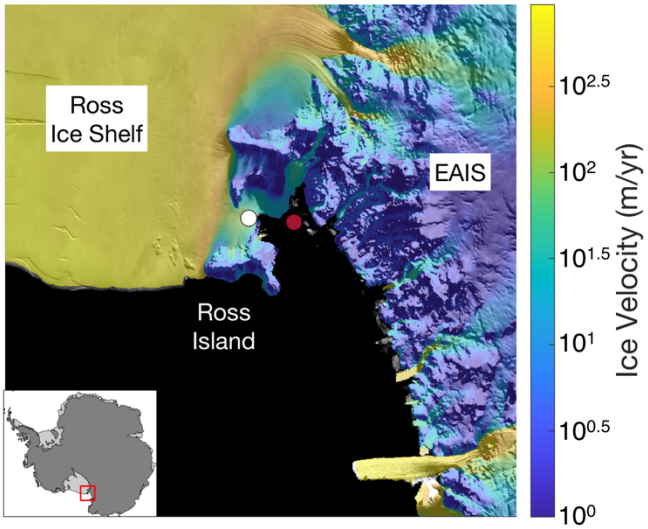

Figure 3.1: Location of AND-1B (white) and AND-2A (red) boreholes. Ross Sea is indicated in black. MODIS Mosaic of Antarctica (Haran et al., 2021) and velocity data (Rignot et al., 2017) are plotted using Antarctic Mapping Tools (Greene et al., 2017).

2 Methods

We modelled the formation and vertical dispersal of cryogenic brines using a one-dimensional vertical advection-diffusion simulation finite-difference code solving the vertical advection-diffusion equation of the form:

$$\frac{\partial C}{\partial t} = \nabla \cdot (D_{sed} \nabla C) - \nabla \cdot (vC) \quad (1)$$

Where C is chemical concentration, t is time, D_{sed} is the diffusion coefficient of the chemical parameter through sediments, and v is the velocity of the brine. We used chemical brine concentrations measured from porewater in cores AND-1B and AND-2A to test the potential applicability of our model outputs (Frank et al., 2010; Pompilio et al., 2007). We modelled porewater concentrations of Cl^- and $\delta^{18}O$ for a sediment column 2 km long (seafloor to 2000 mbsf) which has experienced simplified 100,000-year cycles of ice sheet retreat and re-advance. In the model periods when the sediment column is overlain by ice, we consider two different scenarios: one in which the ice base is melting and one in which it is freezing (Fig. 3.2). We chose to model the concentrations of Cl^- and $\delta^{18}O$ because we did not expect that they interacted chemically with the sediments at temperatures prevailing in the shallow subsurface (Morin et al., 2010). Thus, we assumed that the concentrations of Cl^- and $\delta^{18}O$ found in the porewater were indicators of freezing- and transport-related processes in the sedimentary column that is experiencing changes to Cl^- and $\delta^{18}O$ concentrations at its top during 100,000-year glacial cycles.

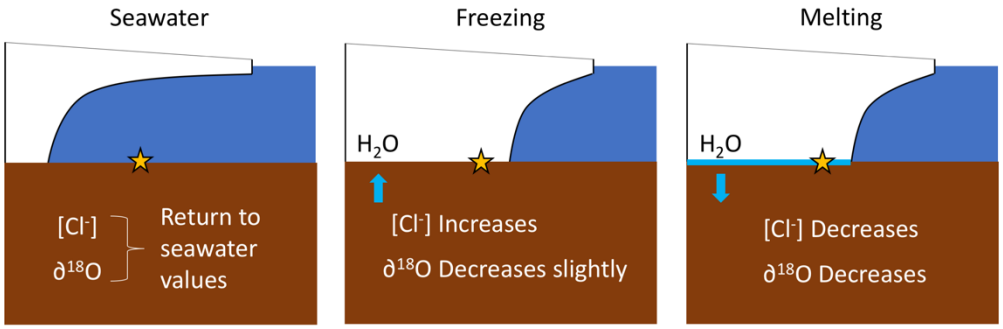

Figure 3.2: Schematic for the three different periods examined during the 100,000-year model runs. During seawater periods, the porewater in the topmost element reflect seawater concentrations. During subglacial periods when the ice is frozen to the bed (i.e., freezing periods), Cl^- concentration increases, and $\delta^{18}O$ decreases slightly. During subglacial periods when melting is occurring at the bed, Cl^- decreases, and $\delta^{18}O$ decreases significantly.

We calculated the diffusion coefficients for Cl^- and $\delta^{18}O$ in sediments using the self-diffusion coefficients reported in Li and Gregory (1974) and Wang (1951) respectively, and accounting for increasing temperature with depth. The equation used for calculating D_{sed} was taken from Li and Gregory (1974):

$$D_{sed} = D\frac{\alpha}{\theta^2} \quad (2)$$

Where D is the self-diffusion coefficient, α is the ratio of viscosity of the bulk solution to the average viscosity of the interstitial solution, and θ is tortuosity. Because α is a constant close to one (Li and Gregory, 1974), we assumed that it was one for simplicity. We calculated θ using an equation from Boudreau (1996):

$$\theta^2 = 1 - ln(\varphi^2) \quad (3)$$

Where φ is porosity, taken here to be 0.4 (Engelhardt et al., 1990; Tulaczyk et al., 2001). The self-diffusion coefficients were reported at 0 ºC, 18 ºC, and 25 ºC for Cl^-

(Li and Gregory, 1974), and at 0 ºC, 5 ºC, 15 ºC, 25 ºC, 35 ºC, 45 ºC, and 55 ºC for $\delta^{18}O$ (Wang, 1951b). We calculated D_{sed} for each of these measurements and fit an Arrhenius equation to the data to obtain a temperature dependence of D_{sed}. Because our domain extends from 0 – 2000 mbsf, the temperatures over which we model diffusion vary widely (-2.4 - 150 ºC [Morin et al., 2010]), which, in turn, varies the diffusivities. We then converted the calculated temperature dependence of D_{sed} to depth dependence using the temperature-depth relationship calculated from measurements at the AND-1B borehole (Morin et al., 2010). The range in D_{sed} used in the model was 0.0105-0.2217 m^2/yr for Cl^- and 0.0153-0.3177 m^2/yr for $\delta^{18}O$.

In addition to diffusion, we accounted for density-driven vertical flow of the brine in our finite-difference code. We calculated the vertical velocity (v) using an expression based on Darcy's Law (Wooding, 2007):

$$v = K\frac{\Delta\rho}{\rho} \quad (4)$$

Where K is the hydraulic conductivity of the sediments and ρ is the density of the porewater. $\Delta\rho$ represents the difference in porewater density between one element and the element directly above it. When $\Delta\rho$ is negative – i.e., the porewater density of the lower element is higher – density stratification is stable and we set the velocity to zero. When $\Delta\rho$ is positive, it is divided by the density to calculate the downward hydraulic gradient. In our model runs we examined values of K ranging from 0.001 – 0.1 m/yr, which we keep constant throughout the model domain. We calculated the density of the porewater from the concentration of Cl^- by assuming that our porewater

had a ratio of total dissolved solids (TDS) to Cl^- of 1.8 (the ratio of TDS to chlorinity in standard seawater). Because changes in oxygen isotopes do not vary the density of the porewater noticeably, we relied on the concentration of chloride to determine whether or not density-driven flow occurred. Thus, we ran the model for both chemical parameters in parallel, using the velocities calculated from the Cl^- density gradients to calculate vertical advection of $\delta^{18}O$.

In our model, we assume that the differences in concentration of Cl^- and $\delta^{18}O$ are negligible in the horizontal direction. Thus, while we expect that there is a horizontal exchange of Cl^- and $\delta^{18}O$ on the microscale (e.g., due to salt fingering under unstable stratification), we assume that the horizontal gradients in chemical concentration and velocity are much smaller than the vertical gradients at the spatial scale of our model resolution (5 meters). This allows us to simplify Equation 1 by ignoring tracer advection in the horizontal direction. After making this assumption and differentiating the diffusive term in Equation 1, the equation becomes:

$$\frac{\partial C}{\partial t} = D_{sed}\frac{\partial^2 C}{\partial z^2} + \frac{\partial D_{sed}}{\partial z}\frac{\partial C}{\partial z} + K\frac{\Delta\rho}{\rho}\frac{\partial C}{\partial z} \quad (5)$$

Where z is depth below the seafloor (zero at the top of the sedimentary column and positive downward).

In our model runs, we exposed the simulated sedimentary column to three different versions of upper boundary conditions (Fig. 3.2), representing the different parts of a simplified glacial cycle: (i) seawater exposure representing the warm parts of climate cycles (e.g., modern conditions) when ice is not in contact with the

seafloor, (ii) basal melting when the ice sheet is overriding the study site and climactic (e.g., surface temperature) as well as glaciological conditions (e.g., large ice thickness) lead to a positive thermal energy balance at the ice base, and (iii) basal freezing when the ice sheet is overriding the study site and climactic and glaciologic conditions lead to a negative thermal energy balance at the ice base. For simplicity, we refer to these three types of upper boundary conditions as: seawater periods, meltwater periods, and freezing periods, respectively.

Changing the upper boundary conditions was simplest during the seawater periods. During the seawater periods, we changed the values of Cl^- and $\delta^{18}O$ concentration in the topmost element to reflect the composition of seawater as measured from samples obtained from above the boreholes (Frank et al., 2010; Pompilio et al., 2007) and allowed the model to run.

During the meltwater periods we added freshwater to the uppermost element at a rate determined by the melt rate. We initially calculated a melt rate of 5×10^{-4} m/yr using equation 9 from Christoffersen and Tulaczyk (2003). However, because that calculation required a number of assumptions about ice sheet conditions, we opted to use that value as a suggestion of the actual melt rate and tested a variety of similar melt rates (Table 3.1). We lowered the Cl^- concentration of the topmost element by simply increasing its dilution based on the rate of melt. To account for the added meltwater in our calculations of $\delta^{18}O$, we assumed that the melted ice had a $\delta^{18}O$ ranging from -60 to -40 (Wang et al., 2010) and settled on a value that fit the

observations from AND-1B and AND-2A best (Table 3.1). We then took the weighted average of the meltwater and porewater based on volume.

Table 3.1: List of free model parameters and the ranges over which they were allowed to vary in the model runs.

Parameter	Range Examined	Units
K	0.001-0.1	m/yr
Freezing Rate	10^{-5}-10^{-3}	m/yr
Melting Rate	10^{-4}-10^{-1}	m/yr
Freezing Periods	0-90,000	Years
Melting Periods	0-90,000	Years
Seawater Periods	10,000-100,000	Years

During the freezing periods, we altered the values of Cl^- concentration and $\delta^{18}O$ by extracting freshwater at a rate set by the freezing rate (Table 3.1). The extracted water leaves the simulated domain, and, in reality, would become part of a frozen basal ice layer (Christoffersen et al., 2010). We began with the assumption that the freezing rate was the same order of magnitude as the melting rate (10^{-4}) and then modified it as a control parameter to fit the observations from AND-1B and AND-2A (Table 3.1). We increased the Cl^- concentration in the topmost element by subtracting the mass of water that froze. This is equivalent to assuming that during freezing no significant Cl^- is incorporated into the basal ice and all of it stays in the pore spaces beneath the ice base. Although Cl^- is soluble in ice, so ice that forms from Cl-bearing fluids (e.g. seawater or brine) will contain some chlorine, the amount of Cl^- incorporated in the ice amounts to ca. 0.1% of the Cl^- concentration in the fluid (Gross et al., 1977). Because this is such a small proportion of the Cl^- concentration in the brine, we feel justified in neglecting this effect. To calculate the $\delta^{18}O$ evolution

in the topmost element during freezing, we relied on the observation that $\delta^{18}O$ of sea ice is 3 permil more positive than the remaining seawater from which it froze (Toyota et al., 2013). We thus lowered the value of $\delta^{18}O$ in the topmost element accounting for the difference in volume between the frozen water and the water remaining in the pore spaces. A visual representation of the effects on the concentration of the uppermost element caused by changing between seawater, freezing, and melting periods can be seen in Fig. 3.3 and Fig. 3.4.

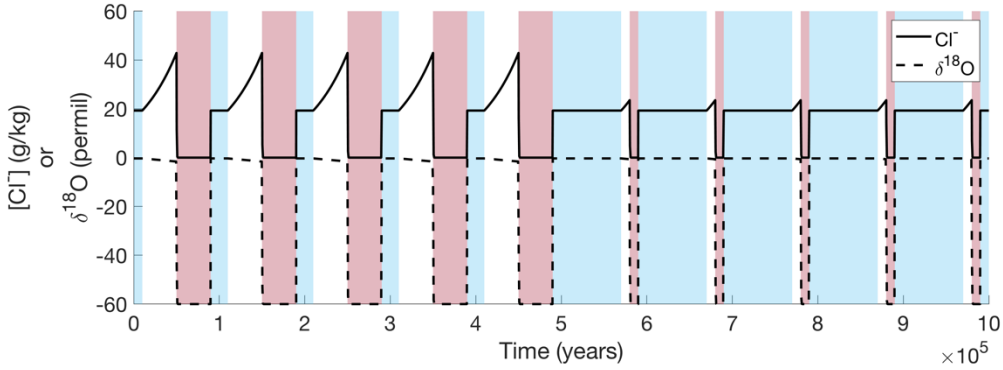

Figure 3.3: Surface boundary conditions for model runs for AND-1B core. The black lines represent Cl^- concentration or the $\delta^{18}O$ for the uppermost element. The blue, white, and red backgrounds indicate the timing of seawater, freezing, and melting periods respectively.

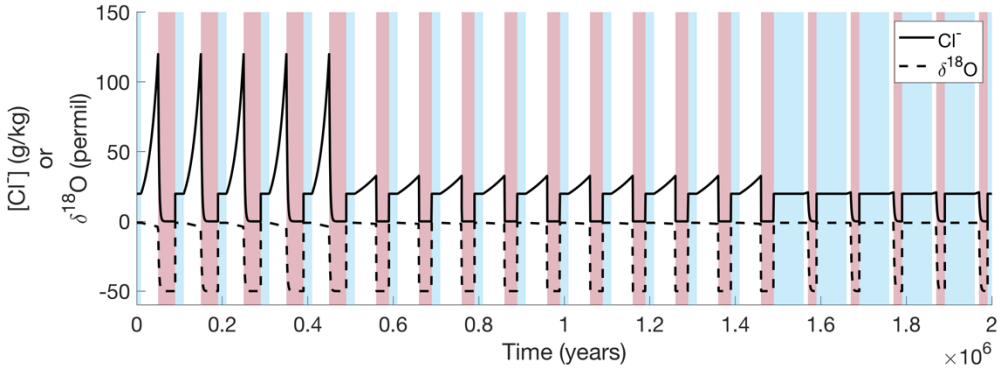

Figure 3.4: Surface boundary conditions for model runs for AND-2A core. The black lines represent Cl^- concentration or the $\delta^{18}O$ for the uppermost element. The blue, white, and red backgrounds indicate the timing of seawater, freezing, and melting periods respectively.

We ran the model, altering the free parameters in order to allow the model outputs to fit the observations from AND-1B and AND-2A respectively. We used a spatial resolution of 5 m and a temporal resolution of 10 years, and ran the simulation by repeating 100,000-year cycles, containing periods of exposure to seawater, melting, and freezing. We ended each model run with a 10,000 year seawater period because the ice sheet has been absent from both the AND-1B and AND-2A sites during the past ca. 10,000 years of the Holocene (McKay et al., 2016; Spector et al., 2017). For each set of observations (i.e. AND-1B and AND-2A), we varied the lengths and arrangements of the periods of seawater, melting, and freezing to fit our model outputs to the observations (Fig. 3.3; Fig 3.4). We also tested a wide variety of values for *K*, freezing rate, and melting rate. We determined the fit for the modelled concentrations of Cl^- and $\delta^{18}O$ to the observations by performing a regression and calculating the R^2 value.

3 Results

We were able to fit our model simulations to the observed concentrations of Cl^- and $\delta^{18}O$ (Fig. 3.5; Fig. 3.6) using reasonable model parameters and simplified glacial cycles. For both cores the models were better able to fit the Cl^- concentrations than the $\delta^{18}O$ concentrations (Fig. 3.5; Fig. 3.6).

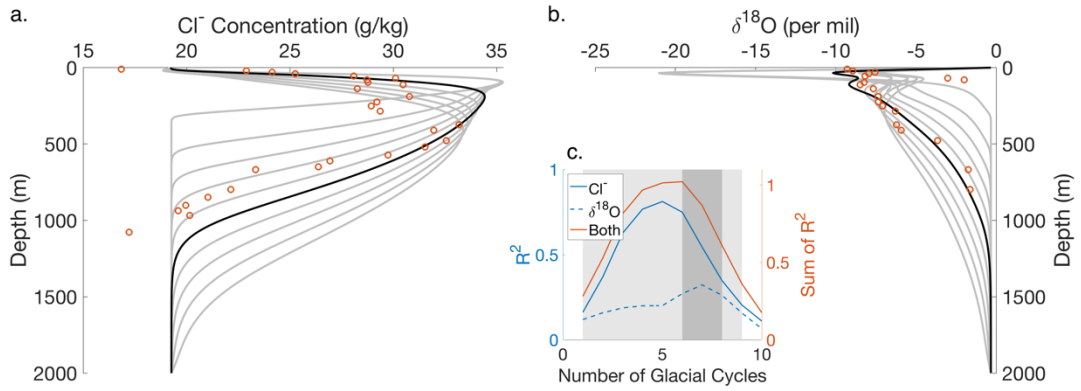

Figure 3.5: Model results compared to observed brine concentrations in the AND-1B core. **(a)** Cl^- concentration. **(b)** $\delta^{18}O$ **(c)** R^2 values indicating model fit after each glacial cycle. Light gray shading denotes cycles over which the R^2 value is significant for Cl^- and the dark gray shading denotes the cycles over which R^2 was significant for both Cl^- and $\delta^{18}O$. The dark lines in **(a)** and **(b)** denote the model results from the glacial cycles that best fit the observations for both Cl^- and $\delta^{18}O$ based on R^2 values shown in **(c)**. The results from 10 glacial cycles are shown in **(a)** and **(b)**.

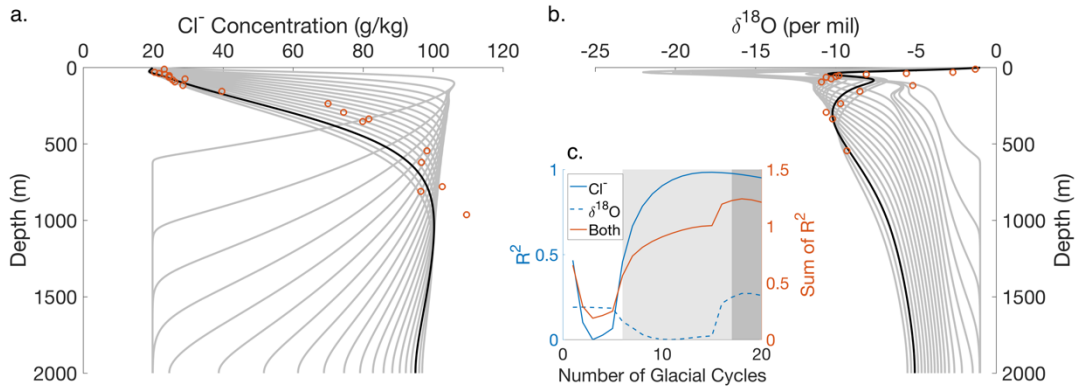

Figure 3.6: Model results compared to observed brine concentrations in the AND-2A core. **(a)** Cl^- concentration. **(b)** $\delta^{18}O$ **(c)** R^2 values indicating model fit after each glacial cycle. Light gray shading denotes cycles over which the R^2 value is significant for Cl^- and the dark gray shading denotes the cycles over which R^2 was significant for both Cl^- and $\delta^{18}O$. The dark lines in **(a)** and **(b)** denote the model results from the glacial cycles that best fit the observations for both Cl^- and $\delta^{18}O$ based on R^2 values shown in **(c)**. The results from 20 glacial cycles are shown in **(a)** and **(b)**.

For the simulation of the AND-1B core, the model was best able to fit the observations within ten 100,000-year glacial cycles (Fig. 3.5). The solution we found that best fit the observations required the first five glacial cycles to differ slightly from the following five cycles. For cycles 1-5 the sediments were exposed to 10,000 years of seawater conditions, followed by 40,000 years of freezing conditions, 40,000 years of melting conditions, and 10,000 years of seawater conditions. For cycles 6-10 we increased the amount of time the sediments were exposed to seawater: 70,000 years of seawater conditions, 10,000 years of freezing conditions, 10,000 years of melting conditions, and 10,000 years of seawater conditions. These cycles are visually represented in Fig. 3.3. For all glacial cycles *K* was 0.09 m/yr, the freezing rate was $4x10^{-5}$ m/yr, and the melting rate was 0.01 m/yr. The model outcome that

produced the best fit for the combination of Cl^- and $\delta^{18}O$ occurred after six glacial cycles (Fig. 3.5c).

For the AND-2A core, the solution we found that best fit the observed data required more than ten 100,000-year glacial cycles (Fig. 3.6). The first five glacial cycles were the coldest with a freezing rate of $9x10^{-5}$ m/yr and a melt rate of 0.001 m/yr. These cycles began with 10,000 years of seawater conditions, followed by 40,000 years of freezing conditions, 40,000 years of melting conditions, and a final 10,000 years of seawater conditions. During glacial cycles 6-15 the sediments experienced slightly longer periods of freezing conditions, but the conditions at the bed were slightly warmer, resulting in a lower freezing rate ($2x10^{-5}$ m/yr) and a higher melting rate (0.1 m/yr). The glacial cycles followed the pattern of 10,000 years of seawater conditions, 50,000 years of freezing conditions, 30,000 years of melting conditions, and 10,000 years of seawater conditions. The final five glacial cycles (cycles 16-20) consisted of cycles of 60,000 years of seawater conditions, 10,000 years of freezing conditions (freezing rate of 10^{-5} m/yr), 20,000 years of melting conditions (melting rate of 10^{-3} m/yr), and 10,000 years of seawater conditions. These cycles are visually represented in Fig. 3.4. Throughout all glacial cycles, the value for *K* was 0.09 m/yr. The model outputs that produced the best fit for the combination of Cl^- and $\delta^{18}O$ observations occurred after 18 glacial cycles (Fig. 3.6c).

4 Discussion

The model was able to create cryogenic brines of similar chlorinity and $\delta^{18}O$ composition to the brines observed in the pore spaces of sediments which were repeatedly subject to glacial overriding and retreat. For both cores, the model was able to reproduce the observed Cl^- concentrations better than the $\delta^{18}O$ concentrations (Fig. 3.5; Fig. 3.6). This could be due to flaws in the way we alter the concentration $\delta^{18}O$ during melting or freezing conditions or because we also do not account for the lowering of $\delta^{18}O$ in the porewater due to carbonate formation (Staudigel et al., 2018). Regardless, because the model was able to generally reproduce observed chemical concentrations, we conclude that cryogenic brines may form in sediment pore spaces rather than in an isolated marine basin. This mechanism is a more plausible explanation in this setting (McMurdo Sound). Given the current lack of a forebulge in the presence of the Antarctic Ice Sheet or a moraine large enough to cut off access to the ocean, it is unlikely that these locations were isolated from the ocean except when overridden by ice.

Given the number of free parameters tuned to allow the model outputs to fit the observations from the AND-1B and AND-2A cores, it is unlikely that our results are unique. Therefore, we cannot deduce with any confidence the length of time the sediments were exposed to seawater, freezing, and melting periods throughout the glacial cycles. However, the fact that were successful in reproducing the observations, assuming reasonable parameter values (Table 3.1), indicates that it is possible to form cryogenic brines in the pore spaces of marine sediments which repeatedly experienced grounding line advance and retreat.

Although we grant that our model outputs are probably not unique, in all of our simulations we found that more glacial cycles were required to fit the observations from the AND-2A core than the AND-1B core. This could be due to the large difference in water depth at these two field sites (935.76 m at AND-1B [Falconer et al., 2007] and 384 m at AND-2A [Florindo et al., 2008]). In order for the grounding line to advance over the AND-1B site, the ice would have to be at least 1 km thick to avoid floatation. In contrast, an ice sheet ca. 500 m thick would be able to be grounded at the AND-2A site. Because the ice sheet does not need to experience as much thickening to advance over the AND-2A site, it is plausible that during the past two million years the ice sheet thickened enough to advance over the AND-2A site but not the AND-1B site. Thus, the sediments at the AND-2A site may have experienced more cycles of ice advance and retreat during the past two million years.

An important observation from the modelling process was that we were unable to recreate the brine concentrations at depth without incorporating density driven flow. Diffusion alone was not able to account for the high concentrations at depth. Additionally, a relatively high (although not implausible) value of K was required to drive the brines downward. This indicates that these sediments are highly permeable, which could be due to a combination of porosity and fracturing (Paulsen et al., 2008). However, this density-driven downward flow is not without precedent as the previous models for the formation of cryogenic brines require the denser brines

to sink to the bottom of the isolated marine basin and percolate deep into the sediments (Grasby et al., 2013; Starinsky and Katz, 2003).

Additionally, we tested what effect imposing a uniform vertical groundwater flow (as opposed to the more targeted density-driven flow) would have on our results. Imposing a background downward vertical velocity appeared to affect the changes to the brine concentrations during the freezing periods more than it did the seawater or melting periods, resulting in greater changes to the Cl^- concentration (which increases during the freezing periods) than the $\delta^{18}O$ (which becomes more negative during the melting phases). We attempted to fit the model outcomes to the observations by altering the length of freezing periods and changing the freezing rate, but found that we were unable to reproduce a reasonable fit for the entire Cl^- profile. Thus, although we do not rule out a background flow entirely, we conclude that density-driven flow is predominant mode of vertical flow of fluids at the AND-1B and AND-2A field sites.

A summary of our proposed mechanism for cryogenic brine formation looks thus: when the sediments are exposed to the ocean, the uppermost sediments exchange with the ocean, thus adding Cl^- (Fig. 3.2). When the sediments are overridden by ice, freezing at the base removes fresh water, thus increasing the concentration of Cl^- in the porewater. Additionally, because water preferentially freezes ^{16}O, the $\delta^{18}O$ in the porewater becomes slightly more negative. Because this cryoconcentrated water is denser than the water below, it sinks. When conditions at the base of the ice become conducive to melting, glacial meltwater is introduced to

the topmost sediments, thus diluting the concentration of Cl^- and lowering the $\delta^{18}O$ considerably. Because this water is less dense than the water below it, it does not sink, although diffusion of the chemical species does occur. The ice then retreats, and the topmost sediments are again exposed to the ocean.

5 Conclusions

Our results demonstrate a plausible new mechanism for the formation of cryogenic brines. Rather than being created when isolated marine basins freeze over, we contend that brines can form in the pore spaces of sediments that experience repeated advance and retreat of an ice sheet.

Cryogenic brines have been found in in boreholes in many locations in the Canadian and Fennoscandian Shields (Bottomley et al., 1994; Frape and Fritz, 1982) and may be more prevalent underneath the Antarctic Ice Sheet than we currently know. Because cryoconcentration can occur in sediment pore spaces, it is likely that there are brines hidden in the sediments where the Antarctic Ice Sheet is frozen to the bed (Foley et al., 2019). Sampling of subglacial waters has been biased towards fast-moving ice (Kamb, 2001; Tulaczyk et al., 2014), where the ice sheet is not frozen to the bed and basal melting is prevalent. However, subglacial freezing is occurring along most of the ice sheet margin in Antarctica (Foley et al., 2019), and if we were to sample deep sediment cores at those locations we would find cryogenic brines.

Additionally, similar cryoconcentrated brines may be found on other planetary bodies in the solar system. For instance, there is evidence hinting at the presence of

liquid water below the ice cap on Mars' south pole (Lauro et al., 2021; Orosei et al., 2018). Given the cold temperatures at the base of the Martian ice caps, the liquid water is assumed to contain high solute concentrations. These brines could have formed in the sediment pore spaces in a manner similar to the mechanism proposed here.

List of Supplemental Files

Chapter 2 Supplemental Materials

References

Achberger, A. M., Christner, B. C., Michaud, A. B., Priscu, J. C., Skidmore, M. L., Vick-Majors, T. J., Adkins, W., Anandakrishnan, S., Barbante, C., Barcheck, G., Beem, L., Behar, A., Beitch, M., Bolsey, R., Branecky, C., Carter, S., Christianson, K., Edwards, R., Fisher, A., Fricker, H., Foley, N., Guthrie, B., Hodson, T., Jacobel, R., Kelley, S., Mankoff, K., McBryan, E., Mikucki, J., Mitchell, A., Powell, R., Purcell, A., Sampson, D., Scherer, R., Sherve, J., Siegfried, M. and Tulaczyk, S.: Microbial community structure of subglacial Lake Whillans, West Antarctica, Front. Microbiol., 7(SEP), 1–13, doi:10.3389/fmicb.2016.01457, 2016.

Ackert, R.: Swinging gate or Saloon doors: Do we need a new model of Ross Sea deglaciation?, Fifteenth West Antarctic Ice Sheet Meeting, Sterling, Virginia, 8–11 October 2008.

Adkins, J. F. and Schrag, D. P.: Reconstructing Last Glacial Maximum bottom water salinities from deep-sea sediment pore fluid profiles, Earth Planet. Sci. Lett., 216(1–2), 109–123, doi:10.1016/S0012-821X(03)00502-8, 2003.

Amundson, J. M., Fahnestock, M., Truffer, M., Brown, J., Lüthi, M. P. and Motyka, R. J.: Ice mélange dynamics and implications for terminus stability, Jakobshavn Isbrse, Greenland, J. Geophys. Res. Earth Surf., 115(1), 1–12, doi:10.1029/2009JF001405, 2010.

Anderson, J. B., Conway, H., Bart, P. J., Witus, A. E., Greenwood, S. L., McKay, R. M., Hall, B. L., Ackert, R. P., Licht, K., Jakobsson, M. and Stone, J. O.: Ross Sea paleo-ice sheet drainage and deglacial history during and since the LGM, Quat. Sci. Rev., 100, 31–54, doi:10.1016/j.quascirev.2013.08.020, 2014.

Andrews, J. T., Domack, E. W., Cunningham, W. L., Leventer, A., Licht, K. J., Jull, A. J. T., DeMaster, D. J. and Jennings, A. E.: Problems and possible solutions concerning radiocarbon dating of surface marine sediments, Ross Sea, Antarctica, Quat. Res., 52(2), 206–216, doi:10.1006/qres.1999.2047, 1999.

Arimitsu, M., Piatt, J. and Heflin, B.: Pelagic Forage Fish Distribution Abundance and Body Condition: U.S. Geological Survey data release, , doi:10.5066/F74J0C9Z, 2017.

Åström, J. A.: Statistical models of brittle fragmentation, Adv. Phys., 55(3–4), 247–278, doi:10.1080/00018730600731907, 2006.

Bahr, D. B.: Simulating iceberg calving with a percolation model, J. Geophys. Res., 100(B4), 6225–6232, doi:10.1029/94JB03133, 1995.

Bamber, J. L., Oppenheimer, M., Kopp, R. E., Aspinall, W. P. and Cooke, R. M.: Ice sheet contributions to future sea-level rise from structured expert judgment, Proc. Natl. Acad. Sci. U. S. A., 166(23), 11195–11200, doi:10.1073/pnas.1817205116, 2019.

Baroni, C. and Hall, B. L.: A new Holocene relative sea-level curve for Terra Nova Bay, Victoria Land, Antarctica, J. Quat. Sci., 19(4), 377–396, doi:10.1002/jqs.825, 2004.

Bart, P. J. and Tulaczyk, S.: A significant acceleration of ice volume discharge preceded a major retreat of a West Antarctic paleo-ice stream, Geology, 48(4), 313–317, doi:10.1130/G46916.1, 2020.

Bart, P. J., DeCesare, M., Rosenheim, B. E., Majewski, W. and McGlannan, A.: A centuries-long delay between a paleo-ice-shelf collapse and grounding-line retreat in the Whales Deep Basin, eastern Ross Sea, Antarctica, Sci. Rep., 8(1), 1–9, doi:10.1038/s41598-018-29911-8, 2018.

Bartholomaus, T. C., Larsen, C. F. and O'Neel, S.: Does calving matter? Evidence for significant submarine melt, Earth Planet. Sci. Lett., 380, 21–30, doi:10.1016/j.epsl.2013.08.014, 2013.

Begeman, C. B., Tulaczyk, S. M., Marsh, O. J., Mikucki, J. A., Stanton, T. P., Hodson, T. O., Siegfried, M. R., Powell, R. D., Christianson, K. and King, M. A.: Ocean Stratification and Low Melt Rates at the Ross Ice Shelf Grounding Zone, J. Geophys. Res. Ocean., 123(10), 7438–7452, doi:10.1029/2018JC013987, 2018.

Bentley, M. J., Ocofaigh, C., Anderson, J. B., Conway, H., Davies, B., Graham, A. G. C., Hillenbrand, C. D., Hodgson, D. A., Jamieson, S. S. R., Larter, R. D., Mackintosh, A., Smith, J. A., Verleyen, E., Ackert, R. P., Bart, P. J., Berg, S., Brunstein, D., Canals, M., Colhoun, E. A., Crosta, X., Dickens, W. A., Domack, E., Dowdeswell, J. A., Dunbar, R., Ehrmann, W., Evans, J., Favier, V., Fink, D., Fogwill, C. J., Glasser, N. F., Gohl, K., Golledge, N. R., Goodwin, I., Gore, D. B., Greenwood, S. L., Hall, B. L., Hall, K., Hedding, D. W., Hein, A. S., Hocking, E. P., Jakobsson, M., Johnson, J. S., Jomelli, V., Jones, R. S., Klages, J. P., Kristoffersen, Y., Kuhn, G., Leventer, A., Licht, K., Lilly, K., Lindow, J., Livingstone, S. J., Massé, G., McGlone, M. S., McKay, R. M., Melles, M., Miura, H., Mulvaney, R., Nel, W., Nitsche, F. O., O'Brien, P. E., Post, A. L., Roberts, S. J., Saunders, K. M., Selkirk, P. M., Simms, A. R., Spiegel, C., Stolldorf, T. D., Sugden, D. E., van der Putten, N., van Ommen, T., Verfaillie, D., Vyverman, W., Wagner, B., White, D. A., Witus, A. E. and Zwartz, D.: A community-based geological reconstruction of Antarctic Ice Sheet deglaciation since the Last Glacial Maximum, Quat. Sci. Rev., 100, 1–9, doi:10.1016/j.quascirev.2014.06.025, 2014.

Bigg, G. R., Wadley, M. R., Stevens, D. P. and Johnson, J. A.: Modelling the dynamics and thermodynamics of icebergs, Cold Reg. Sci. Technol., 26(2), 113–135, doi:10.1016/S0165-232X(97)00012-8, 1997.

Bindschadler, R. A., Roberts, E. P. and Iken, A.: Age of Crary Ice Rise, Antarctica, determined from temperature-depth profiles, Ann. Glaciol., 14, 13–16, 1990.

Blackburn, T., Edwards, G. H., Tulaczyk, S., Scudder, M., Piccione, G., Hallet, B., McLean, N., Zachos, J. C., Cheney, B. and Babbe, J. T.: Ice retreat in Wilkes Basin of East Antarctica during a warm interglacial, Nature, 583(7817), 554–559, doi:10.1038/s41586-020-2484-5, 2020.

Bottomley, D. J., Conrad Gregoire, D. and Raven, K. G.: Saline ground waters and brines in the Canadian Shield: Geochemical and isotopic evidence for a residual evaporite brine component, Geochim. Cosmochim. Acta, 58(5), 1483–1498, doi:10.1016/0016-7037(94)90551-7, 1994.

Boudreau, B. P.: The diffusive tortuosity of fine-grained unlithified sediments, Geochim. Cosmochim. Acta, 60(16), 3139–3142, doi:10.1016/0016-7037(96)00158-5, 1996.

Bouhier, N., Tournadre, J., Rémy, F. and Gourves-Cousin, R.: Melting and fragmentation laws from the evolution of two large southern ocean icebergs, Cryosph., 12(7), 2267–2285, doi:10.5194/tc-12-2267-2018, 2018.

Bradley, S. L., Hindmarsh, R. C. A., Whitehouse, P. L., Bentley, M. J. and King, M. A.: Low post-glacial rebound rates in the Weddell Sea due to Late Holocene ice-sheet readvance, Earth Planet. Sci. Lett., 413, 79–89, doi:10.1016/j.epsl.2014.12.039, 2015.

Brunt, K. M., Fricker, H. A., Padman, L., Scambos, T. A. and O'Neel, S.: Mapping the grounding zone of the Ross Ice Shelf, Antarctica, using ICESat laser altimetry, Ann. Glaciol., 51(55), 71–79, doi:10.3189/172756410791392790, 2010.

Buizert, C., Cuffey, K. M., Severinghaus, J. P., Baggenstos, D., Fudge, T. J., Steig, E. J., Markle, B. R., Winstrup, M., Rhodes, R. H., Brook, E. J., Sowers, T. A., Clow, G. D., Cheng, H., Edwards, R. L., Sigl, M., McConnell, J. R. and Taylor, K. C.: The WAIS Divide deep ice core WD2014 chronology – Part 1: Methane synchronization (68-31 ka BP) and the gas age-ice age difference, Clim. Past, 11(2), 153–173, doi:10.5194/cp-11-153-2015, 2015.

Carroll, D., Sutherland, D. A., Shroyer, E. L., Nash, J. D., Catania, G. A. and Stearns, L. A.: Modeling Turbulent Subglacial Meltwater Plumes: Implications for Fjord-Scale Buoyancy-Driven Circulation, J. Phys. Oceanogr., 45(8), 2169–2185, doi:10.1175/JPO-D-15-0033.1, 2015.

Catania, G., Hulbe, C., Conway, H., Scambos, T. A. and Raymond, C. F.: Variability in the mass flux of the Ross ice streams, West Antarctica, over the last millennium, J. Glaciol., 58(210), 741–752, doi:10.3189/2012JoG11J219, 2012.

Catania, G. A., Conway, H., Raymond, C. F. and Scambos, T. A.: Surface morphology and internal layer stratigraphy in the downstream end of Kamb Ice Stream, West Antarctica, J. Glaciol., 51(174), 423–431, doi:10.3189/172756505781829142, 2005.

Catania, G. A., Conway, H., Raymond, C. F. and Scambos, T. A.: Evidence for floatation or near floatation in the mouth of Kamb Ice Stream, West Antarctica, prior to stagnation, J. Geophys. Res. Earth Surf., 111(1), 1–10, doi:10.1029/2005JF000355, 2006.

Chapuis, A. and Tetzlaff, T.: The variability of tidewater-glacier calving: Origin of event-size and interval distributions, J. Glaciol., 60(222), 622–634, doi:10.3189/2014JoG13J215, 2014.

Christner, B. C., Priscu, J. C., Achberger, A. M., Barbante, C., Carter, S. P., Christianson, K., Michaud, A. B., Mikucki, J. A., Mitchell, A. C., Skidmore, M. L., Vick-Majors, T. J., Adkins, W. P., Anandakrishnan, S., Anandakrishnan, S., Beem, L., Behar, A., Beitch, M., Bolsey, R., Branecky, C., Fisher, A., Foley, N., Mankoff, K. D., Sampson, D., Tulaczyk, S., Edwards, R., Kelley, S., Sherve, J., Fricker, H. A., Siegfried, S., Guthrie, B., Hodson, T., Powell, R., Scherer, R., Horgan, H., Jacobel, R., McBryan, E. and Purcell, A.: A microbial ecosystem beneath the West Antarctic ice sheet, Nature, 512(7514), 310–313, doi:10.1038/nature13667, 2014.

Christoffersen, P. and Tulaczyk, S.: Thermodynamics of basal freeze-on: Predicting basal and subglacial signatures of stopped ice streams and interstream ridges, Ann. Glaciol., 36, 233–243, doi:10.3189/172756403781816211, 2003.

Christoffersen, P., Tulaczyk, S. and Behar, A.: Basal ice sequences in Antarctic ice stream: Exposure of past hydrologic conditions and a principal mode of sediment transfer, J. Geophys. Res. Earth Surf., 115(3), 1–12, doi:10.1029/2009JF001430, 2010.

Christoffersen, P., Bougamont, M., Carter, S. P., Fricker, H. A. and Tulaczyk, S.: Significant groundwater contribution to Antarctic ice streams hydrologic budget, Geophys. Res. Lett., 41(6), 2003–2010, 2014.

Church, J.A., P.U. Clark, A. Cazenave, J.M. Gregory, S. Jevrejeva, A. Levermann, M.A. Merri eld, G.A. Milne, R.S. Nerem, P.D. Nunn, A.J. Payne, W.T. Pfeffer, D. Stammer and A.S. Unnikrishnan, 2013: Sea Level Change. In: *Climate Change 2013: The Physical Science Basis. Contribution of Working Group I to the Fifth Assessment Report of the Intergovernmental Panel on Climate Change* [Stocker, T.F., D. Qin, G.-K. Plattner, M. Tignor, S.K. Allen, J. Boschung, A. Nauels, Y. Xia, V. Bex and P.M. Midgley (eds.)]. Cambridge University Press, Cambridge, United Kingdom and New York, NY, USA.

Clark, P. U., Dyke, A. S., Shakun, J. D., Carlson, A. E., Clark, J., Wohlfarth, B., Mitrovica, J. X., Hostetler, S. W. and McCabe, A. M.: The Last Glacial Maximum, Science (80-.)., 325(5941), 710–714, doi:10.1126/science.1172873, 2009.
Clarke, T. S., Liu, C., Lord, N. E. and Bentley, C. R.: Evidence for a recently abandoned shear margin adjacent to ice stream B2, Antarctica, from ice-penetrating radar measurements, J. Geophys. Res. Solid Earth, 105(B6), 13409–13422, doi:10.1029/2000jb900037, 2000.

Collins, M., R. Knutti, J. Arblaster, J.-L. Dufresne, T. Fichefet, P. Friedlingstein, X. Gao, W.J. Gutowski, T. Johns, G. Krinner, M. Shongwe, C. Tebaldi, A.J. Weaver and M. Wehner, 2013: Long-term Climate Change: Projections, Com- mitments and Irreversibility. In: *Climate Change 2013: The Physical Science Basis. Contribution of Working Group I to the Fifth Assessment Report of the Intergovernmental Panel on Climate Change* [Stocker, T.F., D. Qin, G.-K. Plattner, M. Tignor, S.K. Allen, J. Boschung, A. Nauels, Y. Xia, V. Bex and P.M. Midgley (eds.)]. Cambridge University Press, Cambridge, United Kingdom and New York, NY, USA.

Conway, H., Hall, B. L., Denton, G. H., Gades, A. M. and Waddington, E. D.: Past and future grounding-line retreat of the West Antarctic Ice Sheet, Science (80-.)., 286(5438), 280–283, doi:10.1126/science.286.5438.280, 1999.

Crawford, A. J., Mueller, D., Desjardins, L. and Myers, P. G.: The Aftermath of Petermann Glacier Calving Events (2008–2012): Ice Island Size Distributions and Meltwater Dispersal, J. Geophys. Res. Ocean., 123(12), 8812–8827, doi:10.1029/2018JC014388, 2018.

Cuffey, K. M., Clow, G. D., Steig, E. J., Buizert, C., Fudge, T. J., Koutnik, M., Waddington, E. D., Alley, R. B. and Severinghaus, J. P.: Deglacial temperature history of West Antarctica, Proc. Natl. Acad. Sci. U. S. A., 113(50), 14249–14254, doi:10.1073/pnas.1609132113, 2016.

Cuffey, K. M. (2017) "Temperature Reconstruction at the West Antarctic Ice Sheet Divide" U.S. Antarctic Program (USAP) Data Center. doi: https://doi.org/10.15784/600377.

Cunningham, W. L., Leventer, A., Andrews, J. T., Jennings, A. E. and Licht, K. J.: Late Pleistocene-Holocene marine conditions in the Ross Sea, Antarctica: Evidence from the diatom record, Holocene, 9(2), 129–139, doi:10.1191/095968399675624796, 1999.

Demaster, D. J., Dunbar, R. B., Gordon, L. I., Leventer, A. R., Morrison, J. M., Nelson, D. M., Nittrouer, C. A. and Smith, W. O.: Cycling and accumulation of biogenic silica and organic matter in high-latitude environments: the Ross Sea, Oceanography, 5(3), 146–153, doi:10.5670/oceanog.1992.03, 1992.

Dowdeswell, J. a. and Forsberg, C. F.: The size and frequency of icebergs and bergy bits derived from tidewater glaciers in Kongsfjorden, northwest Spitsbergen, Polar Res., 11(2), 81–91, doi:10.1111/j.1751-8369.1992.tb00414.x, 1992.

Enderlin, E. M. and Hamilton, G. S.: Estimates of iceberg submarine melting from high-resolution digital elevation models: Application to Sermilik Fjord, East Greenland, J. Glaciol., 60(224), 1111–1116, doi:10.3189/2014JoG14J085, 2014.

Enderlin, E. M., Hamilton, G. S., Straneo, F. and Sutherland, D. A.: Iceberg meltwater fluxes dominate the freshwater budget in Greenland's iceberg-congested glacial fjords, Geophys. Res. Lett., 43(21), 11,287-11,294, doi:10.1002/2016GL070718, 2016.

Engelhardt, H.: Thermal regime and dynamics of the West Antarctic ice sheet, Ann. Glaciol., 39, 85–92, 2004.

Engelhardt, H. and Kamb, B.: Vertical temperature profile of Ice Stream B, Antarct. JUS, 28(5), 63–66, 1993.

Engelhardt, H., Humphrey, N., Kamb, B. and Fahnestock, M.: Physical conditions at the base of a fast moving Antarctic ice stream, Science (80-.)., 248(4951), 57–59, doi:10.1126/science.248.4951.57, 1990.

Falconer, T., Pyne, A., Levy, R., Olney, M., Curren, M. and ANDRILL MIS Science Team: Operations Overview for the ANDRILL McMurdo Ice Shelf Project, Antarctica, Terra Antarct., 14(3), 131–140, 2007.

Fisher, A. T., Mankoff, K. D., Tulaczyk, S. M., Tyler, S. W. and Foley, N.: High geothermal heat flux measured below the West Antarctic Ice Sheet, Sci. Adv., 1(6), e1500093–e1500093, doi:10.1126/sciadv.1500093, 2015.

Fitzpatrick, J. J., Muhs, D. R. and Jull, A. J. T.: Saline Minerals in the Lewis Cliff Ice Tongue, Buckley Island Quadrangle, Antarctica, in Contributions to Antarctic Research I, vol. 50, pp. 57–69., 1990.

Florindo, F., Harwood, D., Levy, R. and Team, S. P. S.: ANDRILL's Success During the 4th International Polar Year, Sci. Drill., 6, 29–31, doi:10.2204/iodp.sd.6.03.2008, 2008.

Foley, N., Tulaczyk, S. M., Grombacher, D., Doran, P. T., Mikucki, J., Myers, K. F., Foged, N., Dugan, H., Auken, E. and Virginia, R.: Evidence for pathways of concentrated submarine groundwater discharge in east Antarctica from helicopter-borne electrical resistivity measurements, Hydrology, 6(2), doi:10.3390/HYDROLOGY6020054, 2019.

Frank, T. D., Gui, Z. and ANDRILL SMS Science Team: Cryogenic origin for brine in the subsurface of southern McMurdo Sound, Antarctica, Geology, 38(7), 587–590, doi:10.1130/G30849.1, 2010.

Frape, S. K. and Fritz, P.: The chemistry and isotopic composition of saline groundwaters from the Sudbury Basin, Ontario., Can. J. Earth Sci., 19(4), 645–661, doi:10.1139/e82-053, 1982.

Fretwell, P., Pritchard, H. D., Vaughan, D. G., Bamber, J. L., Barrand, N. E., Bell, R., Bianchi, C., Bingham, R. G., Blankenship, D. D., Casassa, G., Catania, G., Callens, D., Conway, H., Cook, A. J., Corr, H. F. J., Damaske, D., Damm, V., Ferraccioli, F., Forsberg, R., Fujita, S., Gim, Y., Gogineni, P., Griggs, J. A., Hindmarsh, R. C. A., Holmlund, P., Holt, J. W., Jacobel, R. W., Jenkins, A., Jokat, W., Jordan, T., King, E. C., Kohler, J., Krabill, W., Riger-Kusk, M., Langley, K. A., Leitchenkov, G., Leuschen, C., Luyendyk, B. P., Matsuoka, K., Mouginot, J., Nitsche, F. O., Nogi, Y., Nost, O. A., Popov, S. V., Rignot, E., Rippin, D. M., Rivera, A., Roberts, J., Ross, N., Siegert, M. J., Smith, A. M., Steinhage, D., Studinger, M., Sun, B., Tinto, B. K., Welch, B. C., Wilson, D., Young, D. A., Xiangbin, C. and Zirizzotti, A.: Bedmap2: Improved ice bed, surface and thickness datasets for Antarctica, Cryosphere, 7, 375–393, doi:10.5194/tc-7-375-2013, 2013.

Fried, M. J., Hulbe, C. L. and Fahnestock, M. A.: Grounding-line dynamics and margin lakes, Ann. Glaciol., 55(66), 87–96, doi:10.3189/2014AoG66A216, 2014.

Frignani, M., Giglio, F., Langone, L., Ravaioli, M. and Mangini, A.: Late Pleistocene-Holocene sedimentary fluxes of organic carbon and biogenic silica in the northwestern Ross Sea, Antarctica, Ann. Glaciol., 27, 697–703, doi:10.3189/1998aog27-1-697-703, 1998.

Gardner, A. S., Moholdt, G., Cogley, J. G., Wouters, B., Arendt, A. a, Wahr, J., Berthier, E., Hock, R., Pfeffer, W. T., Kaser, G., Ligtenberg, S. R. M., Bolch, T., Sharp, M. J., Hagen, J. O., van den Broeke, M. R. and Paul, F.: A reconciled estimate of glacier contributions to sea level rise: 2003 to 2009., Science, 340(6134), 852–7, doi:10.1126/science.1234532, 2013.

Gladstone, R. M., Bigg, G. R. and Nicholls, K. W.: Iceberg trajectory modeling and meltwater injection in the Southern Ocean, J. Geophys. Res., 106(C9), 19903–19915, doi:10.1029/2000JC000347, 2001.

Grasby, S. E., Rod Smith, I., Bell, T. and Forbes, D. L.: Cryogenic formation of brine and sedimentary mirabilite in submergent coastal lake basins, canadian arctic, Geochim. Cosmochim. Acta, 110, 13–28, doi:10.1016/j.gca.2013.02.014, 2013.

Greene, Chad A., et al. "Antarctic Mapping Tools for Matlab." Computers & Geosciences, vol. 104, Elsevier BV, July 2017, pp. 151–57, doi:10.1016/j.cageo.2016.08.003.

Gross, G. W., Wong, P. M. and Humes, K.: Concentration dependent solute redistribution at the ice-water phase boundary. III. Spontaneous convection. Chloride solutions, J. Chem. Phys., 67(11), 5264–5274, doi:10.1063/1.434704, 1977.

Halberstadt, A. R. W., Simkins, L. M., Greenwood, S. L. and Anderson, J. B.: Past ice-sheet behaviour: Retreat scenarios and changing controls in the Ross Sea, Antarctica, Cryosphere, 10(3), 1003–1020, doi:10.5194/tc-10-1003-2016, 2016.

Hall, B. L., Hoelzel, A. R., Baroni, C., Denton, G. H., Le Boeuf, B. J., Overturf, B. and Töpf, A. L.: Holocene elephant seal distribution implies warmer-than-present climate in the Ross Sea, Proc. Natl. Acad. Sci. U. S. A., 103(27), 10213–10217, doi:10.1073/pnas.0604002103, 2006.

Hall, B. L., Denton, G. H., Stone, J. O. and Conway, H.: History of the grounded ice sheet in the Ross Sea sector of Antarctica during the Last Glacial Maximum and the last termination, Geol. Soc. London, Spec. Publ., 381(1), 167–181, doi:10.1144/SP381.5, 2013.

Haran, T., et al. MODIS Mosaic of Antarctica 2003-2004 (MOA2004) Image Map, Version 2. NASA National Snow and Ice Data Center DAAC, 2021, doi:10.5067/68TBT0CGJSOJ.

Harwood, D. M., Scherer, R. P. and Webb, P. N.: Multiple Miocene marine productivity events in West Antarctica as recorded in upper Miocene sediments beneath the Ross Ice Shelf (Site J-9), Mar. Micropaleontol., 15(1–2), 1–9, doi:10.1016/0377-8398(89)90006-6, 1989.

Helly, J. J., Kaufmann, R. S., Stephenson, G. R. and Vernet, M.: Cooling, dilution and mixing of ocean water by free-drifting icebergs in the Weddell Sea, Deep. Res. Part II Top. Stud. Oceanogr., 58(11–12), 1346–1363, doi:10.1016/j.dsr2.2010.11.010, 2011.

Higgins, A. K.: North Greenland glacier velocities and calf ice production, Polarforschung, 60(1), 1–23, 1991.

Hodson, T. O., Powell, R. D., Brachfeld, S. A., Tulaczyk, S. and Scherer, R. P.: Physical processes in Subglacial Lake Whillans, West Antarctica: Inferences from sediment cores, Earth Planet. Sci. Lett., 444(June), 56–63, doi:10.1016/j.epsl.2016.03.036, 2016.

Horgan, H. J., Alley, R. B., Christianson, K., Jacobel, R. W., Anandakrishnan, S., Muto, A., Beem, L. H. and Siegfried, M. R.: Estuaries beneath ice sheets, Geology, 41(11), 1159–1162, doi:10.1130/G34654.1, 2013a.

Horgan, H. J., Christianson, K., Jacobel, R. W., Anandakrishnan, S. and Alley, R. B.: Sediment deposition at the modern grounding zone of Whillans Ice Stream, West Antarctica, Geophys. Res. Lett., 40(15), 3934–3939, doi:10.1002/grl.50712, 2013b.

Horgan, H. J., Hulbe, C., Alley, R. B., Anandakrishnan, S., Goodsell, B., Taylor-Offord, S. and Vaughan, M. J.: Poststagnation Retreat of Kamb Ice Stream's Grounding Zone, Geophys. Res. Lett., 44(19), 9815–9822, doi:10.1002/2017GL074986, 2017.

Howat, I. M., Ahn, Y., Joughin, I., Van Den Broeke, M. R., Lenaerts, J. T. M. and Smith, B.: Mass balance of Greenland's three largest outlet glaciers, 2000-2010, Geophys. Res. Lett., 38(12), 1–5, doi:10.1029/2011GL047565, 2011.

Hughes, T.: Calving bays, Quat. Sci. Rev., 21(1–3), 267–282, doi:10.1016/S0277-3791(01)00092-0, 2002.

Hulbe, C. and Fahnestock, M.: Century-scale discharge stagnation and reactivation of the Ross ice streams, West Antarctica, J. Geophys. Res. Earth Surf., 112(F03S27), doi:10.1029/2006JF000603, 2007.

Jones, R. S., Mackintosh, A. N., Norton, K. P., Golledge, N. R., Fogwill, C. J., Kubik, P. W., Christl, M. and Greenwood, S. L.: Rapid Holocene thinning of an East Antarctic outlet glacier driven by marine ice sheet instability, Nat. Commun., 6, doi:10.1038/ncomms9910, 2015.

Joughin, I. and Tulaczyk, S.: Positive mass balance of the Ross Ice Streams, West Antarctica, Science (80-.)., 295(5554), 476–480, doi:10.1126/science.1066875, 2002.

Kamb, B.: Basal zone of the West Antarctic ice streams and its role in lubrication of their rapid motion, in Antarctic Research Series, vol. 77, pp. 157–199., 2001.

Kellogg, T. B. and Kellogg, D. E.: Pleistocene sediments beneath the Ross Ice Shelf, Nature, 293(5828), 130–133, doi:10.1038/293130a0, 1981.

Kingslake, J., Scherer, R. P., Albrecht, T., Coenen, J., Powell, R. D., Reese, R., Stansell, N. D., Tulaczyk, S., Wearing, M. G. and Whitehouse, P. L.: Extensive retreat and re-advance of the West Antarctic Ice Sheet during the Holocene, Nature, 558(7710), 430–434, doi:10.1038/s41586-018-0208-x, 2018.

Kirkham, J. D., Rosser, N. J., Wainwright, J., Vann Jones, E. C., Dunning, S. A., Lane, V. S., Hawthorn, D. E., Strzelecki, M. C. and Szczuciński, W.: Drift-dependent changes in iceberg size-frequency distributions, Sci. Rep., 7(1), 1–10, doi:10.1038/s41598-017-14863-2, 2017.

Klinck, J. M., O'Brien, J. J. and Svendsen, H.: A Simple Model of Fjord and Coastal Circulation Interaction, J. Phys. Oceanogr., 11(12), 1612–1626, doi:10.1175/1520-0485(1981)011<1612:ASMOFA>2.0.CO;2, 1981.

Kubat, I., Sayed, M., Savage, S. B., Carrieres, T. and Crocker, G. B.: An Operational Iceberg Deterioration Model, Proc. Seventeenth Int. Offshore Polar Eng. Conf., 652–657 [online] Available from: http://nparc.cisti-icist.nrc-cnrc.gc.ca/npsi/ctrl?action=rtdoc&an=12327569, 2007.

Lamb, A. L., Wilson, G. P. and Leng, M. J.: A review of coastal palaeoclimate and relative sea-level reconstructions using δ13C and C/N ratios in organic material, Earth-Science Rev., 75(1–4), 29–57, doi:10.1016/j.earscirev.2005.10.003, 2006.

Lanoil, B., Skidmore, M., Priscu, J. C., Han, S., Foo, W., Vogel, S. W., Tulaczyk, S. and Engelhardt, H.: Bacteria beneath the West Antarctic Ice Sheet, Environ. Microbiol., 11(3), 609–615, doi:10.1111/j.1462-2920.2008.01831.x, 2009.

Larsen, C. F., Motyka, R. J., Arendt, A. A., Echelmeyer, K. A. and Geissler, P. E.: Glacier changes in southeast Alaska and northwest British Columbia and contribution to sea level rise, J. Geophys. Res. Earth Surf., 112(1), 1–11, doi:10.1029/2006JF000586, 2007.

Lauro, S. E., Pettinelli, E., Caprarelli, G., Guallini, L., Rossi, A. P., Mattei, E., Cosciotti, B., Cicchetti, A., Soldovieri, F., Cartacci, M., Di Paolo, F., Noschese, R. and Orosei, R.: Multiple subglacial water bodies below the south pole of Mars unveiled by new MARSIS data, Nat. Astron., 5(1), 63–70, doi:10.1038/s41550-020-1200-6, 2021.

Lee, J. Il, McKay, R. M., Golledge, N. R., Yoon, H. Il, Yoo, K. C., Kim, H. J. and Hong, J. K.: Widespread persistence of expanded East Antarctic glaciers in the southwest Ross Sea during the last deglaciation, Geology, 45(5), 403–406, doi:10.1130/G38715.1, 2017.

Li, Y.-H. and Gregory, S.: Diffusion of ions in sea water and in deep-sea sediments. Geochim. Cosmochim. Acta, Geochim. Cosmochim. Acta, 38(5), 703–714, doi:10.1016/0016-7037(74)90145-8, 1974.

Licht, K. J., Jennings, A. E., Andrews, J. T. and Williams, K. M.: Chronology of late Wisconsin ice retreat from the western Ross Sea, Antarctica, Geology, 24(3), 223–226, doi:10.1130/0091-7613(1996)024<0223:COLWIR>2.3.CO;2, 1996.

Lowry, D. P., Golledge, N. R., Bertler, N. A. N., Jones, R. S. and McKay, R.: Deglacial grounding-line retreat in the Ross Embayment, Antarctica, controlled by ocean and atmosphere forcing, Sci. Adv., 5(8), doi:10.1126/sciadv.aav8754, 2019.

Luckman, A., Benn, D. I., Cottier, F., Bevan, S., Nilsen, F. and Inall, M.: Calving rates at tidewater glaciers vary strongly with ocean temperature, Nat. Commun., 6, 1–7, doi:10.1038/ncomms9566, 2015.

Lyons, W. B., Mikucki, J. A., German, L. A., Welch, K. A., Welch, S. A., Gardner, C. B., Tulaczyk, S. M., Pettit, E. C., Kowalski, J. and Dachwald, B.: The Geochemistry of Englacial Brine From Taylor Glacier, Antarctica, J. Geophys. Res. Biogeosciences, 124(3), 633–648, doi:10.1029/2018JG004411, 2019.

Marsh, O. J., Fricker, H. A., Siegfried, M. R. and Christianson, K.: High basal melt rates initiate a channel at the grounding line of Ross Ice Shelf, Antarctica, Geophys. Res. Lett., in press?, doi:10.1002/2015GL066612.Received, 2016.

Matsuoka, K., Hindmarsh, R. C. A., Moholdt, G., Bentley, M. J., Pritchard, H. D., Brown, J., Conway, H., Drews, R., Durand, G., Goldberg, D., Hattermann, T., Kingslake, J., Lenaerts, J. T. M., Martín, C., Mulvaney, R., Nicholls, K. W., Pattyn, F., Ross, N., Scambos, T. and Whitehouse, P. L.: Antarctic ice rises and rumples: Their properties and significance for ice-sheet dynamics and evolution, Earth-Science Rev., 150, 724–745, doi:10.1016/j.earscirev.2015.09.004, 2015.
McKay, R., Golledge, N. R., Maas, S., Naish, T., Levy, R., Dunbar, G. and Kuhn, G.: Antarctic marine ice-sheet retreat in the Ross Sea during the early Holocene, Geology, 44(1), 7–10, doi:10.1130/G37315.1, 2016.

McNabb, R. W. and Hock, R.: Variations in Alaska tidewater glacier frontal ablation, 1985-2013, J. Geophys. Res. Earth Surf., 119(2), 153–167, doi:10.1002/2014JF003276, 2014.

McNabb, R. W., Hock, R., O'Neel, S., Rasmussen, L. a., Ahn, Y., Braun, M., Conway, H., Herreid, S., Joughin, I., Pfeffer, W. T., Smith, B. E. and Truffer, M.: Using surface velocities to calculate ice thickness and bed topography: A case study at Columbia Glacier, Alaska, USA, J. Glaciol., 58(212), 1151–1164, doi:10.3189/2012JoG11J249, 2012a.

McNabb, R. W., Hock, R., O'Neel, S., Rasmussen, L. A., Ahn, Y., Braun, M., Conway, H., Herreid, S., Joughin, I., Pfeffer, W. T., Smith, B. E. and Truffer, M.: Using surface velocities to calculate ice thickness and bed topography: A case study at Columbia Glacier, Alaska, USA, J. Glaciol., 58(212), 1151–1164, doi:10.3189/2012JoG11J249, 2012b.
Meier, M. F. and Post, A.: Columbia Glacier Progress Report, , (DECEMBER 1977), 1978.

Michaud, A. B., Skidmore, M. L., Mitchell, A. C., Vick-Majors, T. J., Barbante, C., Turetta, C., Van Gelder, W. and Priscu, J. C.: Solute sources and geochemical processes in Subglacial Lake Whillans, West Antarctica, Geology, 44(5), 347–350, doi:10.1130/G37639.1, 2016a.

Michaud, A. B., Skidmore, M. L., Mitchell, A. C., Vick-Majors, T. J., Barbante, C., Turetta, C., VanGelder, W. and Priscu, J. C.: Supplemental material: Solute sources and geochemical processes in Subglacial Lake Whillans, West Antarctica, Geol. Soc. Am., doi:10.1130/2016110, 2016b.

Mikucki, J. A., Pearson, A., Johnston, D. T., Turchyn, A. V, Farquhar, J., Schrag, D. P., Anbar, A. D., Priscu, J. C. and Lee, P. A.: A Contemporary Microbially Maintained Subglacial Ferrous "Ocean," Science (80-.)., 324, 397–400, 2009.

Montross, S., Skidmore, M., Christner, B., Samyn, D., Tison, J. L., Lorrain, R., Doyle, S. and Fitzsimons, S.: Debris-Rich Basal Ice as a Microbial Habitat, Taylor Glacier, Antarctica, Geomicrobiol. J., 31(1), 76–81, doi:10.1080/01490451.2013.811316, 2014.

Moon, T., Sutherland, D. A., Carroll, D., Felikson, D., Kehrl, L. and Straneo, F.: Subsurface iceberg melt key to Greenland fjord freshwater budget, Nat. Geosci., 11(1), 49–54, doi:10.1038/s41561-017-0018-z, 2018a.
Moon, T., Sutherland, D. A., Carroll, D., Felikson, D., Kehrl, L. and Straneo, F.: Subsurface iceberg melt key to Greenland fjord freshwater budget, Nat. Geosci., 11(1), 49–54, doi:10.1038/s41561-017-0018-z, 2018b.

Morin, R. H., Williams, T., Henrys, S. A., Magens, D., Niessen, F. and Hansaraj, D.: Heat flow and hydrologic characteristics at the AND-1B borehole, ANDRILL McMurdo Ice Shelf project, Antarctica, Geosphere, 6(4), 370–378, doi:10.1130/GES00512.1, 2010.

Mortensen, J., Rysgaard, S., Arendt, K. E., Juul-Pedersen, T., Søgaard, D. H., Bendtsen, J. and Meire, L.: Local coastal water masses control heat levels in a West Greenland tidewater outlet glacier fjord, J. Geophys. Res. Ocean., (123), 1–16, doi:10.1029/2018JC014549, 2018.

Motyka, R. J., Hunter, L., Echelmeyer, K. a. and Connor, C.: Submarine melting at the terminus of a temperate tidewater glacier, LeConte Glacier, Alaska, U.S.A, Ann. Glaciol., 36, 57–65, doi:10.3189/172756403781816374, 2003.

Müller, P. J.: C N ratios in Pacific deep-sea sediments: Effect of inorganic ammonium and organic nitrogen compounds sorbed by clays, Geochim. Cosmochim. Acta, 41(6), 765–776, doi:10.1016/0016-7037(77)90047-3, 1977.

Null, K. A., Corbett, D. R., Crenshaw, J., Peterson, R. N., Peterson, L. E. and Lyons, W. B.: Groundwater discharge to the western antarctic coastal ocean, Polar Res., 38, 1–11, doi:10.33265/polar.v38.3497, 2019.

O'Leary, M. and Christoffersen, P.: Calving on tidewater glaciers amplified by submarine frontal melting, Cryosphere, 7(1), 119–128, doi:10.5194/tc-7-119-2013, 2013.

O'Neel, S., Echelmeyer, K. A. and Motyka, R. J.: Short-term variations in calving of a tidewater glacier: LeConte Glacier, Alaska, U.S.A, J. Glaciol., 49(167), 587–598, doi:10.3189/172756503781830430, 2003.

Orosei, R., Lauro, S. E., Pettinelli, E., Cicchetti, A., Coradini, M., Cosciotti, B., Di Paolo, F., Flamini, E., Mattei, E., Pajola, M., Soldovieri, F., Cartacci, M., Cassenti, F., Frigeri, A., Giuppi, S., Martufi, R., Masdea, A., Mitri, G., Nenna, C., Noschese, R., Restano, M. and Seu, R.: Radar evidence of subglacial liquid water on Mars, Science (80-.)., 361(6401), 490–493, doi:10.1126/science.aar7268, 2018.

Paulsen, T., Millan, C., Pierdominici, S., Wilson, T., Drew, S. and ANDRILL SMS Science Team: Fracture Logging of the AND-2A Core, ANDRILL Southern McMurdo Sound Project, Antarctica, Terra Antart., 15(1), 69–76, 2008.

Payne, R. E.: Albedo of the Sea Surface, J. Atmos. Sci., 29(5), 959–970, doi:10.1175/1520-0469(1972)029<0959:AOTSS>2.0.CO;2, 1972.

Pfeffer, W. T.: Report to Prince William Sound Citizen's Regional Advisory Council: Future Iceberg Discharge from Columbia Glacier, Alaska - Report 1, , (December), 1–46, 2012.

Pfeffer, W. T.: Report to Prince William Sound Citizen's Regional Advisory Council: Future Iceberg Discharge from Columbia Glacier, Alaska - Report 2, , (June), 1–20, 2013a.

Pfeffer, W. T.: Report to Prince William Sound Citizen's Regional Advisory Council: Future Iceberg Discharge from Columbia Glacier, Alaska - Report 3, , (November), 1–22, 2013b.

Pfeffer, W. T.: Report to Prince William Sound Citizen's Regional Advisory Council: Future Iceberg Discharge from Columbia Glacier, Alaska - Report 4, , (October), 1–10, 2014a.

Pfeffer, W. T.: Report to Prince William Sound Citizen's Regional Advisory Council: Future Iceberg Discharge from Columbia Glacier, Alaska - Report 5, , (October), 1–8, 2014b.

Pfeffer, W. T.: Report to Prince William Sound Citizen's Regional Advisory Council: Future Iceberg Discharge from Columbia Glacier, Alaska - Final Report, , (June), 1–20, 2015.

Pompilio, M., Dunbar, N., Gebhardt, A. C., Helling, D., Kuhn, G., Kyle, P., McKay, R., Talarico, F., Tulaczyk, S., Vogel, S., Wilch, T. and Team, A.-M. S.: Petrology and geochemistry of the AND-1B core, ANDRILL McMurdo Ice Shelf Project, Antartica, Terra Antart., 14(3), 255–288, 2007.

Post, A.: Preliminary hydrography and historic terminal changes of Columbia Glacier, Alaska. [online] Available from: http://pubs.er.usgs.gov/publication/ha559, 1975.

Pritchard, H. D., Arthern, R. J., Vaughan, D. G. and Edwards, L. A.: Extensive dynamic thinning on the margins of the Greenland and Antarctic ice sheets, Nature, 461(7266), 971–975, doi:10.1038/nature08471, 2009.

Prothro, L. O., Majewski, W., Yokoyama, Y., Simkins, L. M., Anderson, J. B., Yamane, M., Miyairi, Y. and Ohkouchi, N.: Timing and pathways of East Antarctic Ice Sheet retreat, Quat. Sci. Rev., 230(106166), doi:10.1016/j.quascirev.2020.106166, 2020.

Purcell, A. M., Mikucki, J. A., Achberger, A. M., Alekhina, I. A., Barbante, C., Christner, B. C., Ghosh, D., Michaud, A. B., Mitchell, A. C., Priscu, J. C., Scherer, R., Skidmore, M. L., Vick-Majors, T. J., Adkins, W. P., Anandakrishnan, S., Barcheck, G., Beem, L., Behar, A., Beitch, M., Bolsey, R., Branecky, C., Carter, S., Christianson, K., Edwards, R., Fisher, A., Fricker, H., Foley, N., Guthrie, B., Hodson, T., Jacobel, R., Kelley, S., Mankoff, K., McBryan, E., Powell, R., Sampson, D., Severinghaus, J., Sherve, J., Siegfried, M. and Tulaczyk, S.: Microbial sulfur transformations in sediments from Subglacial Lake Whillans, Front. Microbiol., 5(NOV), 1–16, doi:10.3389/fmicb.2014.00594, 2014.

Rasmussen, L. a., Conway, H., Krimmel, R. M. and Hock, R.: Surface mass balance, thinning and iceberg production, Columbia Glacier, Alaska, 1948-2007, J. Glaciol., 57(203), 431–440, doi:10.3189/002214311796905532, 2011.

Redfield, A. C.: The biological control of chemical factors in the environment, Am. Sci., 46(3), 230A, 205–221, 1958.

Retzlaff, R. and Bentley, C. R.: Timing of stagnation of ice stream C, West Antarctica, from short- pulse radar studies of buried surface crevasses, J. Glaciol., 39(133), 553–561, doi:10.1017/S0022143000016440, 1993.

Rignot, E., Koppes, M. and Velicogna, I.: Rapid submarine melting of the calving faces of West Greenland glaciers, Nat. Geosci., 3(3), 187–191, doi:10.1038/ngeo765, 2010.

Rignot, E., Mouginot, J. and Scheuchl, B.: Antarctic grounding line mapping from differential satellite radar interferometry, Geophys. Res. Lett., 38(10), 1–6, doi:10.1029/2011GL047109, 2011.

Rignot, E., J. Mouginot, and B. Scheuchl. 2017. *MEaSUREs InSAR-Based Antarctica Ice Velocity Map, Version 2*. [antarctica_ice_velocity_450m_v2]. Boulder, Colorado USA. NASA National Snow and Ice Data Center Distributed Active Archive Center. doi: 10.5067/D7GK8F5J8M8R. [Accessed May 17, 2021].

Scherer, R. P., Aldahan, A., Tulaczyk, S., Possnert, G., Engelhardt, H. and Kamb, B.: Pleistocene collapse of the West Antarctic ice sheet, Science (80-.)., 281(5373), 82–85, doi:10.1126/science.281.5373.82, 1998.

Simkins, L. M., Greenwood, S. L. and Anderson, J. B.: Diagnosing ice sheet grounding line stability from landform morphology, Cryosphere, 12(8), 2707–2726, doi:10.5194/tc-12-2707-2018, 2018.

Small, C. and Nicholls, R. J.: A global analysis of human settlement in coastal zones, J. Coast. Res., 19(3), 584–599, 2003.

Smith, J. A., Graham, A. G. C., Post, A. L., Hillenbrand, C. D., Bart, P. J. and Powell, R. D.: The marine geological imprint of Antarctic ice shelves, Nat. Commun., 10(1), doi:10.1038/s41467-019-13496-5, 2019.

Spahn, F., Vieira Neto, E., Guimarães, A. H. F., Gorban, A. N. and Brilliantov, N. V.: A statistical model of aggregate fragmentation, New J. Phys., 16, doi:10.1088/1367-2630/16/1/013031, 2014.

Spector, P., Stone, J., Cowdery, S. G., Hall, B., Conway, H. and Bromley, G.: Rapid early-Holocene deglaciation in the Ross Sea, Antarctica, Geophys. Res. Lett., 44(15), 7817–7825, doi:10.1002/2017GL074216, 2017.

Starinsky, A. and Katz, A.: The formation of natural cryogenic brines, Geochim. Cosmochim. Acta, 67(8), 1475–1484, doi:10.1016/S0016-7037(02)01295-4, 2003.

Staudigel, P. T., Murray, S., Dunham, D. P., Frank, T. D., Fielding, C. R. and Swart, P. K.: Cryogenic brines as diagenetic fluids: Reconstructing the diagenetic history of the Victoria Land Basin using clumped isotopes, Geochim. Cosmochim. Acta, 224, 154–170, doi:10.1016/j.gca.2018.01.002, 2018.

Still, H., Campbell, A. and Hulbe, C.: Mechanical analysis of pinning points in the Ross Ice Shelf, Antarctica, Ann. Glaciol., 60(78), 32–41, doi:10.1017/aog.2018.31, 2019.

Stuiver, M. and Polach, H. A.: Discussion Reporting of 14 C Data, Radiocarbon, 19(3), 355–363, doi:10.1017/S0033822200003672, 1977.

Sulak, D. J., Sutherland, D. A., Enderlin, E. M., Stearns, L. A. and Hamilton, G. S.: Iceberg properties and distributions in three Greenlandic fjords using satellite imagery, Ann. Glaciol., 58(74), 92–106, doi:10.1017/aog.2017.5, 2017.

Sutherland, D. A., Roth, G. E., Hamilton, G. S., Mernild, S. H., Stearns, L. A. and Straneo, F.: Quantifying flow regimes in a Greenland glacial fjord using iceberg drifters, Geophys. Res. Lett., 41, 8411–8420, doi:10.1002/2014GL062256, 2014.

Tinto, K. J., Padman, L., Siddoway, C. S., Springer, S. R., Fricker, H. A., Das, I., Caratori Tontini, F., Porter, D. F., Frearson, N. P., Howard, S. L., Siegfried, M. R., Mosbeux, C., Becker, M. K., Bertinato, C., Boghosian, A., Brady, N., Burton, B. L., Chu, W., Cordero, S. I., Dhakal, T., Dong, L., Gustafson, C. D., Keeshin, S., Locke, C., Lockett, A., O'Brien, G., Spergel, J. J., Starke, S. E., Tankersley, M., Wearing, M. G. and Bell, R. E.: Ross Ice Shelf response to climate driven by the tectonic imprint on seafloor bathymetry, Nat. Geosci., 12(6), 441–449, doi:10.1038/s41561-019-0370-2, 2019.

Tournadre, J., Bouhier, N., Girard-Ardhuin, F. and Rémy, F.: Antarctic iceberg distributions 1992-2014, J. Geophys. Res. Ocean., 121, 327–349, doi:10.1002/2015JC011178, 2016.

Toyota, T., Smith, I. J., Gough, A. J., Langhorne, P. J., Leonard, G. H., Van Hale, R. J., Mahoney, A. R. and Haskell, T. G.: Oxygen isotope fractionation during the freezing of sea water, J. Glaciol., 59(216), 697–710, doi:10.3189/2013JoG12J163, 2013.

Tranter, M.: Microbes eat rock under ice, Nature, 512(7514), 256–257, doi:10.1038/512256a, 2014.

Tulaczyk, S., Kamb, B. and Engelhardt, H. F.: Estimates of effective stress beneath a modern West Antarctic ice stream from till preconsolidation and void ratio, Boreas, 30(2), 101–114, doi:10.1111/j.1502-3885.2001.tb01216.x, 2001.
Tulaczyk, S., Mikucki, J. A., Siegfried, M. R., Priscu, J. C., Barcheck, C. G., Beem, L. H., Behar, A., Burnett, J., Christner, B. C., Fisher, A. T., Fricker, H. A., Mankoff, K. D., Powell, R. D., Rack, F., Sampson, D., Scherer, R. P. and Schwartz, S. Y.: WISSARD at Subglacial Lake Whillans, West Antarctica: scientific operations and initial observations, Ann. Glaciol., 55(65), 51–58, doi:10.3189/2014aog65a009, 2014.
Turcotte, D. and Schubert, G.: Geodynamics, 3rd ed., Cambridge University Press, Cambridge., 2014.

Turner, J. T.: Zooplankton fecal pellets, marine snow, phytodetritus and the ocean's biological pump, Prog. Oceanogr., 130, 205–248, doi:10.1016/j.pocean.2014.08.005, 2015.

Vasskog, K., Langebroek, P. M., Andrews, J. T., Nilsen, J. E. Ø. and Nesje, A.: The Greenland Ice Sheet during the last glacial cycle: Current ice loss and contribution to sea-level rise from a palaeoclimatic perspective, Earth-Science Rev., 150, 45–67, doi:10.1016/j.earscirev.2015.07.006, 2015.

Van Der Veen, C. J.: Fracture mechanics approach to penetration of surface crevasses on glaciers, Cold Reg. Sci. Technol., 27(1), 31–47, doi:10.1016/S0165-232X(97)00022-0, 1998.

Venturelli, R. A., Siegfried, M. R., Roush, K. A., Li, W., Burnett, J., Zook, R., Fricker, H. A., Priscu, J. C., Leventer, A. and Rosenheim, B. E.: Mid-Holocene Grounding Line Retreat and Readvance at Whillans Ice Stream, West Antarctica, Geophys. Res. Lett., 47(15), doi:10.1029/2020GL088476, 2020.

Vick-Majors, T. J., Michaud, A. B., Skidmore, M. L., Turetta, C., Barbante, C., Christner, B. C., Dore, J. E., Christianson, K., Mitchell, A. C., Achberger, A. M., Mikucki, J. A. and Priscu, J. C.: Biogeochemical Connectivity Between Freshwater Ecosystems beneath the West Antarctic Ice Sheet and the Sub-Ice Marine Environment, Global Biogeochem. Cycles, 34(3), no, doi:10.1029/2019GB006446, 2020.

Vijay, S. and Braun, M.: Seasonal and interannual variability of Columbia Glacier, Alaska (2011-2016): Ice Velocity, Mass Flux, surface elevation and front position, Remote Sens., 9(6), 1–18, doi:10.3390/rs9060635, 2017.

Vogel, S.W.: The basal regime of the West-Antarctic ice sheet interaction of subglacial geology with ice dynamics, Ph.D. dissertation, University of California, Santa Cruz, 137 pp., 2004.

Vogel, S. W., Tulaczyk, S., Kamb, B., Engelhardt, H., Carsey, F. D., Behar, A. E., Lane, A. L. and Joughin, I.: Subglacial conditions during and after stoppage of an Antarctic Ice Stream: Is reactivation imminent?, Geophys. Res. Lett., 32(14), 1–4, doi:10.1029/2005GL022563, 2005.

Waddington, E. D., Conway, H., Steig, E. J., Alley, R. B., Brook, E. J., Taylor, K. C. and White, J. W. C.: Decoding the dipstick: Thickness of Siple Dome, West Antarctica, at the Last Glacial Maximum, Geology, 33(4), 281–284, doi:10.1130/G21165.1, 2005.

Wadham, J. L., Tranter, M., Skidmore, M., Hodson, A. J., Priscu, J., Lyons, W. B., Sharp, M., Wynn, P. and Jackson, M.: Biogeochemical weathering under ice: Size matters, Global Biogeochem. Cycles, 24(3), doi:10.1029/2009GB003688, 2010.

Wadham, J. L., De'Ath, R., Monteiro, F. M., Tranter, M., Ridgwell, A., Raiswell, R. and Tulaczyk, S.: The potential role of the Antarctic Ice Sheet in global biogeochemical cycles, Earth Environ. Sci. Trans. R. Soc. Edinburgh, 104(1), 55–67, doi:10.1017/S1755691013000108, 2013.

Walter, J. I., Box, J. E., Tulaczyk, S., Brodsky, E. E., Howat, I. M., Ahn, Y. and Brown, A.: Oceanic mechanical forcing of a marine-terminating greenland glacier, Ann. Glaciol., 53(60), 181–192, doi:10.3189/2012AoG60A083, 2012.

Walters, R. A., Josberger, E. G. and Driedger, C. L.: Columbia Bay, Alaska: an "upside down" estuary, Estuar. Coast. Shelf Sci., 26(6), 607–617 [online] Available from: http://pubs.er.usgs.gov/publication/70013755, 1988.

Wang, J. H.: Self-Diffusion and Structure of Liquid Water. I. Measurement of Self-Diffusion of Liquid Water with Deuterium as Tracer, J. Am. Chem. Soc., 73(2), 510–513, doi:10.1021/ja01146a002, 1951a.

Wang, J. H.: Self-diffusion and Structure of Liquid Water. II. Measurement of Self-diffusion of Liquid Water with O18 as Tracer, , 73(9), 4181–4183, doi:10.1021/ja01153a039, 1951b.

Wang, Y., Hou, S., Masson-Delmotte, V. and Jouzel, J.: A generalized additive model for the spatial distribution of stable isotopic composition in Antarctic surface snow, Chem. Geol., 271(3–4), 133–141, doi:10.1016/j.chemgeo.2010.01.004, 2010.

Warren, C., Benn, D., Winchester, V. and Harrison, S.: Buoyancy-driven lacustrine calving, Glaciar Nef, Chilean Patagonia, J. Glaciol., 47(156), 135–146, doi:10.3189/172756501781832403, 2001.

Weertman, J.: Can a water-filled crevasse reach the bottom surface of a glacier?, Symp. Cambridge 1969 - Hydrol. Glaciers, 95, 139–145, doi:10.1017/CBO9781107415324.004, 1973.

Weertman, J.: Stability of the junction of an ice sheet and an ice shelf, J. Glaciol., 13(67), 3–11, 1974.

Wooding, R. A.: Variable-density saturated flow with modified Darcy's law: The salt lake problem and circulation, Water Resour. Res., 43(2), 1–10, doi:10.1029/2005WR004377, 2007.

Zeng, Q., Meisheng, C., Xuezhi, F., Fengxian, L., Xianzhang, C. and Wenkun, S.: Study on spectral reflection characteristics of snow, ice and water of northwest China., Sci. Sin. Ser. B, 27(145), 647–656, 1984.